Fall 12-2020

Space-Based Countermeasure for Hypersonic Glide Vehicle

Robert Joseph Fowler IV
Old Dominion University, rfowl006@odu.edu

SPACE-BASED LASER COUNTERMEASURE FOR HYPERSONIC GLIDE VEHICLE

by

Robert Joseph Fowler IV
B.S. December 2004, Michigan Technological University

A Thesis Submitted to the Faculty of
Old Dominion University in Partial Fulfillment of the
Requirements for the Degree of

MASTER OF SCIENCE

AEROSPACE ENGINEERING

OLD DOMINION UNIVERSITY
December 2020

Approved by:

Brett A. Newman (Director)

Robert L. Ash (Member)

Christopher J. Weiland (Member)

ABSTRACT

SPACE-BASED LASER COUNTERMEASURE FOR HYPERSONIC GLIDE VEHICLE

Robert Joseph Fowler IV
Old Dominion University, 2020
Director: Dr. Brett Newman

The purpose of this thesis is to investigate the effectiveness of a space-based laser weapon system for countering a hypersonic glide vehicle. Hypersonic glide vehicles are an emerging type of weapon system which combine the range of ballistic missiles with the maneuverability of cruise missiles. These systems pose a unique threat to military assets not only for their expanded capabilities but also for the lack of an effective defensive countermeasure. Space-based laser weapon systems may offer a solution to this problem. The dynamics of a space-based laser system defending against a hypersonic glide vehicle are modeled first. The governing equations of motion for the space orbital mechanics and the atmospheric flight mechanics of the two objects, assuming point mass three degree of freedom conditions, are defined. Several variables in the engagement model are allowed to vary including initial conditions for true anomaly and right ascension of the ascending node for the space-based laser system and the velocity ratio, angle of attack, and heading about the ground target for the hypersonic glide vehicle. The motion of each object is propagated from the initial condition forward in time from which the relative motion and lasing along the line of sight are analyzed. A predetermined intercept range for the laser is then compared against the flight path of the hypersonic glide vehicle to determine when a successful intercept of the hypersonic glide vehicle occurs. Finally, the solution set for the intercept of the hypersonic glide vehicle by the

laser is examined. Results reveal usable solution sets do exist where a space-based laser system could defensively counter a hypersonic glide vehicle attacking a specific ground target.

ACKNOWLEDGMENTS

I would like to thank my wife, Melody, and my two children, Joey and Katie, for their infinite love and patience. My appreciation also goes to my parents and parents-in-law for their support and encouragement. My gratitude for making this thesis a reality goes to Dr. Newman as well as for the knowledge I have gained from him. I would also like to thank Drs. Ash and Weiland for serving on my thesis committee as well as for the knowledge they have imparted to me. To the Lord, for second chances.

NOMENCLATURE

a	Semi-major Axis
A_{Rot}	Rotation Matrix
B	Constant in density altitude relation
e	Eccentricity
E	Eccentric Anomaly
g	Earth's gravity
h	HGV initial launch altitude
H	Isothermal scale height of the atmosphere
H	Specific angular momentum
Î	vernal equinox
i	Inclination
J	HGV range parameter
L/D	Lift to Drag Ratio
Lat_{target}	Target's Latitude
$Long_{target}$	Target's Longitude
mm	Number of moles
n	Mean Motion
P	Semi-latus Rectum
r_e	Earth's Radius
R	Ideal gas constant

$\vec{R}$	Geocentric equatorial position vector
s	HGV distance along flight path
T	Air temperature
u	Argument of latitude
t_0	time
$\vec{V}$	Geocentric equatorial velocity vector
V_L	HGV initial launch velocity
$V_{r=r0}$	HGV velocity at ground level
μ	Earth gravitational constant
$\Phi_{ballistic}$	HGV Range ballistic/skip phase
Φ_{glide}	HGV Range glide phase
φ	HGV Heading Angle
v	True Anomaly
Ω	Right Ascension of Ascending Node
ω	Argument of Perigee

TABLE OF CONTENTS

Page

LIST OF TABLES x

LIST OF FIGURES xi

Chapter

1. INTRODUCTION 1
   - 1.1. Problem Motivation 1
   - 1.2. Literature Review 3
     - 1.2.1 Hypersonic Weapons 3
     - 1.2.2 Laser Weapon Systems 18
   - 1.3. Space Based Laser 26
   - 1.4. Problem Statement 30
   - 1.5. Assumptions 30
     - 1.5.1 Overall 30
     - 1.5.2 LWS 31
     - 1.5.3 HGV 31
   - 1.6. Thesis Outline 32

2. DESIGN METHODOLOGY AND MODEL DEVELOPMENT 33
   - 2.1. Approach 33
   - 2.2. Objectives 33
   - 2.3. Initial Conditions 36
   - 2.4. Orbital Mechanics 38
   - 2.5. Closed Form Solution for LWS Orbit 41
   - 2.6. Numerical Solution for LWS Orbit 46
   - 2.7. HGV Boost Phase Equations of Motion 47
   - 2.8. HGV Glide Phase Equations of Motion 49

3. SIMULATION OVERVIEW 51
   - 3.1. Program Layout 51
   - 3.2. HGV Flight Path Determination 56
   - 3.3. Ground Track Propagation 59

4. CASE STUDY RESULTS 61
   - 4.1. Analysis Results 61
   - 4.2. Individual Case Study 66
   - 4.3. Quality Metrics 71

5. CONCLUSIONS 77

5.1. Conclusions 77
5.2. Recommendations 77

REFERENCES 79

VITA 84

LIST OF TABLES

Table Page

1 Upper and Lower Bounds for Quality Metrics 35

2 Control Inputs for LWS and HGV 51

3 Program Constants 52

4 Constants for LWS.m 52

5 Constants for LWS_TIME.m 53

6 Constants for HGV.m 53

7 Intercept Data for Single LWS Orbit 70

8 Quality Metrics for Single LWS Orbit 70

LIST OF FIGURES

Figure Page

1 X-15 Three-View with Design Characteristics 4

2 X-15 Altitude vs. Range Plot 5

3 X-15 Lateral vs. Longitudal Range Plot During Gliding Flight 5

4 Minuteman II Exploded View 6

5 Trident Exploded View 7

6 Typical ICBM Flight Sequence 7

7 MIRV Capability 8

8 AGM-86B and AGM-109 9

9 Typical Cruise Missile Strategic Mission Profile 9

10 X-43 Scramjet Vehicle Geometry 10

11 X-43A Mounted to Pegasus Rocket on B-52 Stratofortress 11

12 X-43A Flight Profile 11

13 X-51A Waverider Scramjet 12

14 X-51 Attached to ATACMS on B-52 Stratofortress 13

15 X-51 Flight Profile 13

16 MARV vs. HGV Approximated Range 14

17 Range Map from Norfolk Naval Station 15

18 Ballistic Missile vs. HGV Flight Path 16

19 HGV Ballistic Phase 17

20 HGV Reentry and Pull-Up Phases 17

Figure Page

21 HGV Glide Phase 18

22 NKC-135A Airborne Laser Lab 20

23 Beriev A-60 Airborne Laser 20

24 Boeing YAL-1 Airborne Laser 21

25 Boeing YAL-1 Engagement Scenario 22

26 Tactical High Energy Laser 23

27 Tactical High Energy Laser Engagement Scenario 23

28 US Navy LWS Incremental Approach 25

29 Proposed BMD Space-Based Laser 28

30 SBL IFX Typical Engagement Profile 28

31 SBL Constellation Coverage 29

32 Ballistic Missile Defense Efforts 29

33 Vector Diagram for LWS and HGV 35

34 Quality Metrics Q_R, Q_T, and Q_G 36

35 Semi-Major Axis 40

36 Eccentricity 40

37 Classical Angular Orbital Elements 40

38 Orbital State Vectors 41

39 Ballistic Phase Launch Geometry 48

40 Flat Earth Map with HGV-LWS Data 54

41 Program Flow Chart Layout 55

42 HGV Heading to Ground Target 56

Figure Page

43 Ground Track Representation 60

44 Successful Intercepts 62

45 Intercepts with respect to HGV Heading and Velocity Ratio 62

46 Intercepts for Vf = 0.1 64

47 Intercepts for Vf = 0.2 64

48 Intercepts for Vf = 0.3 65

49 Intercepts for Vf = 0.4 65

50 Intercepts for Vf = 0.5 66

51 Intercept for Vf = 0.1 and Ω between 205° and 290° with LWS Ground Tracks 67

52 Intercepts for Vf = 0.1 and Ω between 100° and 185° with LWS Ground Tracks..... 67

53 Intercepts for Vf = 0.1 and HGV Heading North, with LWS Ground Tracks..... 69

54 Intercepts for Single LWS Orbit 69

55 Quality Metrics for Single LWS Orbit vs. Time Step 70

56 Intercept Occurrence vs. Range Quality 72

57 Intercept Occurrence vs. Time Quality 72

58 Intercept Occurrence vs. Geometry Quality 73

59 Intercept Occurrence vs. Total Quality 73

60 Right Ascension of Ascending Node vs. Total Quality for Multiple Headings at Vf =0.1..... 74

61 Right Ascension of Ascending Node vs. Total Quality for Multiple Headings at Vf =0.2..... 75

62 Right Ascension of Ascending Node vs. Total Quality for Multiple Headings at Vf =0.3..... 75

63 Right Ascension of Ascending Node vs. Total Quality for Multiple Headings at Vf =0.4..... 76

64 Right Ascension of Ascending Node vs. Total Quality for Multiple Headings at Vf =0.5 76

CHAPTER 1

INTRODUCTION

1.1. Problem Motivation

During the course of human history man has sought to protect himself from his environment and his fellow man. This drive within our species for protection has spurred the often interlinked advancement of technology and defensive weaponry. The 20th century saw the advancement of powered atmospheric flight followed later by space flight. However, as early as the 1930s the idea of using a rocket to launch a reentry vehicle capable of gliding along the upper atmosphere at hypersonic speed was proposed by aeronautical engineer Eugen Sänger. [1] During the late 1950s and early 1960s, in the midst of the Cold War, the United States investigated hypersonic vehicles, developing plans for a sophisticated manned spaceplane named the X-20 Dynamic Soarer or Dyna-Soar. [2] Although the project was cancelled shortly after construction, portions of the design would be realized later in the form of NASA's Space Shuttle. The Space Shuttle, however, lacked the skip-glide capability of Dyna-Soar, and it would be another 20 years before significant investment would be made resulting in the return of hypersonic skip-glide vehicles.

In 1917 the emission process for a coherent radiation beam was described by Albert Einstein. [3] Almost forty years later, in 1960, the engineer and physicist Theodore Maiman would build the world's first light amplification by stimulated emission of radiation or LASER. [4] Today laser technology can be found in many useful applications including communications, home electronics, medical equipment, manufacturing, and national defense. With the growing threat posed by ballistic missiles during the 1970s and early 1980s, United States President

Reagan was determined to develop a nuclear deterrent that did not result in mutually assured destruction. He called upon

> *"... the scientific community in our country, those who gave us nuclear weapons, to turn their great talents now to the cause of mankind and world peace, to give us the means of rendering these nuclear weapons impotent and obsolete."* [5]

This initiative led to the creation of the Strategic Defense Initiative (SDI), headed by the SDI Organization (SDIO) which investigated the feasibility of several missile defense technologies, including lasers, particle beams, and space-based missiles. Although many aspects of the original SDI were determined to be years away from feasibility, work of the SDIO would continue when it would eventually become the Missile Defense Agency (MDA). MDA investigated several means of missile defense including a joint project with Boeing, Northrup Grumman, and Lockheed Martin to develop the YAL-1 Airborne Laser (ABL) outfitted with a chemical oxygen iodine laser (COIL). The YAL-1 successfully destroyed a boosting ballistic test missile in 2010, resulting in the first directed energy lethal intercept demonstration from an airborne platform. [6]

During the last 10 years, utilizing advancements in materials science, militaries around the globe have begun to test hypersonic missiles with skip-glide capability. Recently, Russia fielded the Vanguard Hypersonic Glide Vehicle (HGV), the world's first such weapon system traveling at Mach 20. [7] As with cannons and rockets before them, hypersonic missiles have the potential to unseat decades long military strategies focused on ballistic missile defense (BMD). The entrance of HGVs onto the battlefield presents a new challenge for national security. Anti-missile ballistic weapons do not possess the speed or maneuverability to counter these new

weapons. Countermeasures such as Close-In Weapon Support (CIWS) are also ineffective given the velocity of the HGVs. As such, the U.S. military's land and sea assets are unprotected. Investigations to combat and counter hypersonic missiles are of significant importance to protect our military assets. Laser weapon systems offer a potential solution to combating the threats faced by hypersonic missiles. First conceived during the Reagan era for deterrence of ballistic missiles, one of these concepts is the Space-Based Laser (SBL). Over the last several years laser weapon technology has matured to the point where the U.S. Navy is fielding multiple Laser Weapon Systems (LWS) across the fleet as part of the Navy Laser Weapon Incremental Approach. [8] The U.S. Department of Defense is similarly investigating aircraft based LWSs such as the Airborne High Energy Laser (AHEL) for use on an AC–130 as well as an LWS integrated with a fighter jet. [9] The importance of these countermeasures for new high-speed threats motivates this thesis investigation.

1.2. Literature Review

1.2.1 Hypersonic Weapons

Most hypersonic vehicle technologies that exist in the United States can be traced back to the NASA X-15 hypersonic research aircraft, which was designed and manufactured by North American Aviation. Three research vehicles were flown on 200 missions from 1959 to 1968 with the primary purpose to serve as the intermediary step to piloted space flight. The X-15 explored advancements in hypersonic flows, high-temperature metallic alloys, liquid rocket propulsion, and guidance control systems. Vehicle configuration as seen in Figure 1 consisted of a highly slender but conventional layout with main wing and aft horizontal and vertical tails with a single internal rocket. Design specifications, as described in References [10] and [11], included maximum velocity of 6,600 ft/s, maximum altitude of 250,000 ft, maximum dynamic

pressure of 2,500 lbf/in^2, maximum temperature of 1,200 F, and maximum load factor of 7.33 g. After being air dropped by the host B-52 aircraft, which served as the first stage, a typical mission profile, as shown in Figure 2 and Figure 3, consisted of boosted ascent, ballistic arc through near space conditions, gliding reentry, and finally approach and landing. The vehicle would commonly experience hypersonic conditions up to Mach 6 and would maneuver both longitudinally and laterally. The X-15 demonstrated many of the essential capabilities of a modern HGV, and its characteristics are highly relevant to the class of HGVs investigated in the thesis.

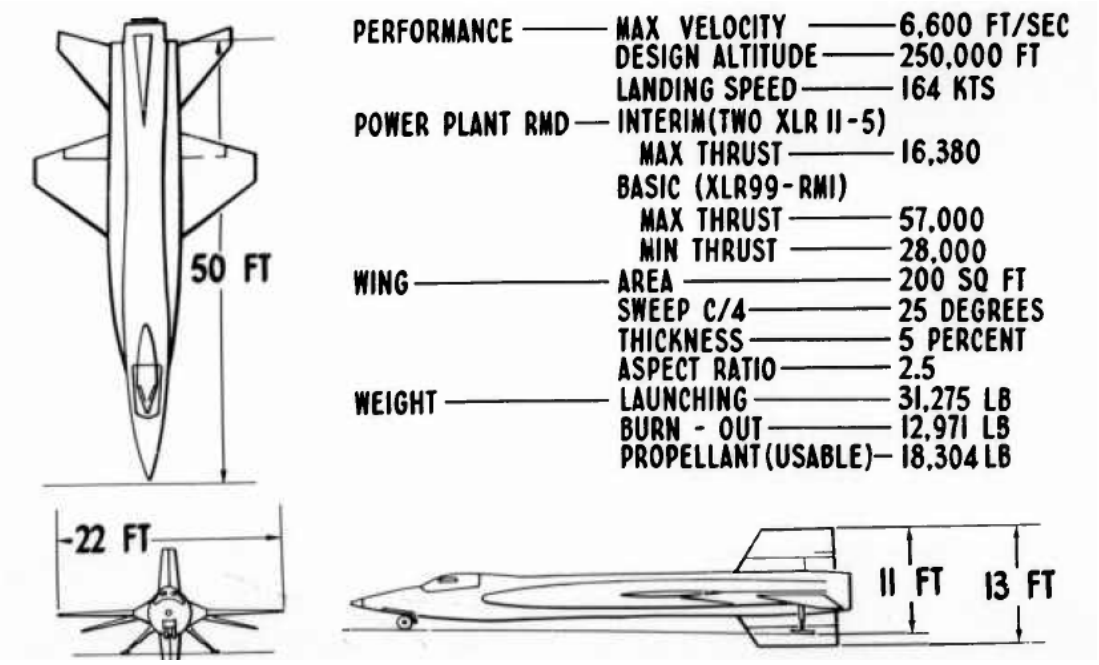

Figure 1 X-15 Three-View with Design Characteristics [10]

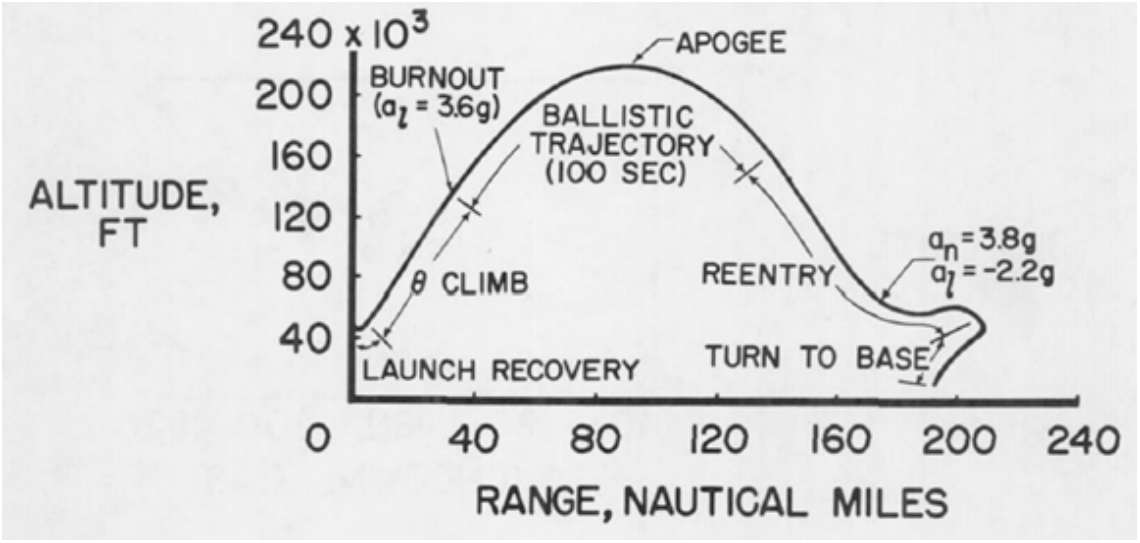

Figure 2 X-15 Altitude vs. Range Plot [11]

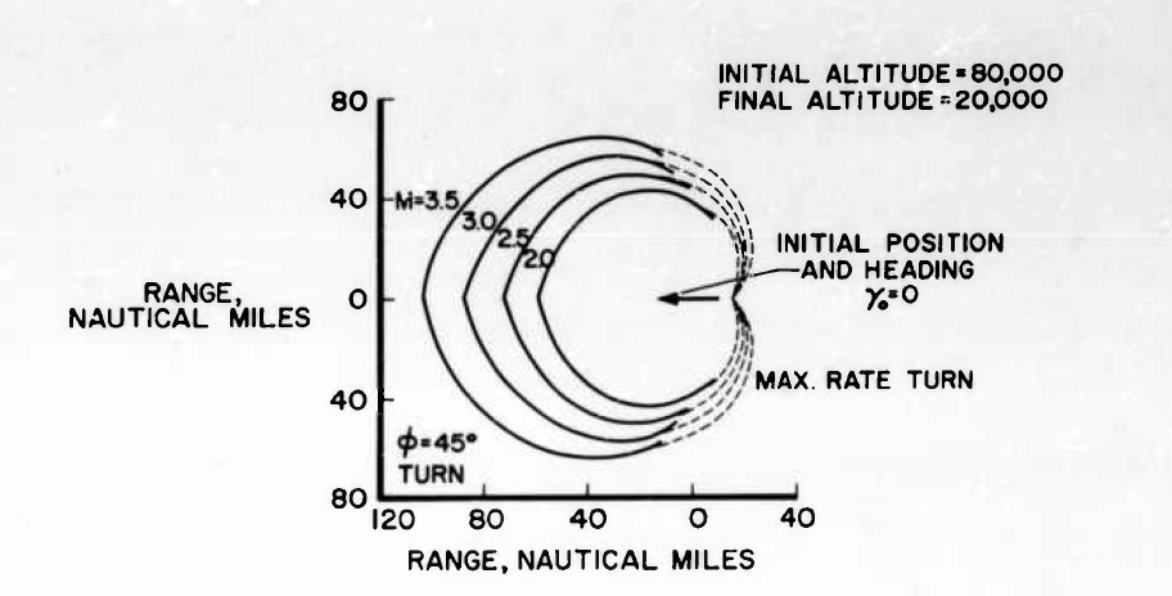

Figure 3 X-15 Lateral vs. Longitudal Range Plot During Gliding Flight [10]

Over the last half century, the land-based intercontinental ballistic missile (ICBM) and its sibling the submarine launched ballistic missile (SLBM) have successfully served as the top-

level strategic deterrent for national defense of the United States. References [12] and [13] provide a thorough review of the development, capability, and operational fielding of these weapon systems such as the Titan, Minuteman, and MX ICBM systems, and the Polaris, Poseidon, and Trident SLBM systems (see Figure 4 and Figure 5). These systems employ a traditional rocket to boost the payload along an orbital arc of global range, after which the payload follows a hypersonic reentry and flies along a piecewise non-maneuvering path to the target as shown in Figure 6. To increase effectiveness and survivability, advanced payloads with independent targeting known as multiple independently targeted reentry vehicles (MIRV), as seen in Figure 7, and maneuver capability known as maneuverable reentry vehicles (MARV) have also been fielded. [12] [13] Reference [14] discusses various engineering analysis methodologies to predict and design the performance and effectiveness of such systems. The ICBM and SLBM are a form of hypersonic weapon systems; however, they are considerably less versatile and adaptable when compared to the HGVs studied in this thesis.

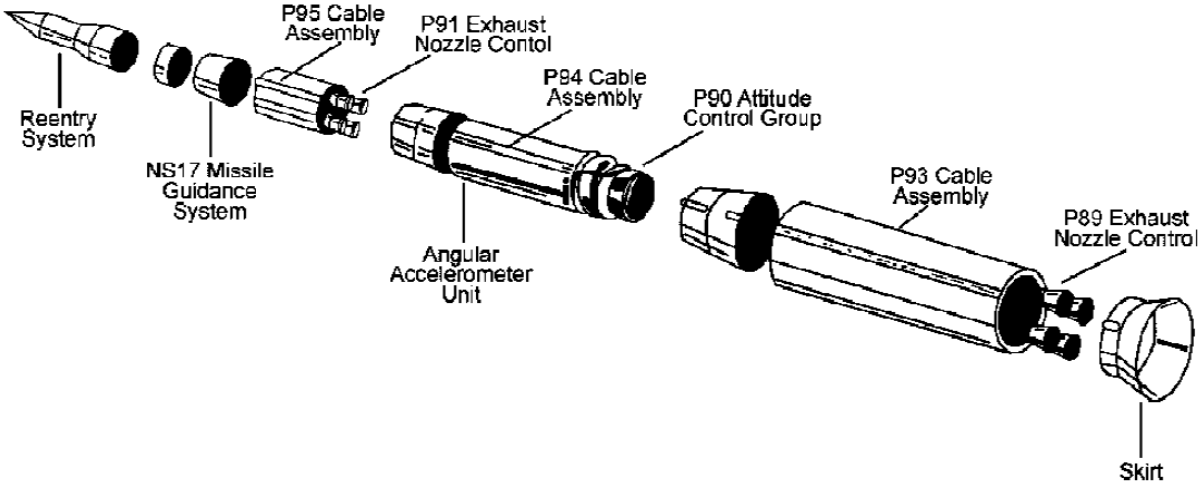

Figure 4 Minuteman II Exploded View [12]

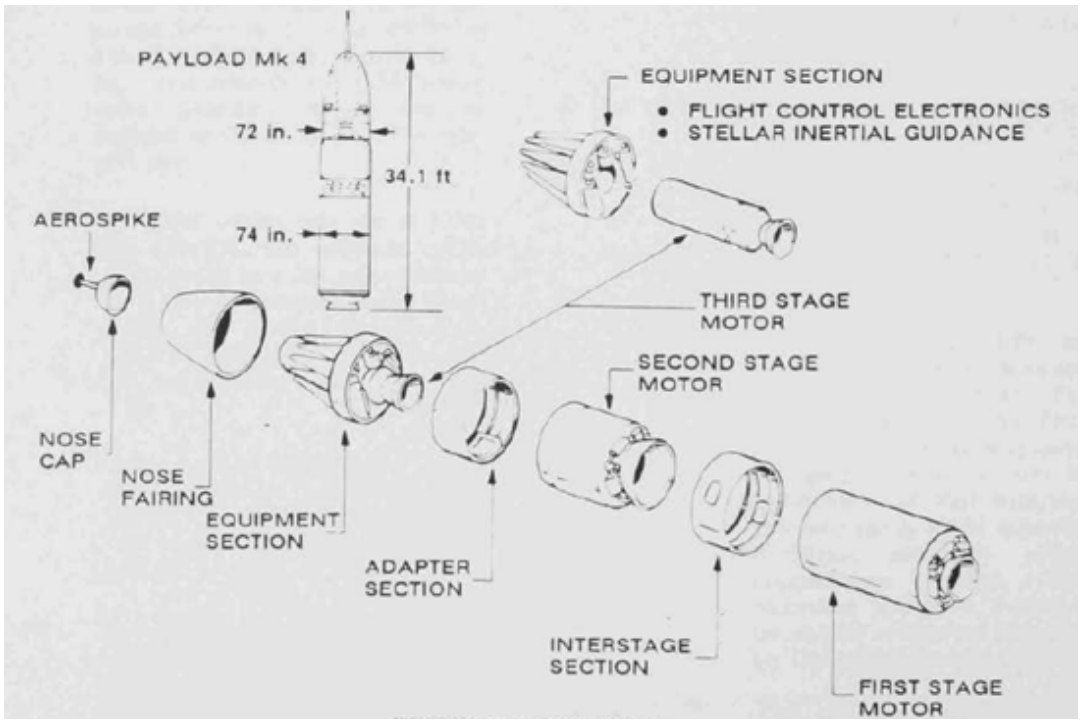

Figure 5 Trident Exploded View [15]

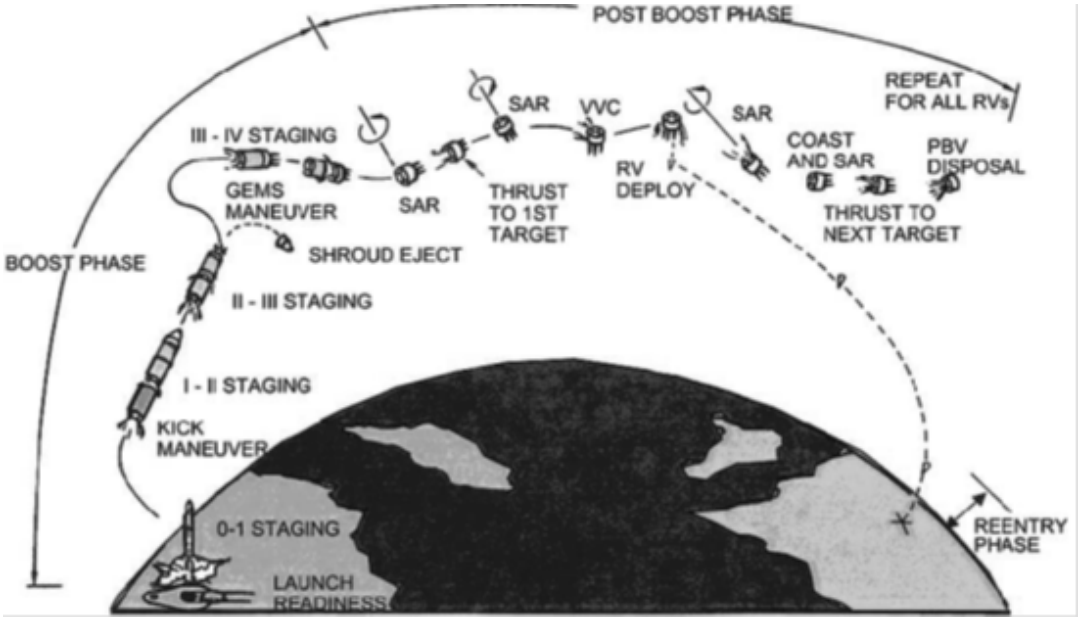

Figure 6 Typical ICBM Flight Sequence [12]

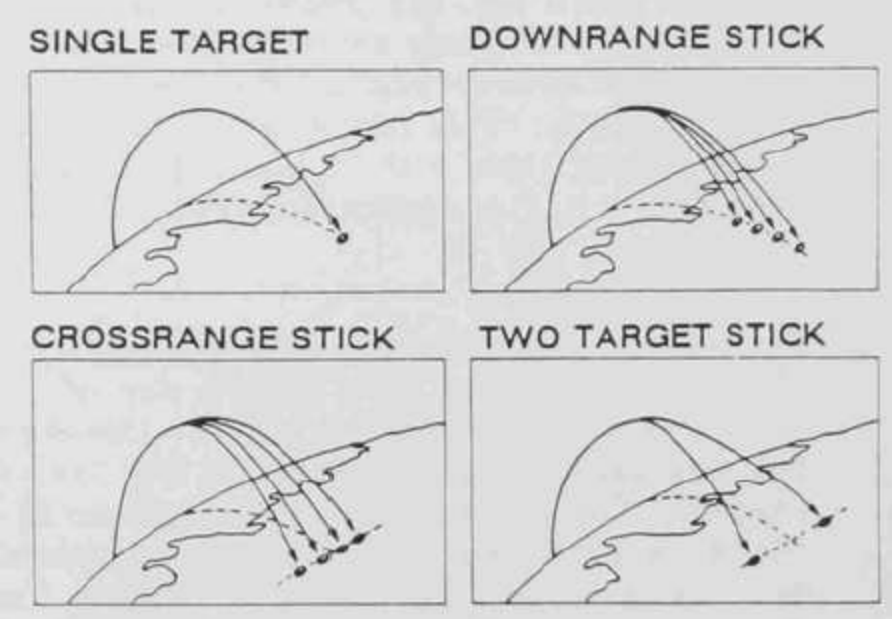

Figure 7 MIRV Capability [15]

To provide a complimentary alternative to the ICBM-SLBM, which is more versatile by providing precision strike with reduced collateral damage, rapid response with lower detectability, and alternative and adjustable attack routes, air and sea launched cruise missiles were developed and fielded in the later decades of the 20th century. References [16] and [17] offer an overview of these systems and the design challenges and trades that were involved in their development including the Boeing Air Launched Cruise Missile (ALCM) AGM-86B and the General Dynamics/Convair Sea Launched Cruise Missile (SLCM) Tomahawk AGM-109. The AGM-86B and the AGM-109 are shown in Figure 8. After launch, these systems operate much like an aircraft where the ALCM or SLCM cruises over long range to the target using lift surfaces and small turbofan propulsion to achieve the range performance. Mission profiles are commonly flown at subsonic speeds at low altitude achieving ranges on the order of 1,000 to 3,000 nm. Figure 9 shows a typical cruise missile strategic mission profile. As the target is

approached, the ALCM-SLCM can select alternate routes to the target with some capability to maneuver. Although not a hypersonic weapon, the cruise missile shares some common traits of HGVs regarding versatility and is thus important to mention in this thesis.

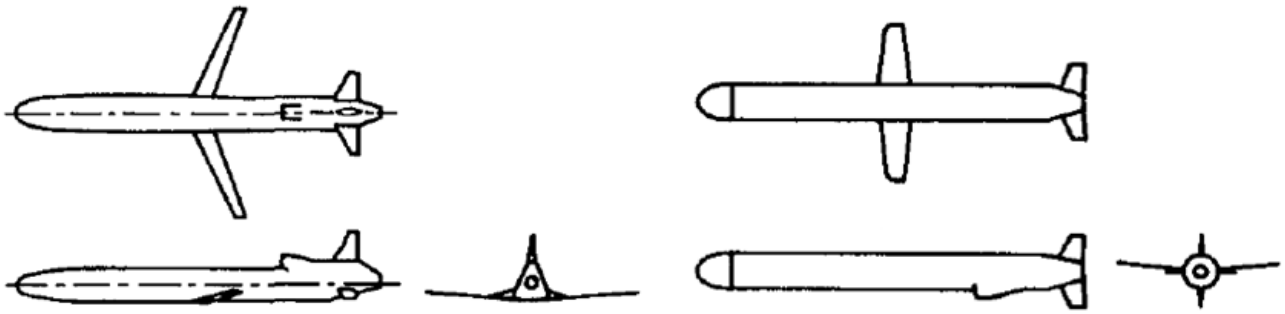

Figure 8 AGM-86B and AGM-109 [18]

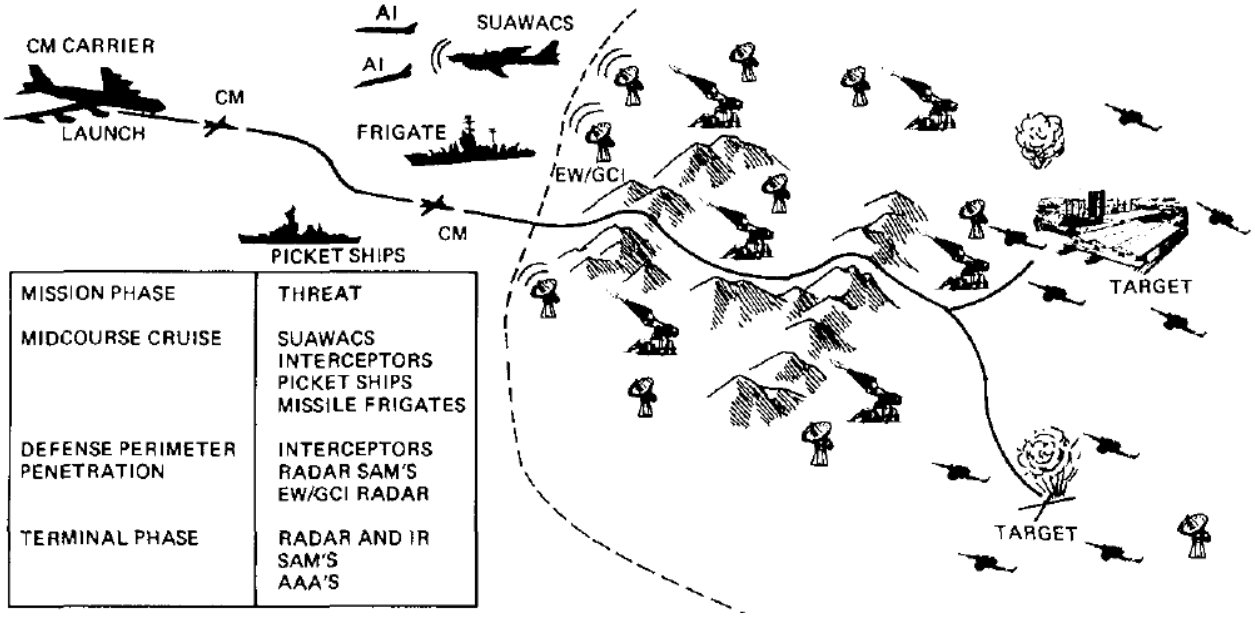

MISSION PHASE	THREAT
MIDCOURSE CRUISE	SUAWACS INTERCEPTORS PICKET SHIPS MISSILE FRIGATES
DEFENSE PERIMETER PENETRATION	INTERCEPTORS RADAR SAM'S EW/GCI RADAR
TERMINAL PHASE	RADAR AND IR SAM'S AAA'S

Figure 9 Typical Cruise Missile Strategic Mission Profile [18]

The X-43A Hypersonic Experimental Vehicle (Hyper-X) was a NASA research program that began in 1997 in collaboration with General Applied Science Laboratory (GASL) and Micro Craft to build three scaled-down test vehicles to investigate supersonic-combustion ramjet (scramjet) technology. The air-breathing, pure hydrogen fueled engine was built by GASL, with the lifting body built by Micro Craft. See Figure 10. The X-43A vehicles conducted three test flights with the first, launched in 2001, resulting in a mishap. The second and third test flights were successful. The X-43A was attached to a modified Pegasus first stage rocket and dropped from a B-52 at an altitude of 40,000 feet while flying at Mach 0.8. See Figure 11. During the X-43's third test flight in 2004 the rocket boosted the X-43 to test point at 110,000 feet where separation from the rocket occurred. The X-43 engine experienced 11 seconds of powered flight in which a speed of Mach 9.68 was achieved. An 800 nm controlled descent ended with splash down in the Pacific Ocean. An illustration of the flight profile is shown in Figure 12.

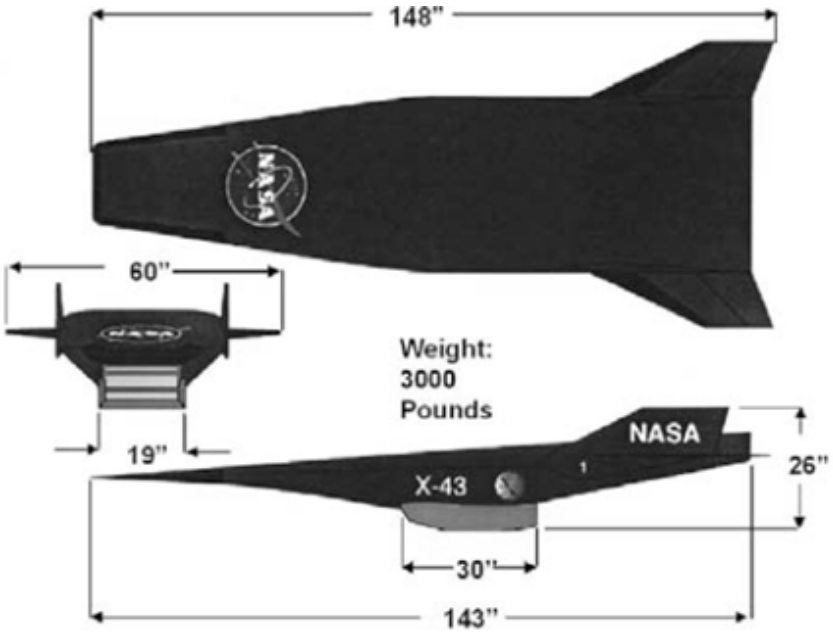

Figure 10 X-43 Scramjet Vehicle Geometry [19]

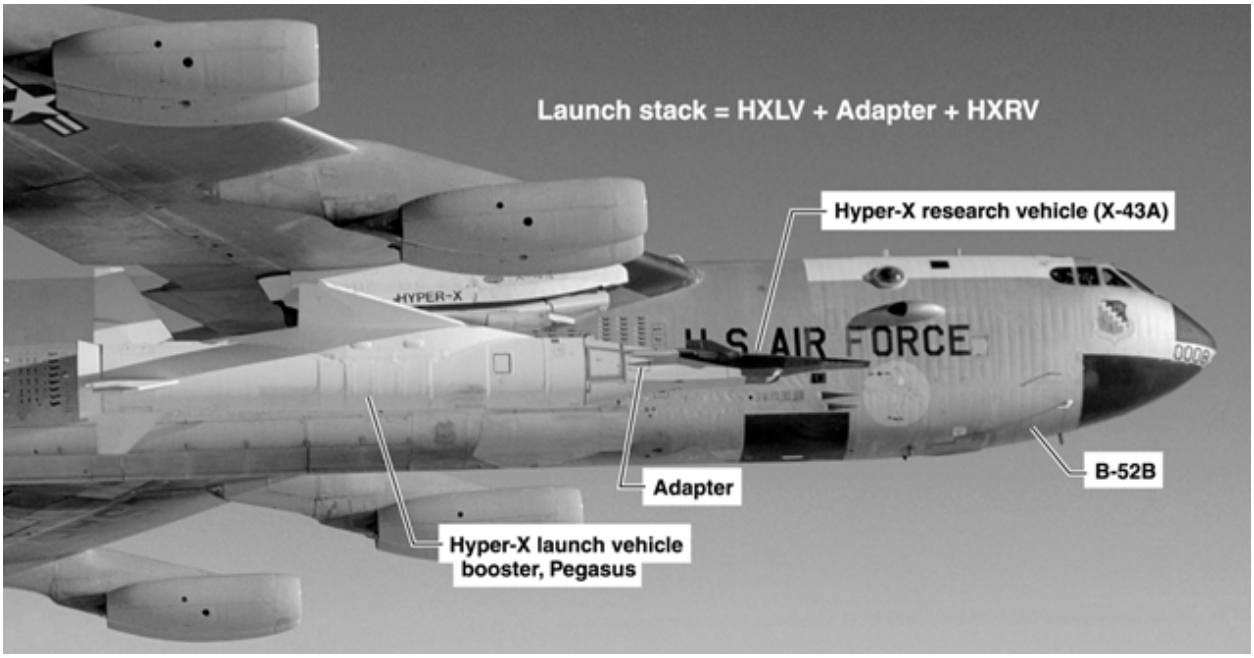

Figure 11 X-43A Mounted to Pegasus Rocket on B-52 Stratofortress [20]

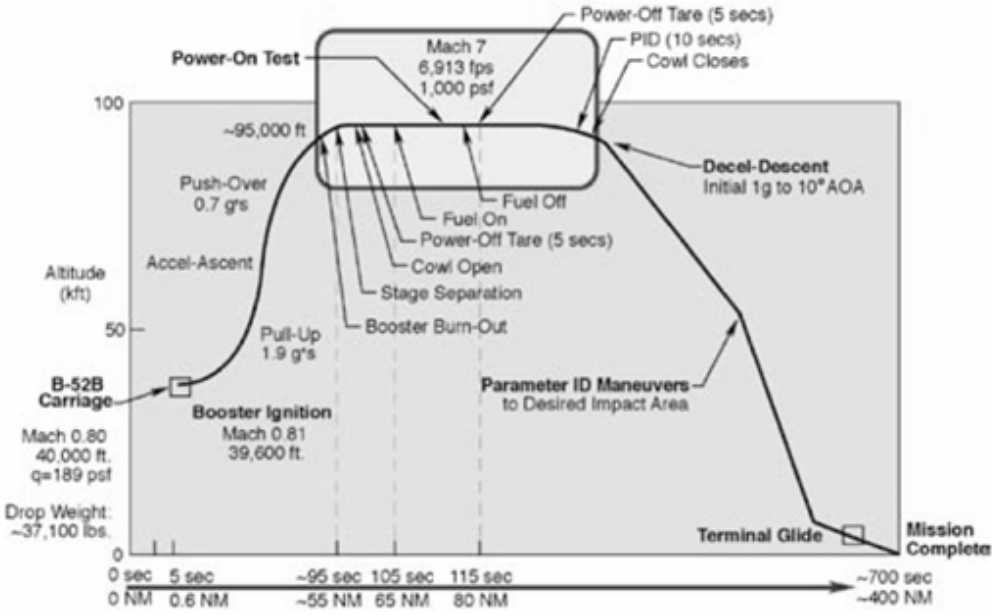

Figure 12 X-43A Flight Profile [19]

As a follow-on program to the X-43A, the USAF began working with NASA on the X-43C. The X-43C was to use a hydrocarbon-fueled scramjet engine (HyTECH) as opposed to a pure hydrogen fueled engine. Reference [21] discusses operational benefits that can be found from using a hydrogen or hydrocarbon-fueled engine. The Air Force Research Lab (AFRL) contracted Pratt & Whitney to develop the engine which, after the cancellation of the X-43C, would eventually be used on the X-51 Waverider shown in Figure 13. Like the X-43A, the X-51 would be dropped from a B-52 while attached to a solid rocket booster, in this case an Army Tactical Missile System (ATACMS). See Figure 14. The flight profile for the X-51, shown in Figure 15, is also similar to the X-43A. Four flights were conducted with the final flight occurring in 2013 with the X-51 traveling at Mach 5.1. [22]

Figure 13 X-51A Waverider Scramjet [23]

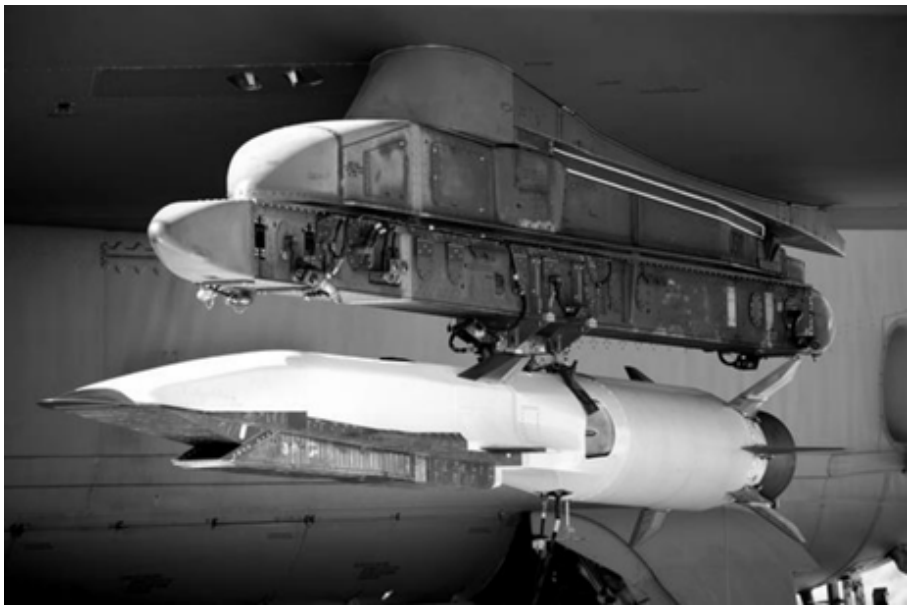

Figure 14 X-51 Attached to ATACMS on B-52 Stratofortress [22]

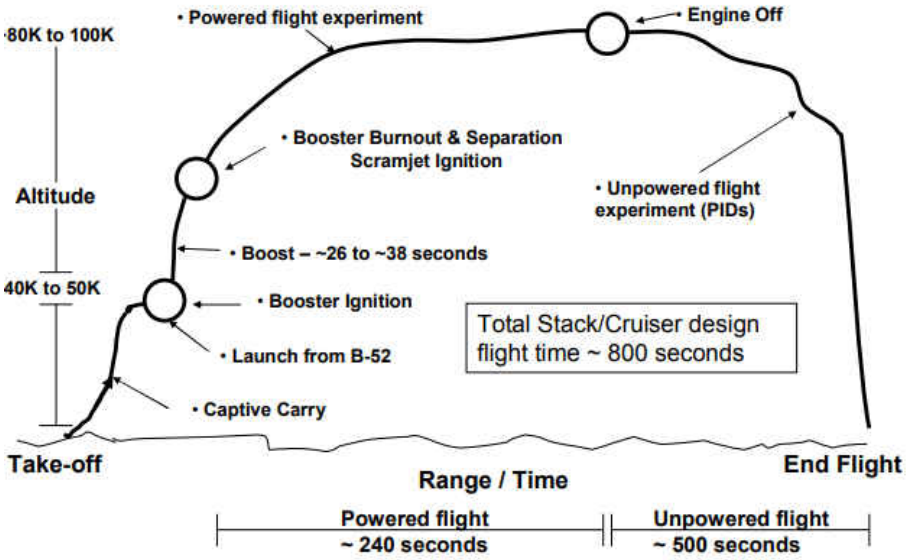

Figure 15 X-51 Flight Profile [24]

HGVs represent a class of weapon that can travel at Mach 5 or greater, combining the speed of a ballistic missile with the maneuverability of a cruise missile. Designs for HGVs

usually consist of a supersonic compression ramjet or scramjet, requiring that the vehicle be launched by a first stage rocket booster. The first stage can be launched from the land or sea like a ballistic missile, or dropped from an aircraft and ignited like a cruise missile. After the vehicle has reached supersonic speeds the first stage detaches and the scramjet is fired. During hypersonic cruise, HGVs generate compression lift by riding on their own shock waves allowing them to greatly extend their range. HGVs have a range comparable to that of a MaRV, upwards of 10,000 to 15,000 km as indicated in Figure 16. Taking Norfolk Naval Station (NNS) as a potential ground target, observe from Figure 17 that an HGV could be launched from anywhere in Europe or Asia and easily reach the NNS position.

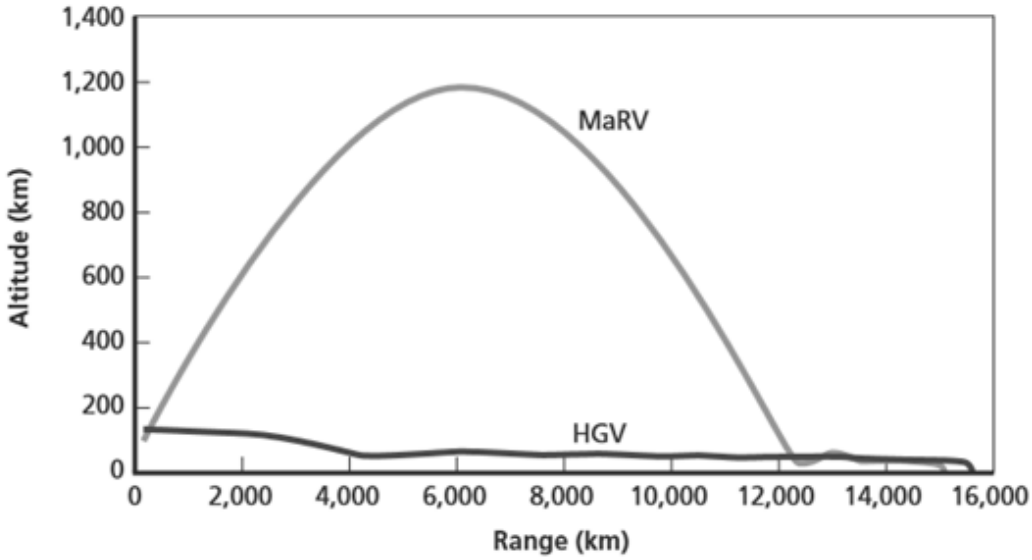

Figure 16 MaRV vs. HGV Approximated Range [25]

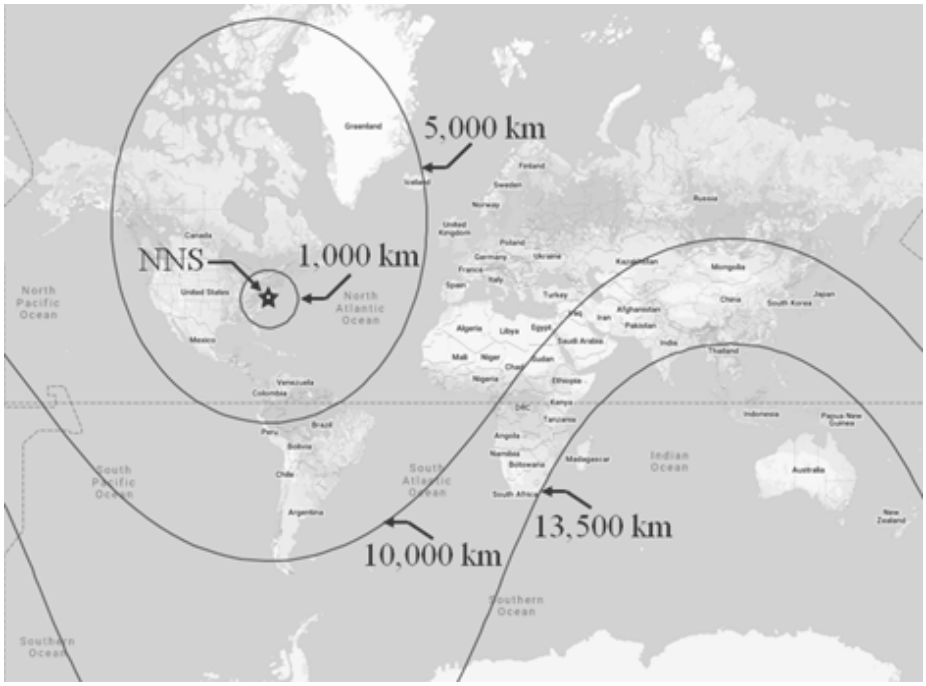

Figure 17 Range Map from Norfolk Naval Station

Another characteristic of HGVs is that they can be maneuvered laterally and vertically. HGVs achieve maneuverability either by actuated tail fins, such as the X-51 Waverider or by rear control thrusters, such as the Hypersonic Technology Vehicle (HTV-2). With this maneuverability, HGVs are able to perform skip-glide maneuvers to extend downrange target access, as well as lateral maneuvers to suppress countermeasures or enhance crossrange target selectability. The lateral maneuver characteristic of HGVs is similar to that of cruise missiles. They can perform numerous lateral maneuvers to hinder an adversary's ability to determine the final ground target location. This hindrance in turn makes HGVs difficult to counter with traditional anti-ballistic missile technology since the required flight path to intercept the HGV target can change any given number of times within the vehicle's initial parameters of fuel, altitude, speed, and heading as characterized in Figure 18.

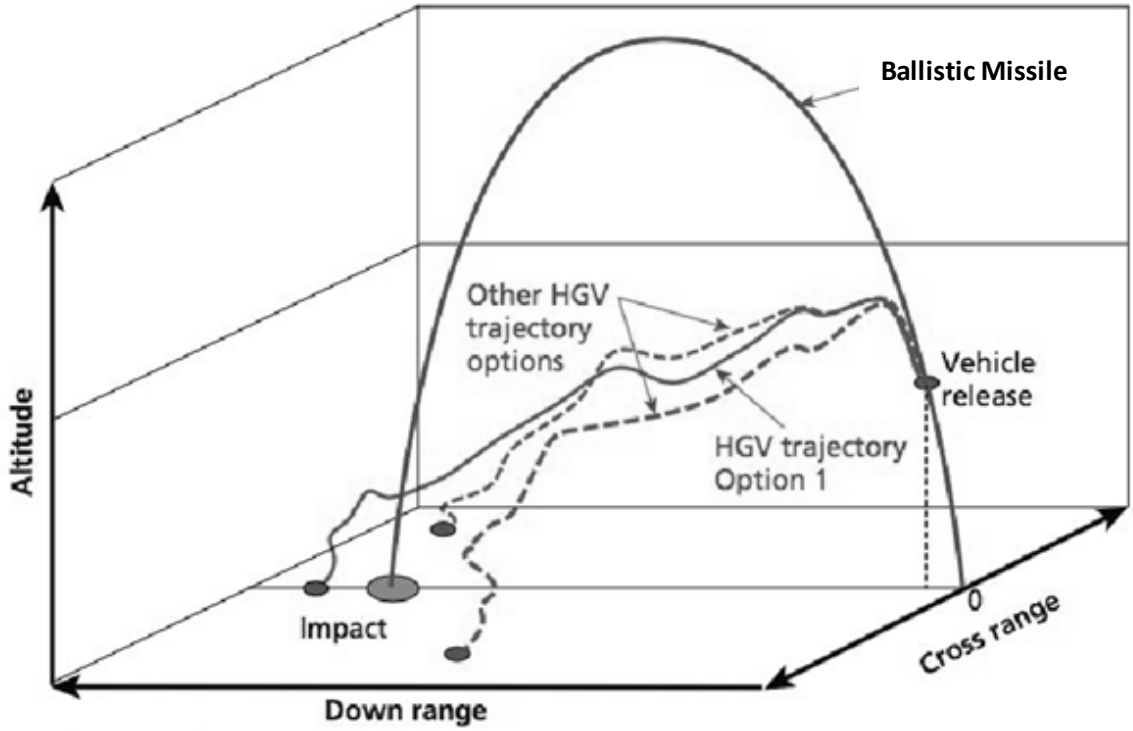

Figure 18 Ballistic Missile vs. HGV Flight Path[25]

The flight of an HGV is comprised of several phases; the first two phases are similar to a traditional flight path for an ICBM, beginning with a powered boost phase, followed by an unpowered ballistic phase. Figure 19 depicts the ballistic phase (the velocity, flight path angle, and downrange angle variables will be defined in Chapter 3. [26]) As the HGV completes its ballistic phase following an elliptical trajectory returning to the more dense upper atmosphere it begins a direct reentry phase followed by a pull-up phase as shown in Figure 20. The lift, drag, and weight forces shown in the Figure 20 will be developed in Chapter 3. During the pull-up phase, depending on the angle of attack, the HGV can move directly into the glide phase illustrated in Figure 21 where it performs a shallow descent into the atmosphere, or it can

execute a skip maneuver in which the HGV exits the dense atmosphere and begins a second ballistic phase. [27] [28] The HGV can execute multiple skips thus prolonging the time of flight and extending its range. After executing the final skip and glide phases the HGV will enter into a dive phase to acquire its target. [29] HGV characteristics reviewed in this section are inherently tied to this thesis.

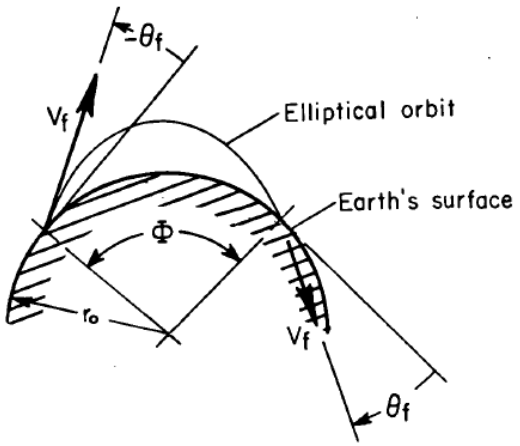

Figure 19 HGV Ballistic Phase [27]

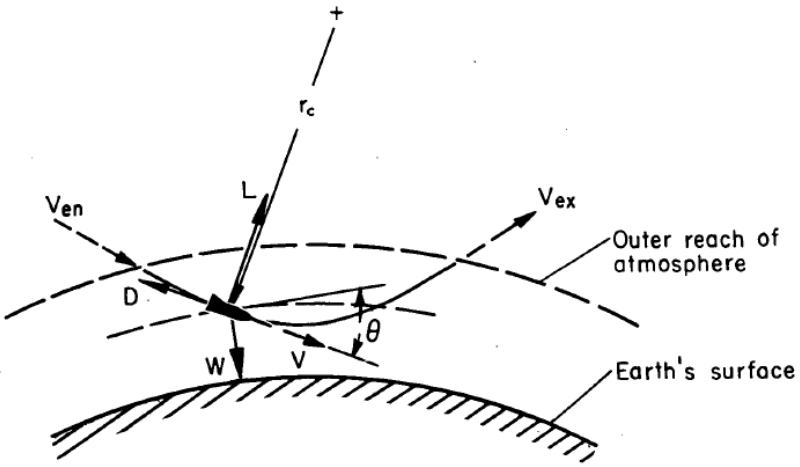

Figure 20 HGV Reentry and Pull-Up Phases [27]

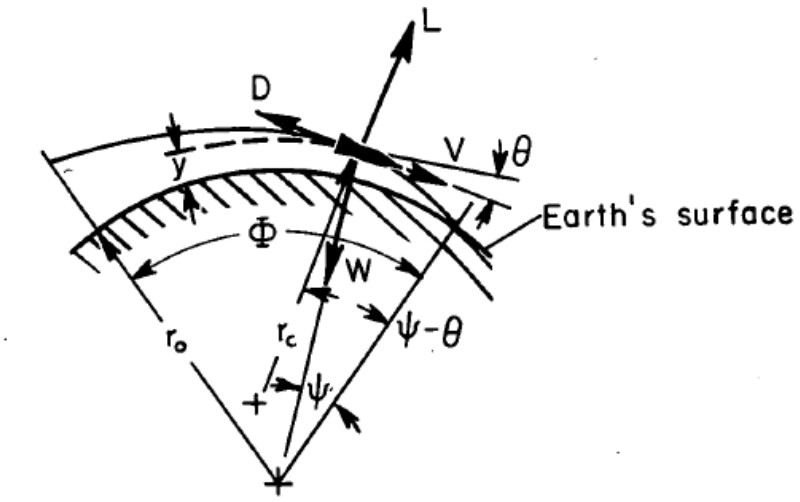

Figure 21 HGV Glide Phase [27]

1.2.2 Laser Weapon Systems

Traditional weapon systems such as guns, cannons, and missiles utilize kinetic energy. A cannon shell can be several meters off target and still have lethal effect on its intended target. However, a laser weapon system requires exceptional pointing precision, not only to track the target but also to maintain focus on a specific spot within its line of sight (LOS). Compounding this problem is the nature of the target. If the LWS is focused on a spot on the target that is non-critical to its operation, say the bumper of a truck vs. the engine compartment, then the laser will have little to no effect. In the same scenario a cannon shell or missile will result in massive damage regardless of the spot it hits. Further, if the critical spot on the target is not well defined or hardened, say the nose cone of a cruise missile, then the LWS will have minimal effect. This factor is one reason why power is above all the greatest challenge to LWSs. LWSs are a sub-category of Directed Energy Weapon Systems (DEWS), which also include highly focused energy such as microwaves and particle beams. Reference [30] is an overview of the system design characteristics for LWSs, high powered microwave weapons (HPMW) and particle beam

weapons (PBW). Of the three forms of DEWS, LWSs are the most technologically advanced and most widely deployed within the U.S. military. Reference [31] describes the various types of lasers including the various permutations of chemical lasers, as well as solid state lasers, fiber lasers, and free electron lasers. Of the laser types, chemical lasers have received the most attention in previous decades because of their ability to obtain high power outputs.

In 1976 the United States Air Force (USAF) converted a NKC-135 Stratotanker into the Airborne Laser Lab (ALL). The ALL featured a 456 kW chemical laser with CO_2 - N_2 - H_2O propellants and operated at a wavelength of 10.6 μm. [32] The ALL main beam director assembly (BDA) was located on the dorsal section of the fuselage forward of the wings as shown in Figure 22. The ALL successfully shot down five AIM-9 missiles and one BQM-34A Firebee drone. In 1977 the Soviet Union began a similar airborne laser effort by converting an Ilyushin Il-76MD transport aircraft into the Beriev A-60 Laser Lab. The A-60, shown in Figure 23, featured a retractable turret of unknown power as well as a nose mounted targeting laser. As discovered during testing of the ALL, thermal blooming, or the localized heating of the air pockets due to varying levels of air density in the atmosphere along the beam path between the BDA and the target, can lead to issues with attenuation and defocusing of the beam. Other atmospheric conditions including aerosols, moisture, and dust were also found to affect LWS performance. [30]

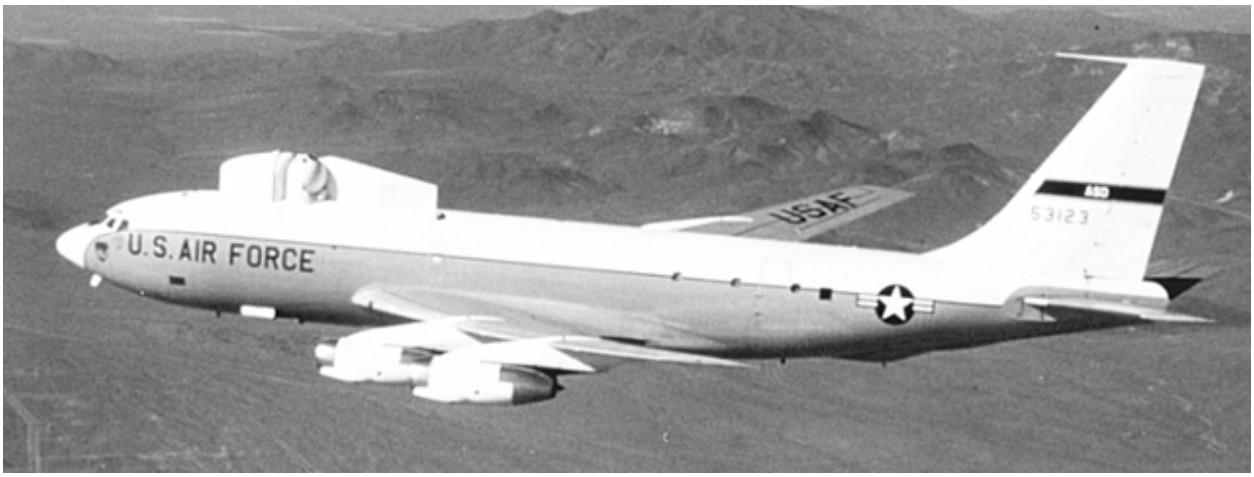

Figure 22 NKC-135A Airborne Laser Lab [32]

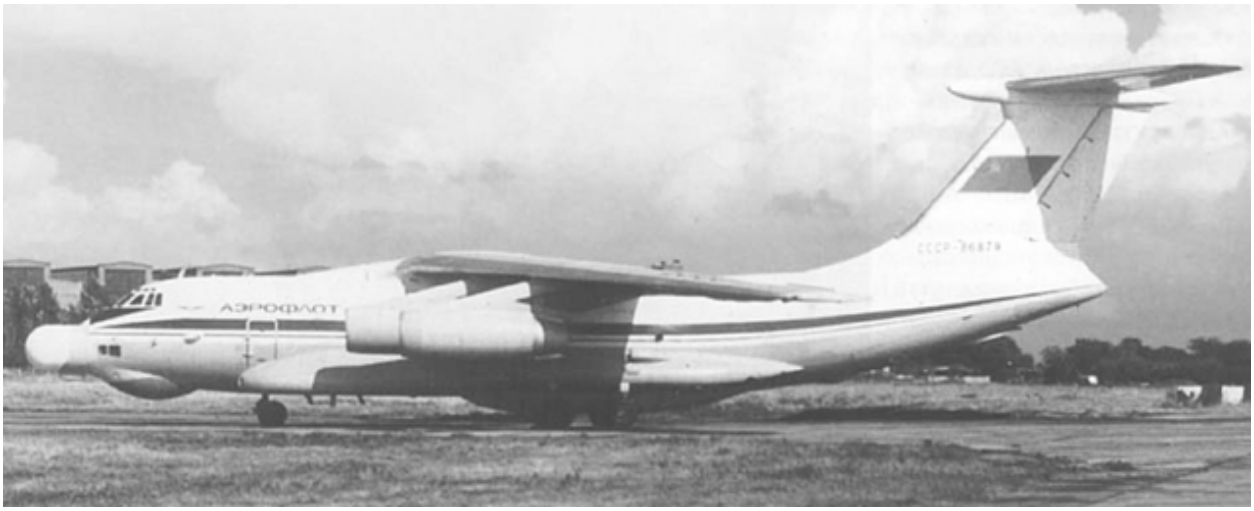

Figure 23 Beriev A-60 Airborne Laser [32]

Advancing from the progress made with the ALL, the USAF continued laser development with the Boeing YAL-1 ABL which was a modified Boeing 747-400 aircraft with a megawatt-class high energy laser (HEL). [33] The HEL was a COIL invented by the USAF in 1977 and housed within the fuselage of the 747, the COIL operated as a continuous wave laser

with a wavelengh of 1.315 μm. The BDA for the ABL replaced the nose of the aircraft as shown in Figure 24. The arrangement of the BDA by Boeing is similar to the Soviet Beriev A-60 targeting laser nose fairing which precede the YAL-1 by several decades. [32] The ABL featured six laser modules with the entire system weighing approximately 200,000 lbs. [34] To partially address the issue of thermal blooming the ABL made use of adaptive, or deformable, mirrors. A representative engagement scenario is shown in Figure 25. The YAL-1 successfully shot down two representative missiles in 2010, requiring between 90 and 500 seconds of lasing depending on the distance from the target. Although the YAL-1 program was cancelled in 2012 the laser technology demonstrated on the airborne platform over three decades has opened the door to a new generation of LWSs. Though this thesis research focuses on space fielded systems, the past ALL and ABL airborne concepts are inherently related.

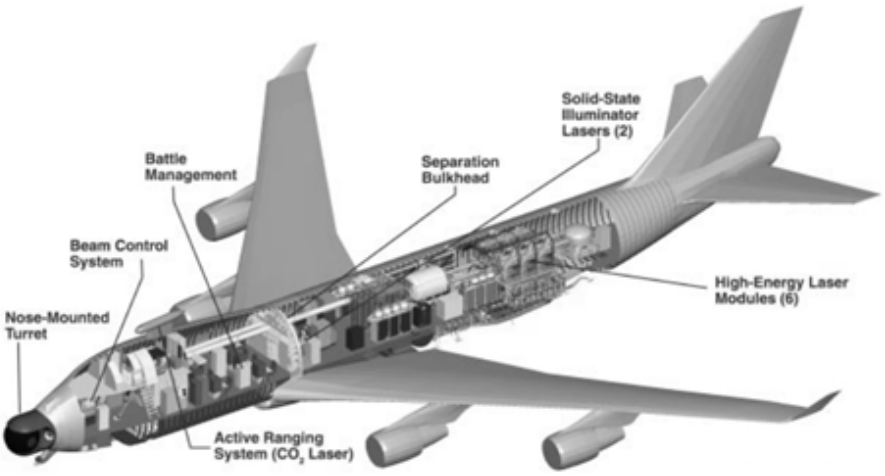

Figure 24 Boeing YAL-1 Airborne Laser [32]

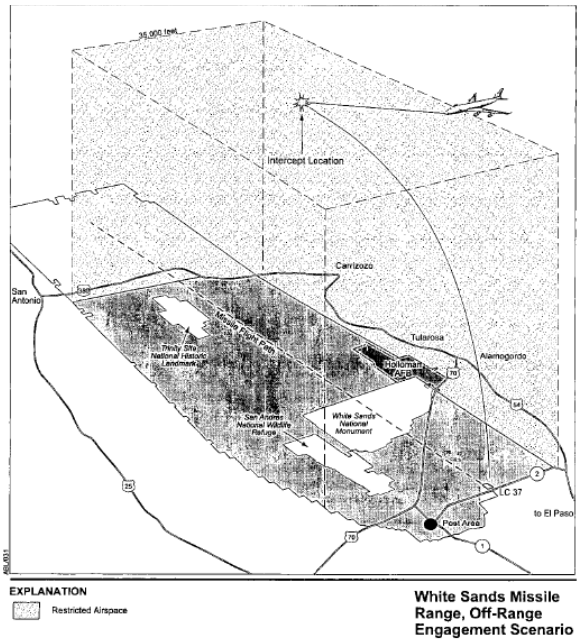

Figure 25 Boeing YAL-1 Engagement Scenario [35]

The Tactical High Energy Laser (THEL) which would be transitioned into the Mobile THEL (MTHEL) shown in Figure 26, was a joint US/Israeli ground based LWS initiated in 1996. MTHEL featured a deutrium-fluoride chemical laser with a 3.8 μm wavelength. Between 2000 and 2004 MTHEL destroyed 28 122 mm and 160 mm Katyusha rockets. [32] Additionally, MTHEL was the first LWS to destroy artillery shells, mortar rounds, and counter a three round mortar salvo in a single engagement. MTHEL was envisioned as a point defense system to protect an area against an incoming threat as represented in Figure 27. Like the airborne chemical laser before it, MTHEL was eventually cancelled in 2004 due to concerns about its size and cost.

Figure 26 Tactical High Energy Laser [36]

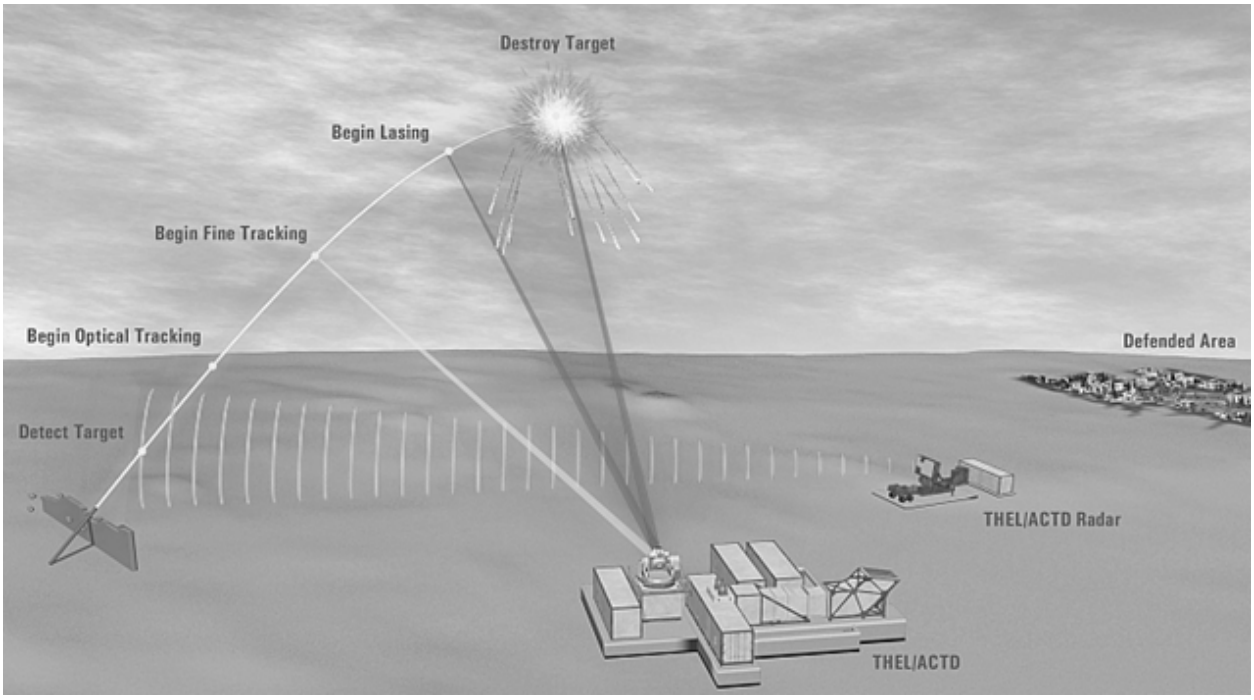

Figure 27 Tactical High Energy Laser Engagement Scenario [32]

Miniaturization of LWS technology has been a driving focus of U.S. military research and tactical deployment efforts across the armed services. Currently, all branches of the Department of Defense (DoD) have efforts underway to test and deploy LWSs with most efforts shifting toward solid state lasers (SSL); the Navy has developed an incremental approach as shown in Figure 28. This approach is being implemented in three increments to evolve LWSs and is described as follows:

> *Increment 1 is the 60 kW HELIOS laser being installed on ships to destroy drones and cripple small attack craft;*
>
> *Increment 2 will ramp up the power enough to take side shots against cruise missiles, so a ship with it installed can use it to defend other ships nearby but not itself; and*
>
> *Increment 3 will be still more powerful, able to burn through the nose-cone in a head-on shot, allowing a ship with it installed to defend itself.* [37]

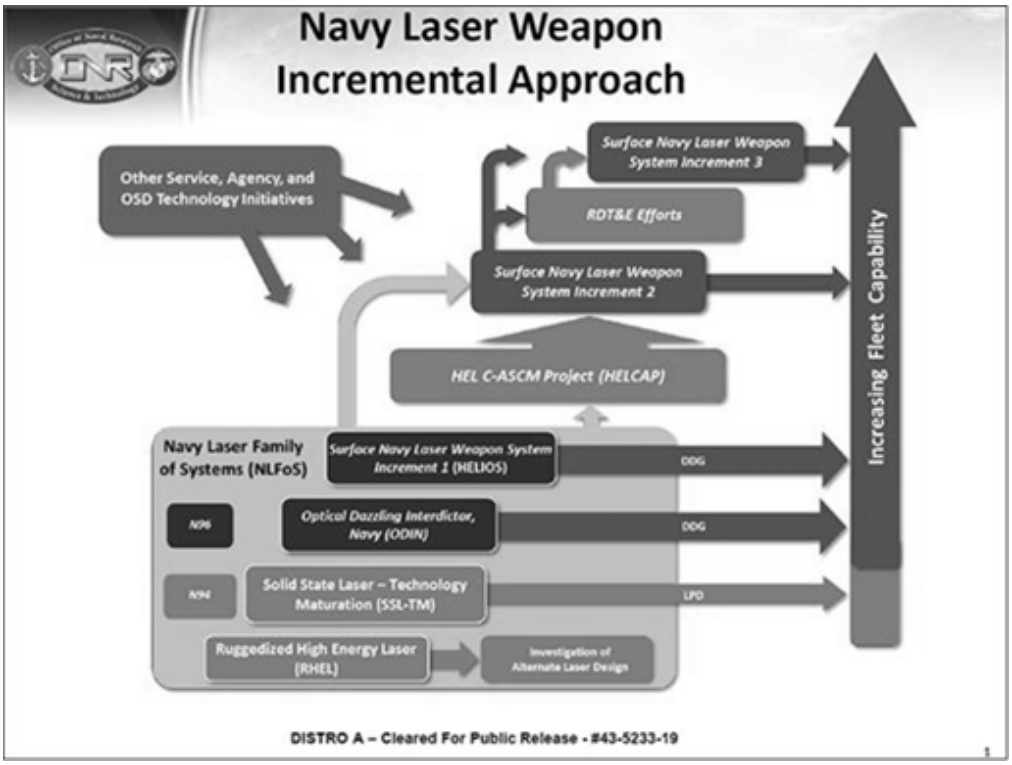

Figure 28 US Navy LWS Incremental Approach [37]

Although decades of research and funding have been spent in the study and testing of chemical lasers, most new efforts are now focused on SSLs. While chemical lasers have proven effective at countering missiles, rockets, artillery shells, and mortar rounds, their high cost, large size, and use of toxic chemicals has made them lose favor. SSLs, unlike chemical lasers, produce their beams by passing electricity through crystal or glass. This beam generation method is advantageous from a weapon perspective, as described in Reference [38], since the only ammunition or fuel for the weapon is electrical power and the logistics of hazardous chemical waste is eliminated. A drawback to SSLs is waste heat management, which in chemical lasers heat management is achieved through the working chemical fluid. Land and sea-based SSLs primarily rely on chilled water to cycle their waste heat. As described in Reference [39], thermal management systems (TMS) often constitute 50% or more of the weight budget for

SSLs. Current development efforts are focused on scaling up the power capacity of SSLs while reducing the TMS footprint.

As shown by the ALL, the tactical use of mobile lasers requires the consideration of a number of internal and external factors to be effective against a target. Factors inherent to the internal system design include power output, tracking, targeting, cooling, beam control, and many others. Chief amongst these is power output, the metric for which LWSs are rated with respect to their radiant power output. The effective range of a laser is proportional to the power output. LWS performance is also impacted by optical beam control, which is the ability to position the centroid of a laser on the target. Optical jitter, motion caused by platform motion and LWS component motion, can negatively affect the optical beam. Small level relative motion between mirrors and lenses can degrade the performance of precision pointing systems. Sources contributing to optical jitter include thermal effects, mechanical vibration, acoustics, static and dynamic loading, and heating and cooling systems as described in References [40] and [41] .

1.3. Space-Based Laser

In 1999 the USAF and Ballistic Missile Defense Organization (BMDO) began a joint venture with TRW, Lockheed Martin, and Boeing to develop the SBL Integrated Flight Experiment (IFX). The SBL IFX was a technology demonstrator leveraging previous research in high energy lasers to test the feasibility of placing an LWS on an orbital platform. The SBL IFX was a megawatt class hydrogen fluoride chemical laser with wavelength between 2.7 and 2.85 µm. The SBL IFX had a total mass of 22,900 lbm and featured a 2.8 m beam director as shown schematically in Figure 29. Details of the characteristics of the systems are described in

References [42] and [43]. A depiction of the engagement profile for the SBL is represented in Figure 30, in which the SBL IFX objective was to strike down an ICBM test article during the boost phase when the missile was under significant aerodynamic stress and most vulnerable. [44] The SBL IFX was planned to be succeeded by a constellation of 20 satellites with ground coverage able to protect a large portion of the globe from ICBM launches as shown in Figure 31.

Placing an LWS on an orbital platform would pose unique challenges compared to those faced by terrestrial based LWS systems. While land and sea-based systems can be positioned defensively around high value assets, an orbiting LWS target may only be in range for a fraction of its orbital period, thus requiring a constellation. A study described in Reference [45] to adequately cover potential launches from northern Asia for instance, would require a satellite constellation of between 71 and 90 satellites at altitudes between 367 to 470 km. This constellation would result in at least 3.6 satellites directly over northern Asia at any time. This study did not consider local distribution fluctuations caused by orbital motion, but it does show that adequately protecting a large area greatly increases the number of required satellites as would be expected. When initially proposed, the SBL constellation was not envisioned as the sole defensive mechanism to counter the ballistic missile threat but as a part of the greater defensive strategy. [44] This strategy consisted of a layered defense for countering ballistic missiles grouped by the kill point in which the defensive system was to operate including Boost, Midcourse, and Terminal Phase kill points as shown in Figure 32. The SBL IFX program was cancelled in 2002; however, with the Russian deployment of the Avangard HGV in 2018, many elements of the SBL are being revisited and are intrinsic to the research focus.

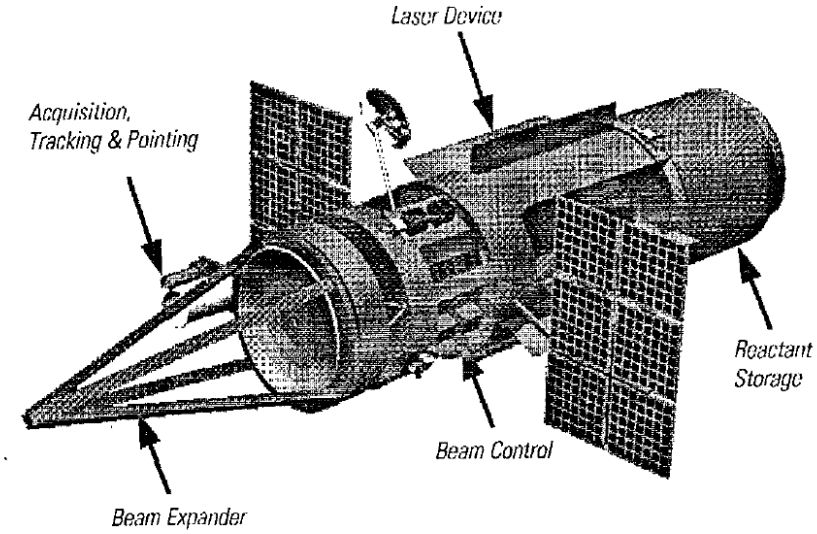

Figure 29 Proposed BMD Space-Based Laser [46]

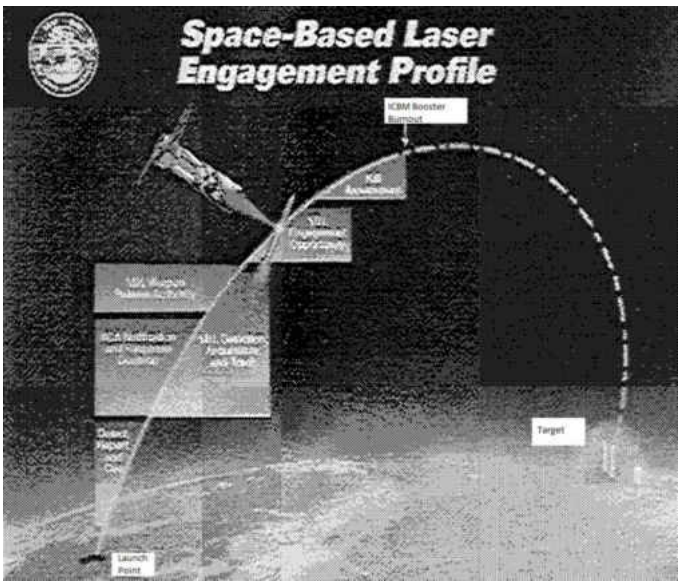

Figure 30 SBL IFX Typical Engagement Profile [44]

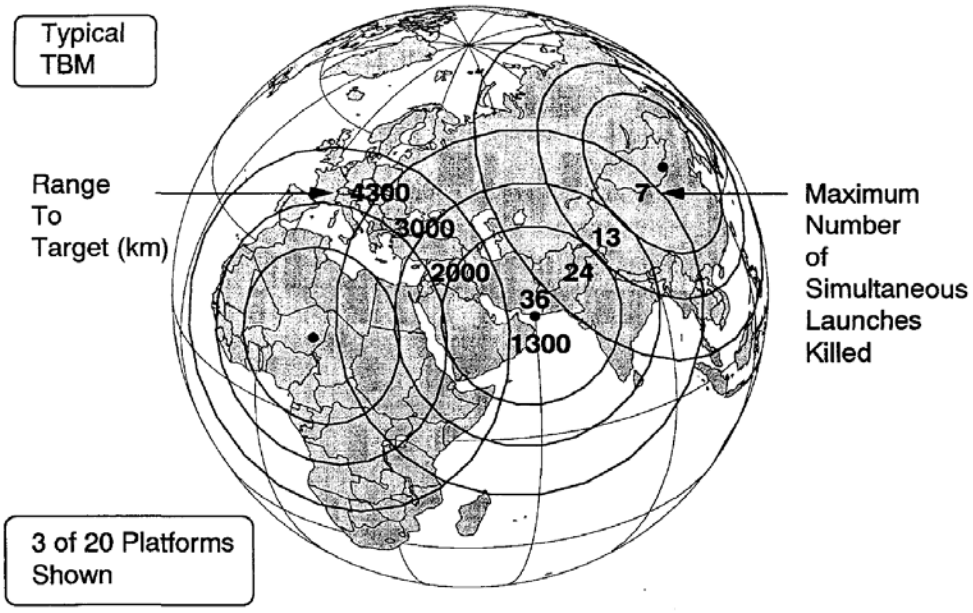

Figure 31 SBL Constellation Coverage [46]

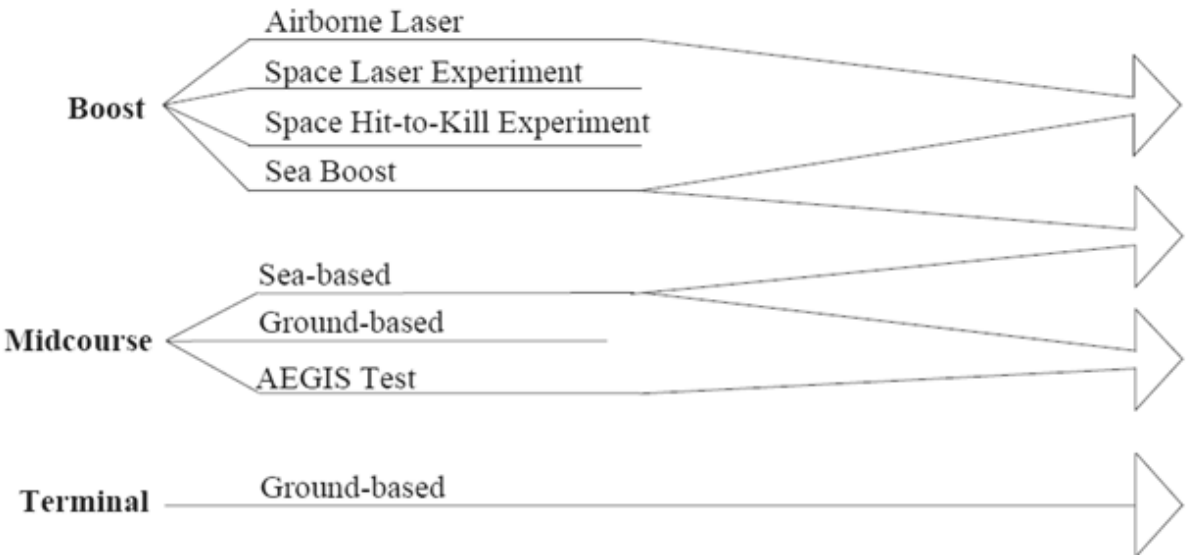

Figure 32 Ballistic Missile Defense Efforts [47]

1.4. Problem Statement

The purpose of this work is to investigate the methodology for determining what set of initial conditions will allow a space-based laser weapon system to acquire and counter a hypersonic glide vehicle moving toward a ground target, with each vehicle having its own dynamic state. While complete global coverage would require numerous satellite-based LWSs, determining initial conditions under which select geo-locations can be protected would be advantageous to protecting military assets. This determination is twofold: first identifying if target acquisition and counteraction is feasible, and second, when it is feasible, estimating the domain of conditions and the quality of those conditions for successful engagement. An important part of the investigation is development of a computational tool that can generate answers to these questions efficiently and accurately for a wide array of situations. The tool is envisioned either for utilization as a fielded decision support aid or a high-level planning aid.

1.5. Assumptions

1.5.1 Overall

In developing the governing equations, several assumptions have been made to simplify their calculation. Not all of these assumptions are conservative in nature and real-world results would differ. The following assumptions are of a generic nature to the setup of the problem.

1) A spherical earth is considered. This assumption is made to simplify calculations related to ground track and HGV target acquisition. As a result of this non-conservative assumption ground track for the idealized orbit will differ from the actual ground track—more significantly at the equator and poles than at other regions of the earth.

2) Atmospheric effects are ignored with respect to the satellite. An isotropic atmosphere is assumed for calculations related to the HGV. This assumption is made to simplify calculations related to the motion of the satellite and the HGV.
3) In the calculation of the orbiting bodies an idealized undisturbed motion has been assumed. In reality, large masses such as the Sun, Jupiter, and Saturn affect the motion of a satellite orbiting the Earth. This assumption has been made to simplify calculations related to satellite orbit. As a result of this non-conservative assumption, the idealized orbit will differ from the actual orbit.

1.5.2 Laser Weapon System Representation

The system performance of the LWS has been simplified to a binary line of sight (LOS) method. If the HGV is within the LOS of the LWS and in range of 1000 km or less, it is said to be *disabled*. This implementation has the effect of ignoring such system parameters as target track, beam power output, training, fast mirror steering, steady state error (jitter), etc. Additionally, external factors such as atmospherics, thermal blooming, and dispersion are also ignored. This assumption is made to simplify the calculation of the LWS to HGV interaction. Given the number of variables involved in LWS performance, a detailed physics model would be required to accurately represent the interaction, which is beyond the scope of this study.

1.5.3 HGV

The following assumptions were made with respect to the Hypersonic Glide Vehicle.

1) Given that an HGV can be launched from ground or air assets, the flight of the HGV will be limited to a single skip and glide phase. Limiting the HGV to a single skip-glide flight segment is meant to approximate fuel limitations, assuming the mass of the vehicle is

constant throughout that time of flight. By only accounting for skip and glide, this also ignores the boost and initial ballistic phase of a ground launch. Additionally, reentry, pull-up, and dive phases are ignored. This is because in determining the range of the HGV, the skip and glide phases are predominant in their contributions to the total range calculation compared to the other phases. [27] [28]

2) Only vertical motion is considered. In reality, HGVs are able to maneuver laterally. Given that the range limits for HGV lateral motion will be significantly smaller than the vertical motion limits – since lateral motion sacrifices range – this assumption is considered conservative.
3) Heating of the HGV surface is ignored. In reality, thermal heating due to the atmosphere acts as a boundary condition for HGV performance.

1.6. Thesis Outline

This research work includes the design methodology for determining the conditions under which a space-based laser weapon system can engage and neutralize a hypersonic glide vehicle. Chapter 2 discusses the design methodology, examining the initial conditions and boundary conditions involved. Chapter 3 examines the equations of motion for the HGV and satellite. Chapter 4 provides an overview of the simulation including the code framework and key functions involved in the solution. Chapter 5 presents the case study results. Lastly, Chapter 6 provides research conclusions and recommendations for further investigation.

CHAPTER 2

DESIGN METHODOLOGY AND MODEL DEVELOPMENT

2.1. Approach

Analysis was approached from the perspective that several components of the defensive layer as shown in Figure 32 and discussed in Reference [47] would not be capable of countering an HGV due to the novel characteristics exhibited by these new weapon systems, specifically the speed and skip-glide capabilities described in Chapter 1. As a result of the capabilities exhibited by HGVs, existing hard-kill interceptors will not succeed in terminating HGVs as acknowledged by Michael Griffin, Under Secretary of Defense for Research and Engineering. [48] In this investigation the space-based laser (SBL) portion of the defensive layer is examined in isolation to determine its effectiveness.

2.2. Objectives

The present strike and defend scenario problem as outlined can be deconstructed into two parts, the evader and the pursuer. The evader, or HGV, has the goal of reaching the ground target before it is countered by the pursuer or SBL. The evader has been restricted to a series of set flight paths, performing one skip-glide maneuver per flight. The strike profile path begins with the HGV being launched on a first stage booster and proceeding into a ballistic skip phase. The HGV re-enters the atmosphere and continues on a glide phase trajectory to the ground target, ignoring the reentry and pull-up phases discussed earlier. The HGV completes the same scenario altering the longitude and latitude coordinates of its starting launch location. This process continues in a circular fashion around the ground target. Additionally, the launch angle of attack and initial velocity ratio are varied during each iteration.

The pursuer has the goal of countering the HGV before the HGV can reach the ground target. A nearly circular fixed orbit is defined for SBL, but the right ascension of the ascending node and true anomaly are allowed to vary with each flight path iteration of the HGV. This variation allows the orbital plane and positioning along the orbit to cover the surface target region. Thus, a set of LWS overflights for each HGV track are considered. The HGV is considered to be countered when the LWS is within 1000 km and the time window of the engagement is within one time step. When the pursuer successfully defends the ground target against the evader, the quality of success is rated by metric Q accounting for range, Q_R, time, Q_T, and geometry aspect, Q_G, with each value having an upper, $\mathcal{u}$, and lower, ℓ bound.

$$Q = Q_R Q_T Q_G \tag{2.1}$$

Q_T is the time during which the HGV is within the LOS of the LWS, while Q_G is the off nadir angle, θ. Q_R is the distance along the LOS between the HGV and LWS, characterized by R. To determine R first the relative inertial position vector, $\vec{R}$, is calculated by subtracting the inertial position vectors of the HGV, $\vec{R}_{HGV}$, and LWS, $\vec{R}_{LWS}$. The relationship between the HGV and LWS is represented schematically in the vector diagram shown in Figure 33.

$$\vec{R} = \vec{R}_{HGV} - \vec{R}_{LWS} \tag{2.2}$$

The inertial frame is represented by unit vectors Î, Ĵ, and K̂. R is then found by taking the square root of the components of $\vec{R}$.

$$\vec{R} = \mathrm{X}\hat{I} + Y\hat{J} + Z\hat{K} \tag{2.3}$$

$$R = \sqrt{(X^2 + Y^2 + Z^2)} \tag{2.4}$$

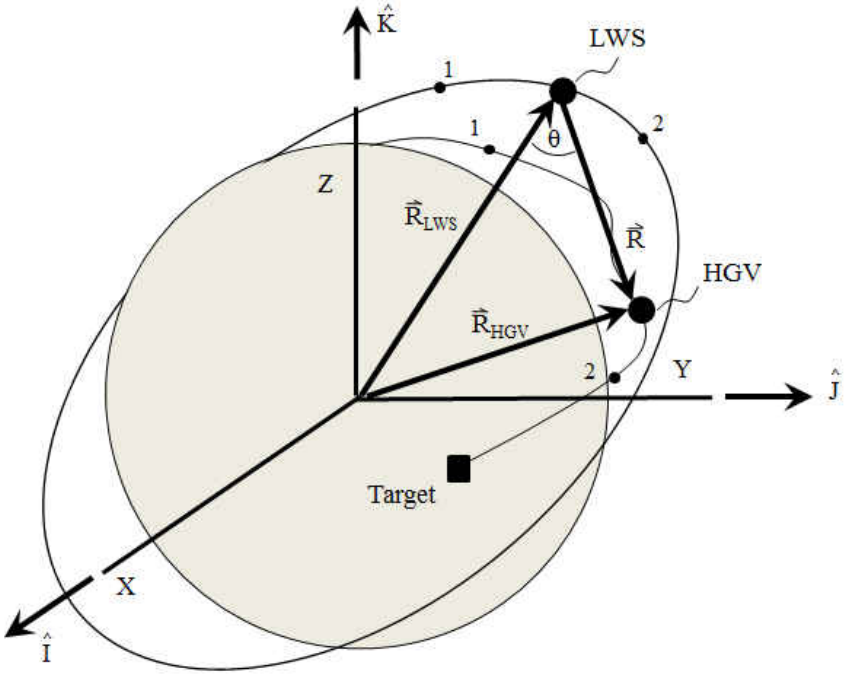

Figure 33 Vector Diagram for LWS and HGV

The u and ℓ values for Q_R Q_T, and Q_G are shown in Table 1, with the quality relationships shown in Figure 34.

Table 1 Upper and Lower Bounds for Quality Metrics

Quality Metric	ℓ	u
Q_R	30 km	1000 km
Q_T	60 s	300 s
Q_G	0°	90°

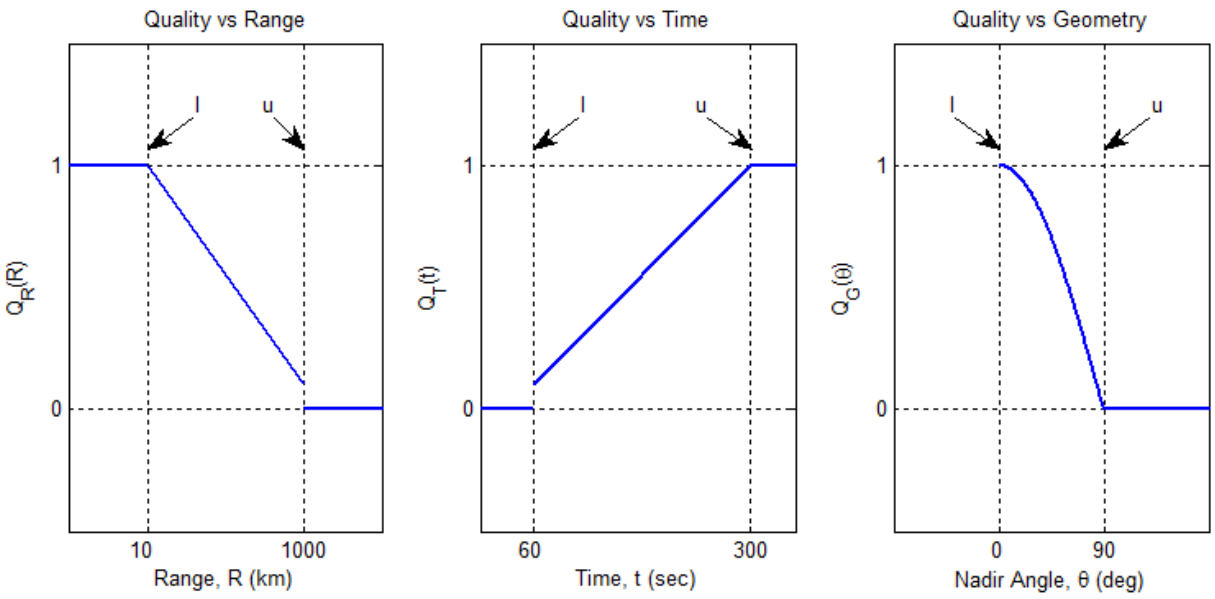

Figure 34 Quality Metrics Q_R, Q_T, and Q_G

2.3. Initial Conditions

HGV test flight data was not available for comparison during this research effort. Instead of using actual flight data, initial conditions developed by Nguyen in Reference [49] were used. Likewise, it is known that the SBL IFX and follow-on constellation were planned for low earth orbit (LEO), but specific orbital parameters were unavailable. The orbit of the International Space Station (ISS) was chosen as a substitute test study location for the SBL given NASA's success in constructing and maintaining a low earth orbit space station with the equivalent complexity that would be expected of an SBL.

Of the six classical orbital elements required to determine the orbit of the satellite, four are used for initial conditions, these include: semi-major axis, eccentricity, inclination, and argument of perigee. The initial values are: a = 6788586.18 m, e = 0.0004482, i = 51.6422°, and

ω = 208.80294°, which places the SBL in the approximate orbit of the International Space Station. The remaining two elements are set by the SBL parameter variation logic.

In calculating the trajectory for the HGV several parameters were defined as initial conditions including a lift to drag ratio, L/D, of 8.61. [49] An initial launch altitude, *h,* of 30 km was chosen, which is similar to the drop altitude exhibited by the B-52 for the test of the X-43 and X-51. An initial HGV launch velocity, V_L was set between Mach 2 and Mach 11.5 to simulate the speed exhibited by the X-43 and X-51. The launch velocity was normalized with respect to the orbital velocity of the HGV at the surface of the earth, V_s.

$$\bar{V}_L = \frac{V_L}{V_s} \tag{2.5}$$

V_s is the circular orbit velocity:

$$V_s = \sqrt{\frac{Gm_e}{r_e}}, \tag{2.6}$$

where G is the gravitational constant, m_e is the mass of the earth and r_e is the radius of the earth. The velocity of the HGV at ground level, $V_{g=r_e}$, was set to 0.3. Initial velocity imparted by the first stage booster is sufficient to insert the HGV along its ballistic skip trajectory. At the end of this segment the HGV follows the glide phase to the ground target. The atmospheric model is used for altitudes below 30 km with an isothermal scale height of the atmosphere, H, set at 6704 m based on the U.S. Standard Atmosphere 1976, with the glide calculations continuing from the ballistic calculations for the HGV. During the ballistic and glide phase the angle of attack, α,

and the non-dimensional in-flight velocity, $\bar{V}_f$ are varied according to the HGV parameter variation logic. The HGV reaches the target by taking the final point along the flight path and mapping it to the target longitude and latitude location.

NNS, located at latitude = 36.957638° and longitude = -76.329428° in Norfolk, VA, is the world's largest naval complex and has been selected as the ground target for the HGV which the LWS is to counter. Given the high concentration of high value targets including aircraft carriers, destroyers, cruisers, amphibious assault ships, and submarines, Norfolk is a key U.S. asset and potential target for HGVs. A time step of 60 s was used throughout all calculations with the simulation beginning at time 0 s. As the simulation progresses with the LWS and the HGV following their orbits and flight paths, respectively, the earth and ground target rotates. Vehicle and earth motions are propagated in the inertial frame, and data is transformed to the earth fixed frame, when needed.

2.4. Orbital Mechanics

To describe the astrodynamics of an artificial body such as a satellite or platform about a natural primary attracting body requires six classical orbital elements. These elements describe the size, shape, and orientation of the orbit, and the position of the satellite along the orbit. These six elements are defined below. [50]

1. Semi-Major Axis, *a*, specifies the size of the orbit and is one-half the distance across the long axis of an ellipse as seen in Figure 35.
2. Eccentricity, *e*, specifies the shape of an orbit by looking at the ratio of the distance between the two foci and the length of the major axis. See Figure 36.

3. Inclination, i, describes the orientation or tilt of the orbit relative to the equatorial plane.
4. Right Ascension of the Ascending Node, Ω, describes the orientation or swivel of the orbit relative to the vernal equinox, indicated by unit vector $\hat{I}$, and the point at which the orbit passes north of the equator on the equatorial plane.
5. Argument of Perigee, ω, describes the orientation of an orbit within its orbital plane. This element is the angle between the ascending node and perigee, measured in the direction of the spacecraft's motion.
6. True Anomaly, v, specifies the position of the satellite along its orbit as measured from perigee.

Figure 37 depicts inclination, right ascension, argument of perigee, and true anomaly in relation to the equatorial plane and the inertial frame represented by unit vectors $\hat{I}$, $\hat{J}$, and $\hat{K}$. Unit vector $\hat{I}$ points from the associated star to the planet at the instant when the equatorial plane of the planet passes through the star's center and the planetary northern hemisphere experiences increasing radiance from the star. Unit vector $\hat{J}$ lies in the equatorial plane pointing in the direction of the planetary orbital motion and unit vector $\hat{K}$ points along the planetary northern pole.

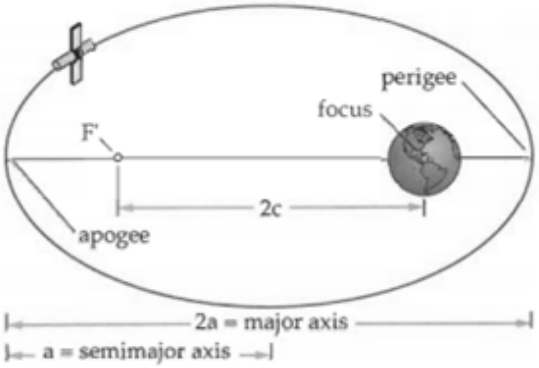

Figure 35 Semi-Major Axis [50]

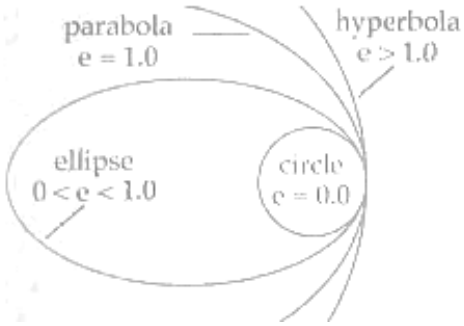

Figure 36 Eccentricity [50]

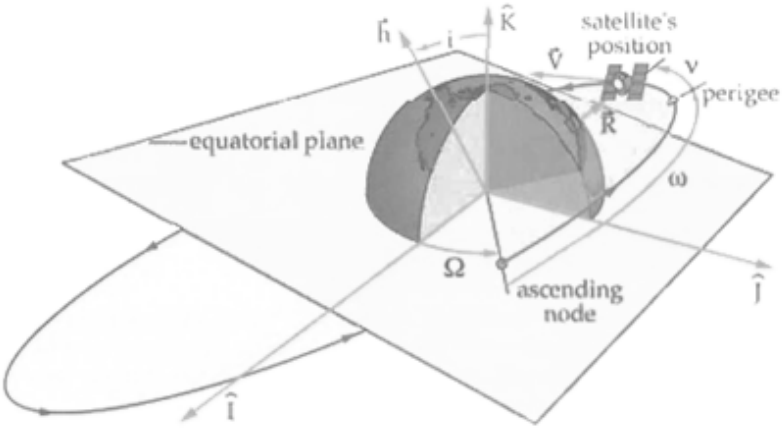

Figure 37 Classical Angular Orbital Elements [50]

Expressing the instantaneous geocentric equatorial position and velocity vectors of a satellite for engineering analysis and prediction in computer code, such as MATLAB, is often advantageous and even necessary. Figure 38 depicts the state vector for position R and velocity V with respect to unit vectors Î, Ĵ, K̂ and vernal equinox, ♈. The six rectangular position and velocity components of R and V form the six state variables that comprise the state vector, for which equations relating to the six classical orbital elements exist.

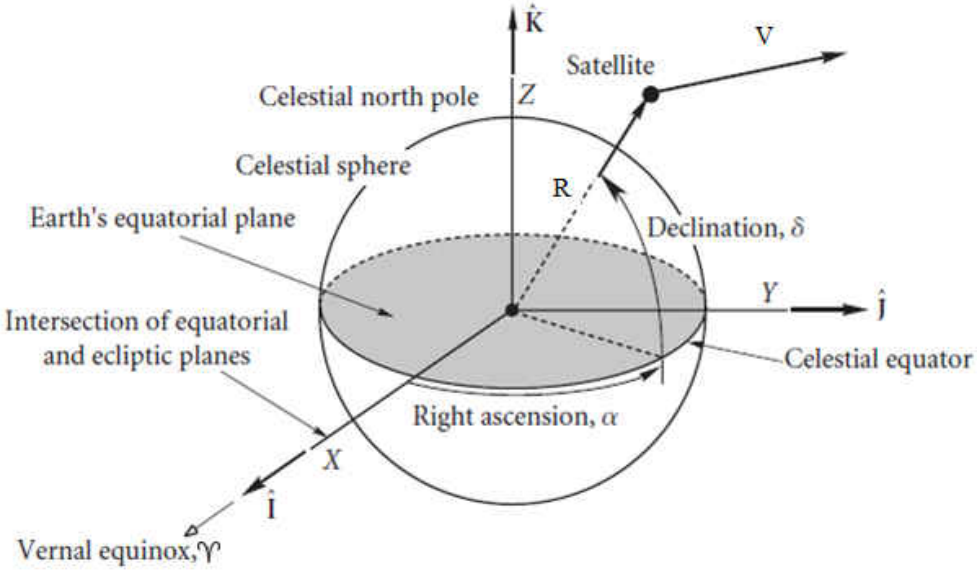

Figure 38 Orbital State Vectors [51]

2.5. Closed-Form Solution for LWS Orbit

The equations of motion of a satellite in orbit about another body have been well understood since the time of Newton and Kepler. Here the six classical orbital elements are used to develop the instantaneous position and velocity of the LWS in closed-form. Beginning with the semi-major axis and the earth gravitational constant, μ, the mean motion, n, period of orbit, T and final time, t_f for a specified number of orbits n_{orb} are given by.

$$n = \sqrt{\frac{\mu}{a^3}}$$

(2.7)

$$T = \frac{2\pi}{n}$$

(2.8)

$$t_f = T\, n_{orb}.$$

(2.9)

The mean anomaly, *M*, is determined by first calculating the initial eccentric anomaly, E_0, using the eccentricity, *e,* and the initial value for true anomaly, ν_0, and then taking the fractional period of an orbit that has elapsed since pericenter, t_p .[52]

$$E_0 = cos^{-1}\left(\frac{e + cos(\nu_0)}{1 + e\, cos(\nu_0)}\right)$$

(2.10)

$$t_p = \frac{-E_0 + e\, sin(E_0)}{n} + t_0$$

(2.11)

$$M = n(t - t_p)$$

(2.12)

Then true anomaly v at general time t can be determined from M by solving Kepler's equation.

The specific angular momentum, H, is found by first utilizing the semi-major axis and eccentricity to calculate the semi-latus rectum, p.

$$p = a(1 - e^2) \tag{2.13}$$

$$H = \sqrt{\frac{\mu}{p}} \tag{2.14}$$

For the specific angular momentum, true anomaly, and eccentricity, the earth centered inertial coordinates (ECI) for the LWS, can be determined in Cartesian space as follows:

$$R_{x,y,z} = \left(\frac{H^2}{\mu}\right)\left(\frac{1}{1 + e\cos v}\right)\begin{bmatrix}\cos v\\ \sin v\\ 0\end{bmatrix} \tag{2.15}$$

$$V_{x,y,z} = \left(\frac{\mu}{H}\right)\begin{bmatrix}-\sin v\\ e + \cos v\\ 0\end{bmatrix}. \tag{2.16}$$

Vector $R_{x,y,z}$ defines the path of the LWS around the earth and is referred to as the orbit equation.[51] Similarly, vector $V_{x,y,z}$ determines the orbit velocity equation. The product of the rotation matrices corresponding to the argument of perigee, inclination, and the right ascension of the ascending node is employed to generate the direction cosine matrix, Q_x. [51]

$$Q_x = \begin{bmatrix} cos\,\omega & sin\,\omega & 0 \\ -sin\,\omega & cos\,\omega & 0 \\ 0 & 0 & 1 \end{bmatrix} \times \begin{bmatrix} 1 & 0 & 0 \\ 0 & cos\,i & sin\,i \\ 0 & -sin\,i & cos\,i \end{bmatrix} \times \begin{bmatrix} cos\,\Omega & sin\,\Omega & 0 \\ -sin\,\Omega & cos\,\Omega & 0 \\ 0 & 0 & 1 \end{bmatrix}$$

(2.17)

Matrix Q_x implements transformation from the inertial frame to the perifocal or orbit frame. Geocentric equatorial position vector R is found by taking the inverse of the direction cosine matrix and multiplying it by the position orbit equation.

$$R = {Q_x}^{-1} R_{x,y,z}$$

(2.18)

Likewise, the geocentric equatorial velocity vector V is found by taking the inverse of the direction cosine and multiplying it by the velocity orbit equation.

$$V = {Q_x}^{-1} V_{\boldsymbol{x,y,z}}$$

(2.19)

To translate the given LWS position into latitude, L_{lat_LWS}, and longitude, L_{lon_LWS}, the following calculations are made.

$$L_{lat\_LWS} = \sin^{-1}(\sin i \sin u)$$

(2.20)

$$L_{lon\_LWS} = \tan^{-1}\left(\frac{\mathrm{P}_y}{r}\right) - \varpi_{earth}$$

(2.21)

where, r, is equal to

$$r = \frac{p}{1 + e\cos v}$$

(2.22)

and u is the argument of latitude found by summing the true anomaly and the argument of perigee, i.e.

$$u = v + \omega.$$

(2.23)

To graph the trajectory of the LWS the unit vector, *h*, is calculated to find the nodes' line, n.

$$h = \begin{bmatrix} h_x \\ h_y \\ h_z \end{bmatrix} = \begin{bmatrix} \sin i \sin \Omega \\ -\sin i \cos \Omega \\ \cos i \end{bmatrix}$$

(2.24)

$$n = \begin{bmatrix} n_x \\ n_y \\ n_z \end{bmatrix} = \begin{bmatrix} -\dfrac{h_y}{\left({h_x}^2 + {h_y}^2\right)^{\frac{1}{2}}} \\ \dfrac{h_x}{\left({h_x}^2 + {h_y}^2\right)^{\frac{1}{2}}} \\ 0 \end{bmatrix}$$

(2.25)

2.6. Numerical Solution for LWS Orbit

The numerical solution for the LWS orbit is calculated as a method of verifying the closed-form solution. The position and velocity vectors R and V are then propagated through an ordinary differential equations solver where the orbital state space vector, $\dot{S}$, is determined at each new time step and the position vector is multiplied by the new position magnitude, R_{mag}.

$$R_{mag} = |R| \tag{2.26}$$

$$\dot{S} = \begin{bmatrix} V \\ -\left(\frac{\mu}{R_{mag}^{\,3}}\right) R \end{bmatrix} = \begin{bmatrix} V_x \\ V_y \\ V_z \\ -\left(\frac{\mu}{R_{mag}^{\,3}}\right) R_x \\ -\left(\frac{\mu}{R_{mag}^{\,3}}\right) R_y \\ -\left(\frac{\mu}{R_{mag}^{\,3}}\right) R_z \end{bmatrix} \tag{2.27}$$

If perturbations were to be accounted for, they would be added to the last three terms of the orbital state space vector.

2.7. HGV Boost Phase Equations of Motion

The ballistic missile boost phase utilizes the same classical orbital elements as those of a satellite. The range of the ballistic missile boost phase is determined from the assumed semi-major axis and eccentricity. The semi-major axis is given in terms of the two launch conditions: the magnitude of the launch radius vector from center of the earth, r_L, and the ratio of velocity to circular orbital velocity at launch altitude, V_L.

$$a = \frac{r_L}{(2 - V_L)^2} \tag{2.28}$$

Additionally, the eccentricity, e, is given in terms of V_L, and the launch angle, θ_L. The relationship between the launch conditions and the orbit is represented in Figure 39.

$$e = \sqrt{1 - (2 - V_L)^2 {V_L}^2 \, cos^2(\theta_L)} \tag{2.29}$$

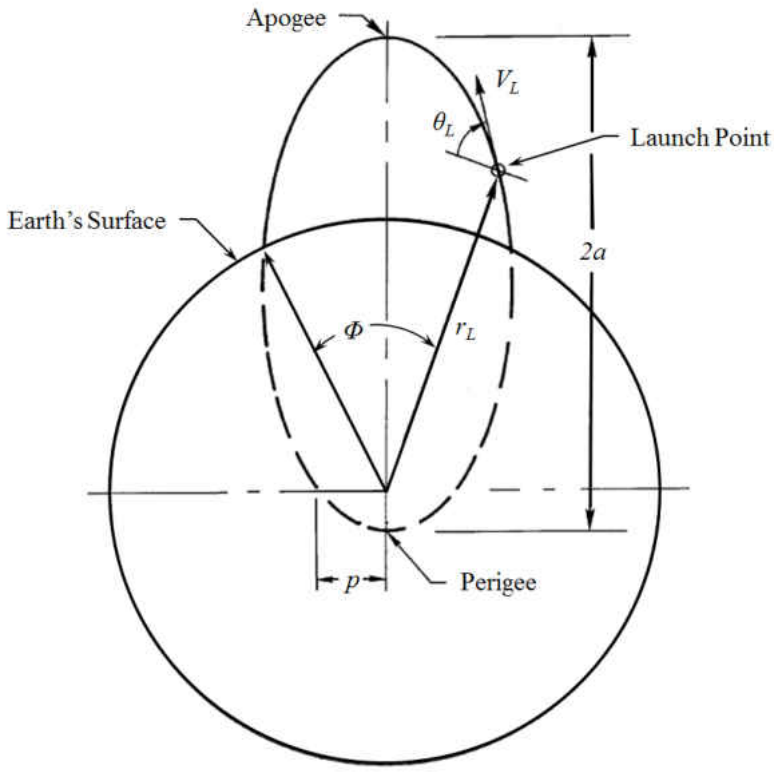

Figure 39 Ballistic Phase Launch Geometry [26]

The magnitude of the radius vector from center of the earth, r, is. [53]

$$r = \frac{a(1-e^2)}{(1+e\,cos(\theta-\theta'))} \tag{2.30}$$

By employing that radius, the velocity of the HGV in the ballistic phase can be calculated.

$$V = \sqrt{\mu\left(\frac{2}{r}-\frac{1}{a}\right)} \tag{2.31}$$

The total angular ballistic range, $\Phi_{ballistic}$, can be found by summing the number of ballistic skips, n, which is used in determining the skip coefficient, c_{skip}, which in turn is a function of the Lift to Drag Ratio, *L/D*.

$$c_{skip} = e^{\left(\frac{4(n-1)\theta_f}{L/D}\right)} \tag{2.32}$$

$$\phi_{ballistic} = \frac{R}{r_e} = 2\sum_{n=1}^{\infty} tan^{-1}\left(\frac{sin\,\theta_f\, cos\,\theta_f}{\frac{1}{V_f{}^2}c_{skip} - cos^2\,\theta_f}\right) \tag{2.33}$$

2.8. HGV Glide Phase Equations of Motion

The Glide Phase of the HGV is dependent on the atmospheric density. As discussed earlier, an approximation is made concerning the atmosphere in which it is assumed to be isothermal. The scale height, H, is the increase in altitude for which atmospheric pressure decreases by a factor of 1/e. Scale height is determined by taking the mean atmospheric temperature, T, universal gas constant, R, mean molecular mass of one atmospheric particle, M, and gravitational acceleration. The mean atmospheric temperature is the primary variable in determining the scale height; a value of 229.3K has been assumed for these equations.[27]

$$H = \frac{TR}{gM} \tag{2.34}$$

It is also necessary to find the range parameter for glide vehicles which is twice the partial range, $\Phi_{glide\_partial}$, divided by the lift to drag ratio.

$$J = \frac{2\phi_{glide\_partial}}{L/D} \tag{2.35}$$

The altitude is found by taking the velocity ratio of the HGV for the radius of the Earth, which for an altitude of 30 km is 0.3.

$$r = H\left(\ln\left(\frac{1-\left(1-{V_f}^2\right)e^J}{\left(1-{V_f}^2\right)e^J}\right)+\ln\left(\frac{1-{V_{r=r_0}}^2}{{V_{r=r_0}}^2}\right)\right) \tag{2.36}$$

The HGV glide range is finally calculated taking into account the final velocity ratio of the HGV as well as the lift to drag ratio.

$$\phi_{glide} = \frac{R}{r_e} = \frac{1}{2}\left(\frac{L}{D}\right)\ln\left(\frac{1}{1-{V_f}^2}\right) \tag{2.37}$$

The ballistic and glide components of altitude and range along the flight path are combined resulting in predicted r_{total} and ϕ_{total}.

CHAPTER 3

SIMULATION OVERVIEW

3.1. Program Layout

The program for the HGV-LWS simulation was developed within the Mathworks MATLAB R2013a computing environment[54] with the M_Map Toolbox [55] running on the Windows 7 operating system. The program's primary function is MAIN.m. This function retrieves four user-specified variable sets that manipulate the orbit of the LWS satellite and flight path of the HGV. These variables exist as a for-loop with minimum and maximum values and step size for each term (Table 2). The variables are then sent to LWS.m and HGV.m where the motion of the LWS and HGV are determined, respectively. Four other functions are called by the program; these are sub-functions of LWS.m and include the following: LWS_TIME.m, ECCENTRIC_ANOMALY.m [56], ORBIT_STATE.m [57], and ODE45.m [58]. Final determination of the quality of the engagement is determined by QUALITY_MEASURE.m, which is then sent back to MAIN.m for processing. Table 3 lists constants used by the program.

Table 2 Control Inputs for LWS and HGV

Control Input	Notation	Range	Increment
True Anomaly	ν	0 to 360 deg	10 deg
Right Ascension of Ascending Node	Ω	0 to 360 deg	10 deg
Velocity Ratio	V_f	0.1 to 0.5	0.1
Angle of Flight Path to Horizontal	θ_f	35 to 40 deg	0.5 deg

Table 3 Program Constants

Constant	Notation	Value
Radius of Earth	r_e	6378.1 km
Rotational Period of Earth	T_e	86164 s
Gravitational Constant	μ	3.986004415e5 km^3/s^2
Gravitational Acceleration	g	9.80665 m/s^2
Ground Target Latitude	T_{Lat}	36.957638 deg
Ground Target Longitude	T_{Long}	-76.329428 deg
Radius of Laser Acquisition	$r_{capture}$	1000 km

After the values for true anomaly and right ascension of ascending node are sent to LWS.m, the other four classical orbital elements are shown in Table 4. The period of the orbit is sent to LWS_TIME.m as an input to calculate the time vector and time span, which are sent back to LWS.m. The number of orbits and time step are constants listed in LWS_TIME.m and are shown in Table 5. Next, ECCENTRIC_ANOMALY.m is called using the mean anomaly and eccentricity as inputs. Finally, the ordinary differential equation (ODE) solver ODE45.m is called which integrates the orbit states found in ORBIT_STATE.m. The values for the time step, state, node line, and other calculated data are then sent back to MAIN.M

Table 4 Constants for LWS.m

Constant	Notation	Value
Semi-Major Axis	a	6788586.18 m
Eccentricity	e	.0004482
Inclination	i	51.6422 deg
Argument of Perigee	ω	208.80294 deg

Table 5 Constants for LWS_TIME.m

Constant	Notation	Value
Number of Orbits	n_{orb}	2
Time Step	*step*	60 s

The HGV input variables are velocity and attitude of attack which are sent to HGV.m with the following values listed in Table 6 as constants. After completing the calculations outlined in Chapter 3, HGV.m sends the HGV position and velocity data from the boost and glide phases to MAIN.m.

Table 6 Constants for HGV.m

Constant	Notation	Value
Launch Velocity	V_L	0.6
Launch Altitude	y_L	30 km
Lift to Drag Ratio	*L/D*	8.61
Velocity Ratio at Earth's Surface	V_r	0.3
Temperature of Atmosphere	*T*	229.3 K
Universal Gas Constant	*R*	8.315 J/mol*K
Molar Mass of Atmospheric Particle	*M*	0.029 kg/mol

MAIN.m receives the position and velocity information for the LWS and HGV for the inputs listed in Table 2. The program then calculates whether the HGV will reach the ground target first for a given set of inputs or the LWS will counter the HGV prior to the HGV reaching the ground target. A limit of two orbits is set for the satellite. The flight path, instantaneous position, and ground tracks are plotted for the LWS and HGV for each condition where the LWS

counters the HGV. These results are plotted on a rotating three-dimensional sphere of the earth with a geopolitical map overlaid on the sphere. This graphic is also presented in the two-dimensional projection manner (Figure 40). Figure 41 shows the overall computational tool flow chart and sequencing.

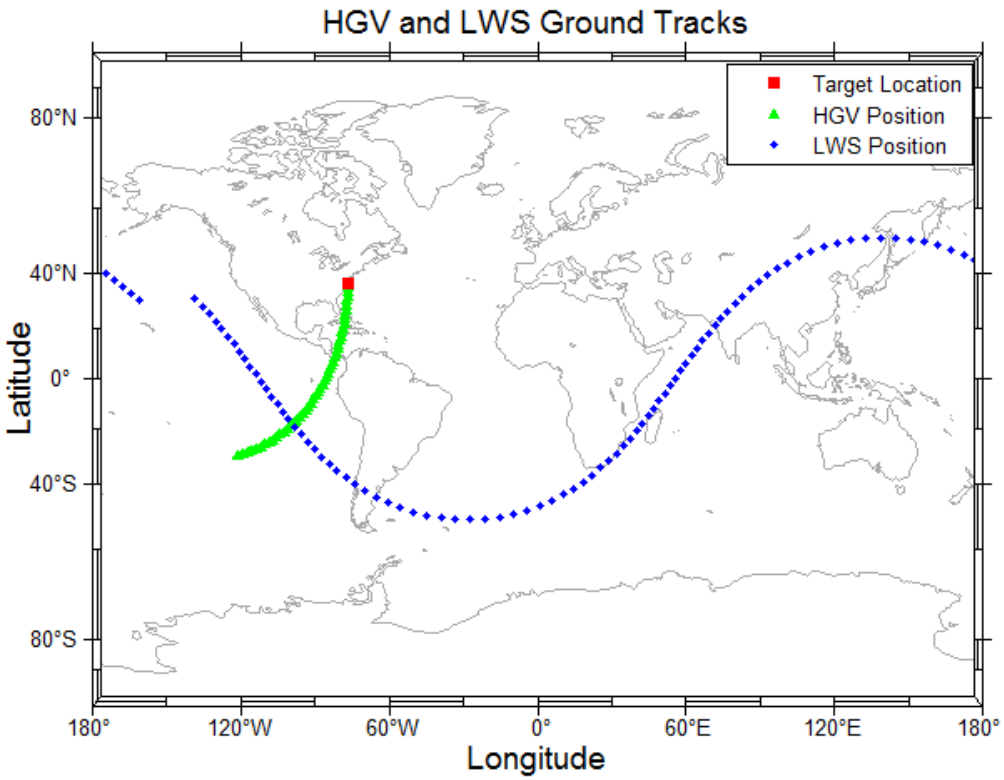

Figure 40 Flat Earth Map with HGV-LWS Data

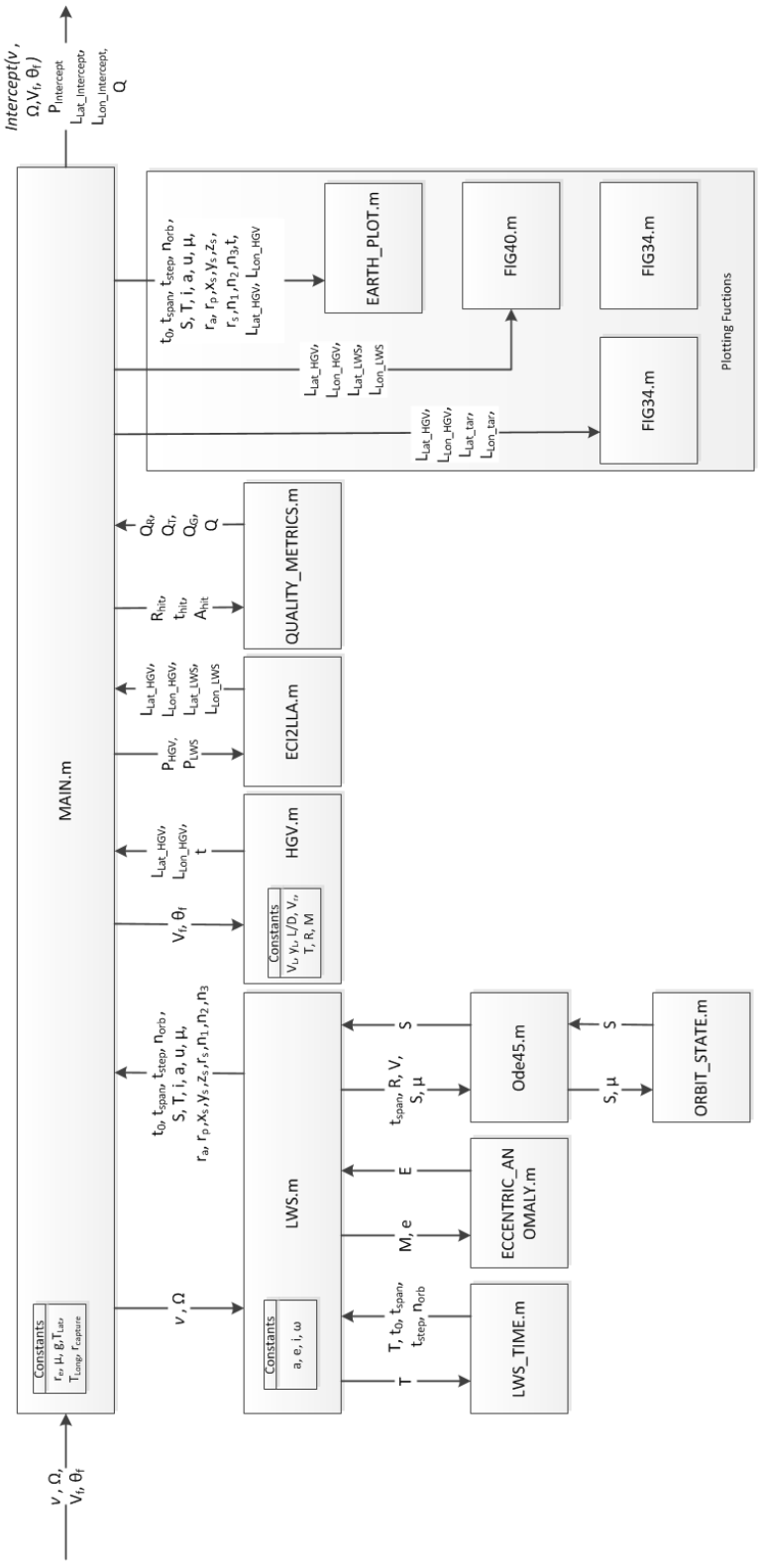

Figure 41 Program Flow Chart Layout

3.2. HGV Flight Path Determination

The initial flight path for the HGV is calculated assuming a flat earth. This flight path is mapped onto the spherical representation of the earth, setting the target's latitude and longitude as the end point for the flight path. The heading angle φ is initially set due East, with subsequent headings occurring every 45 degrees in a counterclockwise rotation, as seen in Figure 42, thus creating a set of flight paths about the target location.

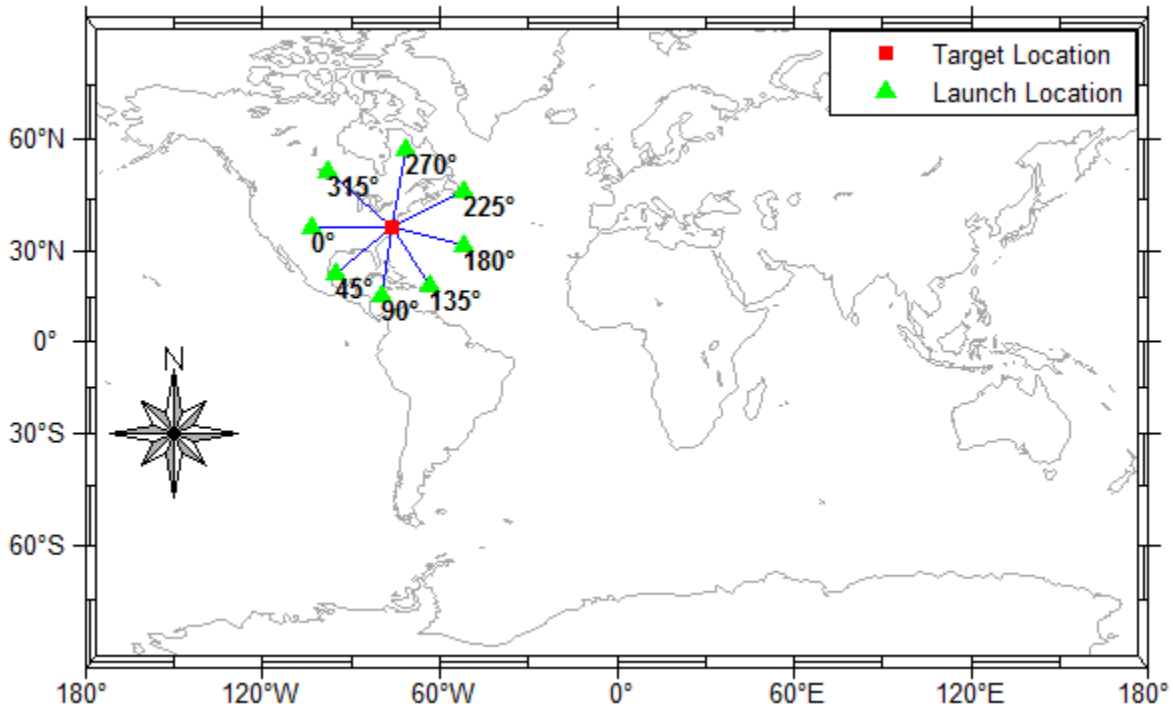

Figure 42 HGV Heading to Ground Target

To create the set of flight paths around the ground target, r_{total} and ϕ_{total} are converted into an earth center-earth fixed (ECEF) frame denoted by $P_{x\,HGV}$, $P_{y\,HGV}$, and $P_{z\,HGV}$ with r_e added to r_{total} giving the HGV distance from the center of the earth r_{HGV}.

$$P_{x\_HGV} = r_{HGV}\sin(L_{lat\_HGV})\cos(L_{lon\_HGV})$$
$$P_{y\_HGV} = r_{HGV}\sin(L_{lat\_HGV})\sin(L_{lon\_HGV})$$
$$P_{z\_HGV} = r_{HGV}\cos(L_{lat\_HGV})$$

(3.1)

ϕ_{total} is set as the longitude of the HGV, L_{lon_HGV}, with the latitude for the first flight path, L_{lat_HGV}, set to the target latitude, L_{lat_tar}.

$$P_{x\_HGV} = r_{HGV}\sin(L_{lat\_tar})\cos(\phi_{total})$$
$$P_{y\_HGV} = r_{HGV}\sin(L_{lat\_tar})\sin(\phi_{total})$$
$$P_{z\_HGV} = r_{HGV}\cos(L_{lat\_tar})$$

(3.2)

Similarly, the ground target location in the ECEF frame, P_{x_tar}, P_{y_tar}, and P_{z_tar}, is first converted from the modified polar coordinates in longitude, L_{lon_tar}, and latitude, L_{lat_tar}.

$$P_{x\_tar} = r_e\sin(L_{lat\_tar} - 90)\cos(L_{lon\_tar} - 180)$$
$$P_{y\_tar} = r_e\sin(L_{lat\_tar} - 90)\sin(L_{lon\_tar} - 180)$$
$$P_{z\_tar} = r_e\cos(L_{lat\_tar} - 90)$$

(3.3)

The x, y, and z components of the target position are normalized with respect to the target distance from the center of the earth, r_{tar} which for a land-based target and assuming a spherical earth can be approximated as r_e.

$$r_{tar} = \sqrt{{P_{x\_tar}}^2 + {P_{y\_tar}}^2 + {P_{z\_tar}}^2} \approx r_e$$

(3.4)

The following substitutions were made for each normalized polar component using α, β, and γ.

$$\alpha = \frac{P_{x\_tar}}{r_{tar}}$$

$$\beta = \frac{P_{y\_tar}}{r_{tar}}$$

$$\gamma = \frac{P_{z\_tar}}{r_{tar}}$$

(3.5)

Employing the normalized ECEF position components and heading angle, the rotation matrix, A_{Rot} can be determined.

$$A_{Rot} =$$

$$\begin{bmatrix} \cos\varphi + (1-\cos\varphi)\alpha^2 & \alpha\beta(1-\cos\varphi) - \gamma\sin\varphi & \alpha\gamma(1-\cos\varphi) + \beta\sin\varphi \\ \alpha\beta(1-\cos\varphi) + \gamma\sin\varphi & \cos\varphi + (1-\cos\varphi)\beta^2 & \beta\gamma(1-\cos\varphi) - \alpha\sin\varphi \\ \alpha\gamma(1-\cos\varphi) - \beta\sin\varphi & \beta\gamma(1-\cos\varphi) + \alpha\sin\varphi & \cos\varphi + (1-\cos\varphi)\gamma^2 \end{bmatrix}$$

(3.6)

The product of A_{Ro} and the HGV position vector generates the new position vector in terms of the earth centered inertial (ECI) frame, P_{HGV_ECI}, as it relates to φ.

$$P_{HGV\_ECI} = A_{Rot} \begin{bmatrix} P_{x\_HGV} \\ P_{y\_HGV} \\ P_{z\_HGV} \end{bmatrix} \tag{3.7}$$

3.3. Ground Track Propagation

During the motion of the LWS and HGV, ground tracks like Figure 43 were generated across the surface of the spherical representation of the earth. The ground track is plotted at every time step as the earth rotates. Taking the latitude and longitude position of the LWS, L_{lat_LWS} and L_{lon_LWS}, or HGV, L_{lat_LWS} and L_{lon_LWS}, and multiplying it by the radius of the earth results in an earth center fixed reference position for the ground track of either the LWS or HGV denoted by $P_{x\_gt\_LWS}$, $P_{y\_gt\_LWS}$, $P_{z\_gt\_LWS}$ and $P_{x\_gt\_HGV}$, $P_{y\_gt\_HGV}$, $P_{z\_gt\_HGV}$, respectively.

$$\begin{aligned} P_{x\_gt\_LWS} &= r_e \cos L_{lat\_LWS} \cos L_{lon\_LWS} \\ P_{y\_gt\_LWS} &= r_e \cos L_{lat\_LWS} \sin L_{lon\_LWS} \\ P_{z\_gt\_LWS} &= r_e \sin L_{lat\_LWS} \end{aligned} \tag{3.8}$$

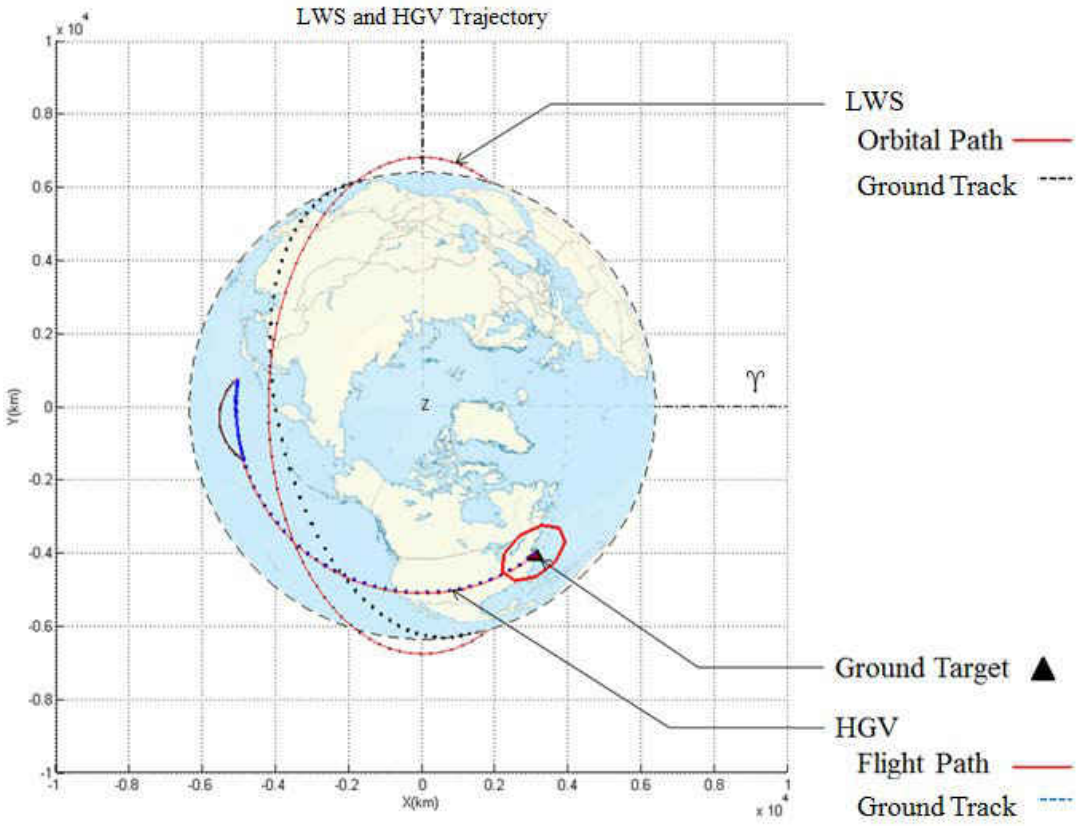

Figure 43 Ground Track Representation

CHAPTER 4

CASE STUDY RESULTS

4.1. Analysis Results

For the case of a satellite-based LWS countering an HGV in the protection of a ground target located at Norfolk Naval Station, a total of 100,185,210 case studies were run. Of the total number of cases run in which the LWS true anomaly and right ascension were varied along with the HGV velocity ratio, angle, and heading, a total of 487,414 case studies resulted in the LWS successfully intercepting the HGV, or 0.49% of the total cases. To better understand the results of the intercepts, the number of intercepts were compared against the HGV velocity ratio. This comparison is shown in Figure 44 from which it can be seen that the number of intercepts is generally decreasing as the velocity ratio of the HGV increases. There is, however, an increase in intercepts from the south at a velocity ratio of 0.5 which is detailed in the southern heading of the HGV, shown in Figure 45.

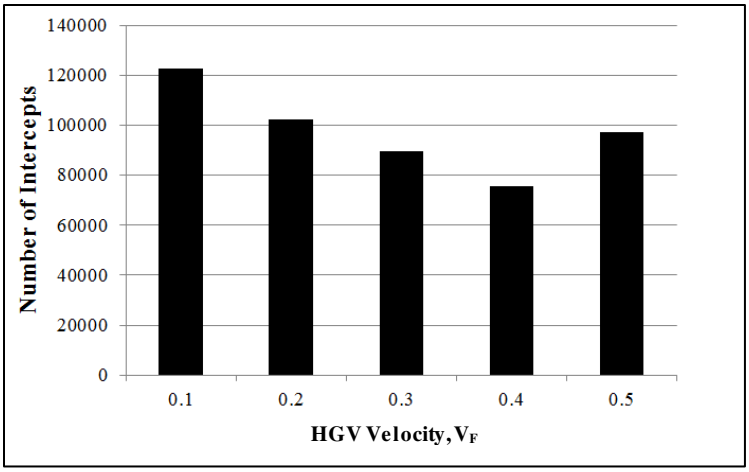

Figure 44 Successful Intercepts

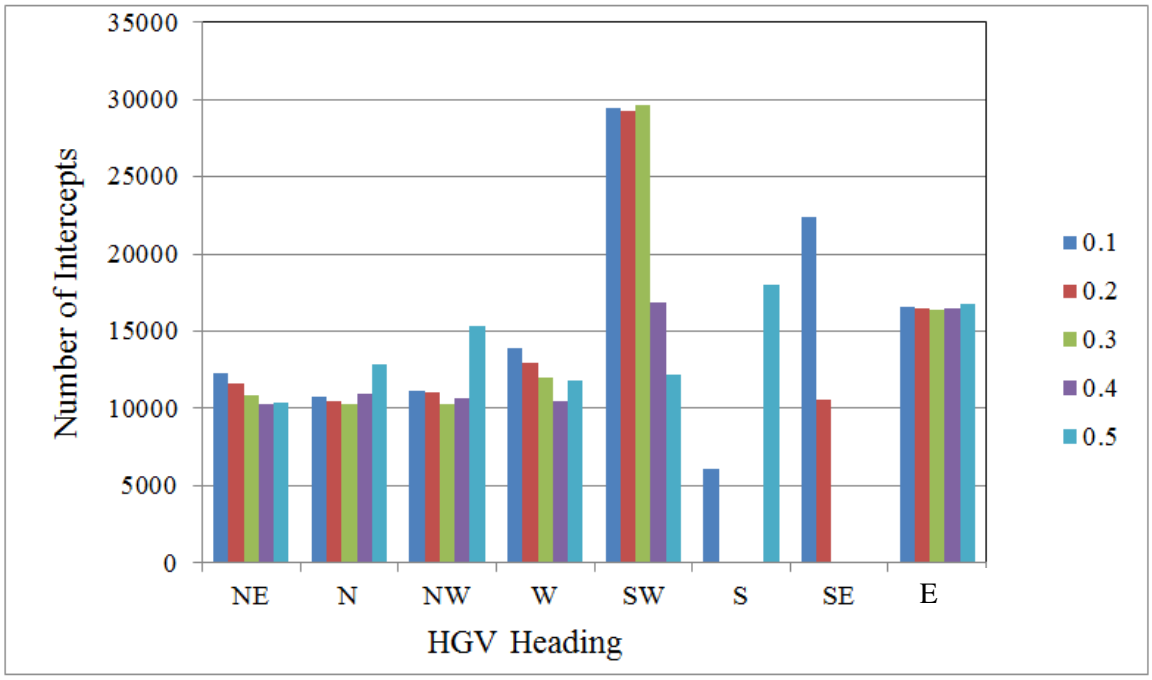

Figure 45 Intercepts with respect to HGV Heading and Velocity Ratio

In order to further examine the intercepts, the position of the LWS at time of intercept as well as the flight path of the HGV are plotted for varying velocity ratios in Figure 46 through Figure 50. These figures show that as the velocity ratio increased the distance from the ground target increased representing a longer time of flight. The position of the LWS at the time of intercept

remained clustered around the ballistic skip phase portion of the HGV flight path regardless of HGV velocity. This finding mirrors expected results for a conventional anti-ballistic missile in that the ballistic phase is the most vulnerable phase of the flight path for the missile due to the proximity to the passing LWS.

With a velocity ratio of 0.1 to 0.2, the HGV can be launched from the Caribbean Sea and the Atlantic Ocean west of Bermuda, as shown in Figure 46 and Figure 47, and reach the target. At a velocity ratio of 0.3 and 0.4, the HGV can be launched from the Eastern Atlantic Ocean, the Pacific Ocean east of Hawaii, and South America, as shown in Figure 48 and Figure 49, and reach the target. At a velocity ratio of 0.5, Figure 50 shows the HGV can be launched from the Pacific Ocean west of Hawaii, central Russia, and the southern Atlantic Ocean and reach the target.

Figure 46 displays eight ground tracks for the HGV at the eight corresponding headings; this is not the case with Figure 47 through Figure 50 where the ground tracks are only depicted when an intercept was predicted. Figure 46 through Figure 50 indicate no intercepts occur above a latitude of 51.81° which corresponds to the limits of the LWS orbit, namely the inclination as well as the upper limit of the range quality. Increasing either the upper limit for range quality or increasing the orbital inclination will allow the LWS to capture the full range of HGV latitude positions for this scenario of target position, HGV velocity ratio, flight angle and heading.

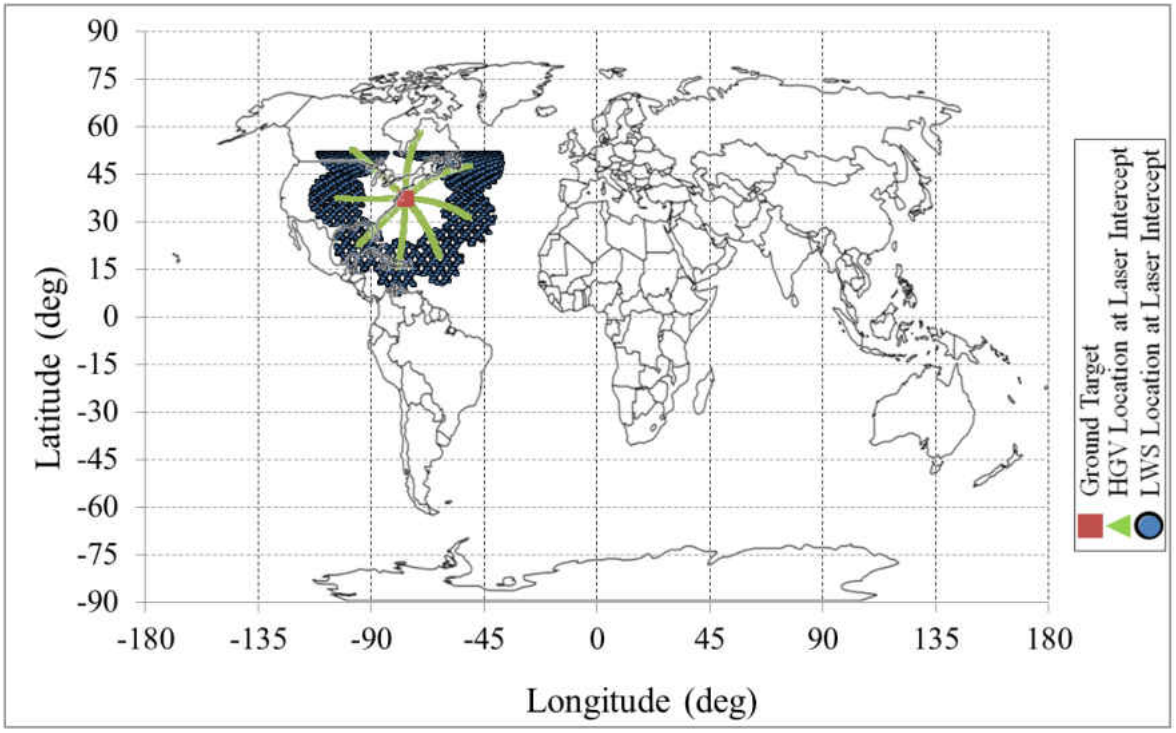

Figure 46 Intercepts for Vf = 0.1

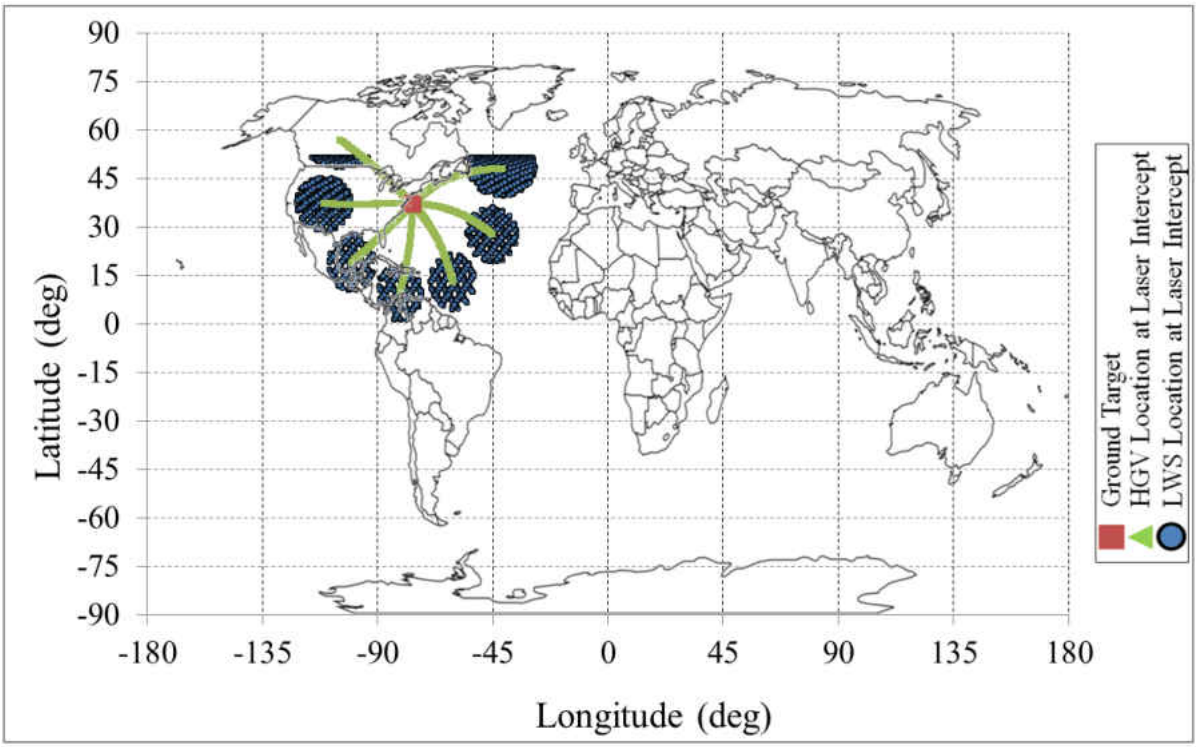

Figure 47 Intercepts for Vf = 0.2

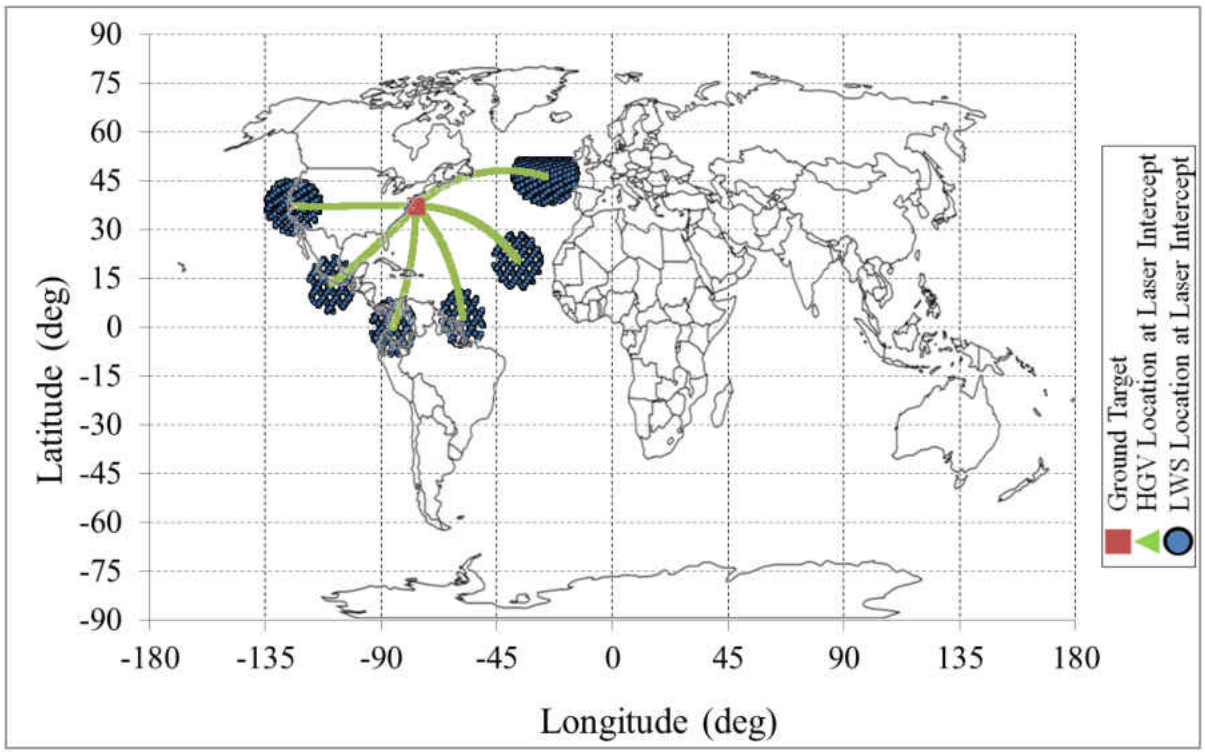

Figure 48 Intercepts for Vf = 0.3

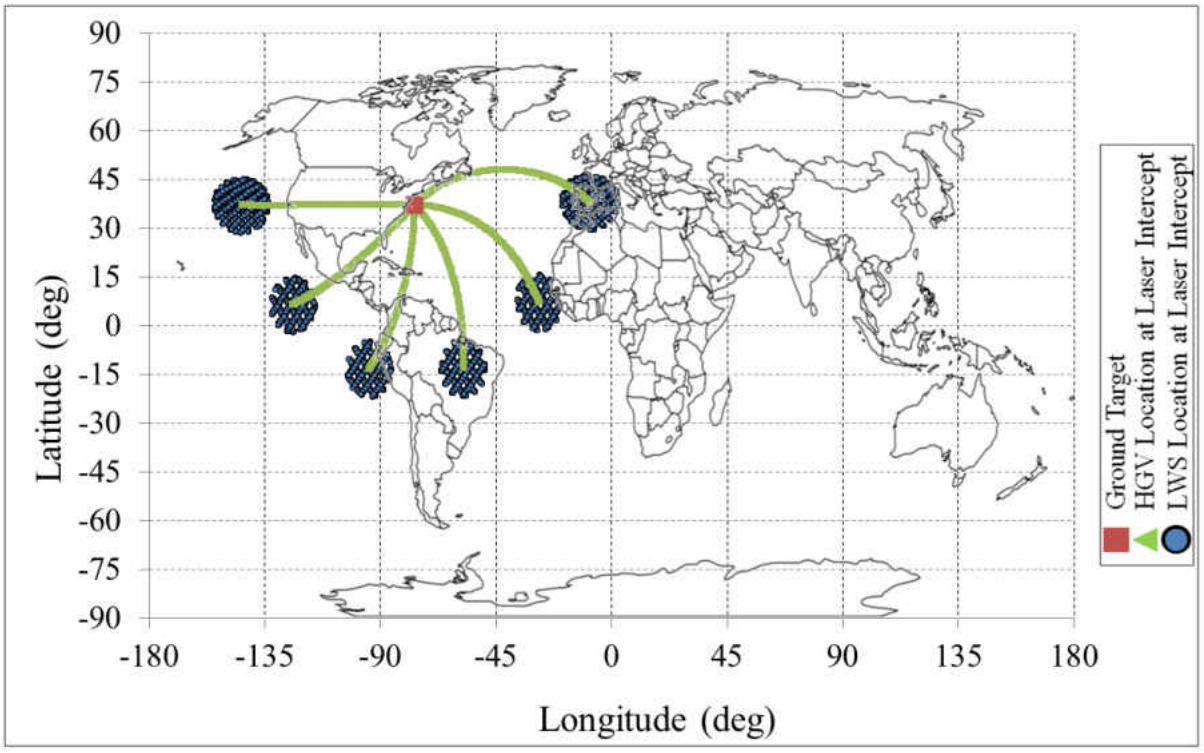

Figure 49 Intercepts for Vf = 0.4

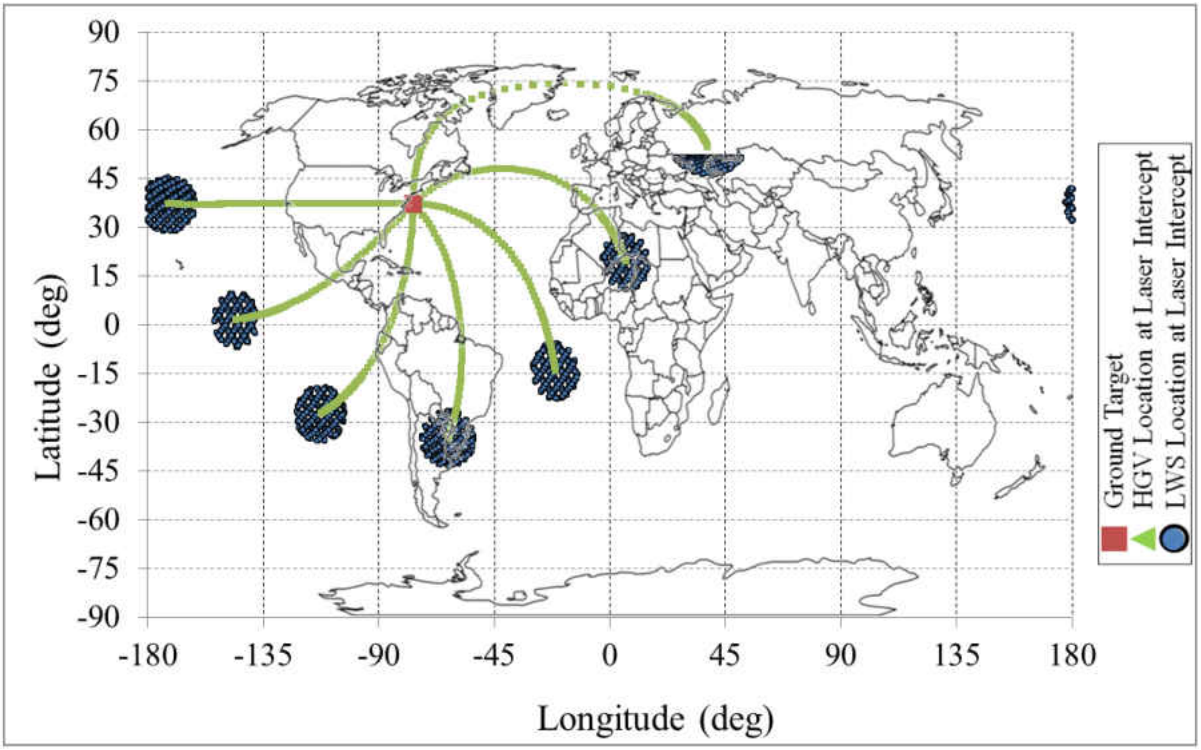

Figure 50 Intercepts for Vf = 0.5

4.2. Individual Case Study

By isolating selected input variables, additional insight is gained. By narrowing the data set down to HGV velocity ratio for 0.1 and the LWS right ascension of the ascending node between 205° and 290°, varying by 5°, the LWS intercepts can be overlaid onto the LWS ground tracks as shown in Figure 51. Shifting the LWS right ascension of the ascending node by 90° and truncating some ground tracks for visual clarity yields Figure 52, which when combined give the data set shown in Figure 46.

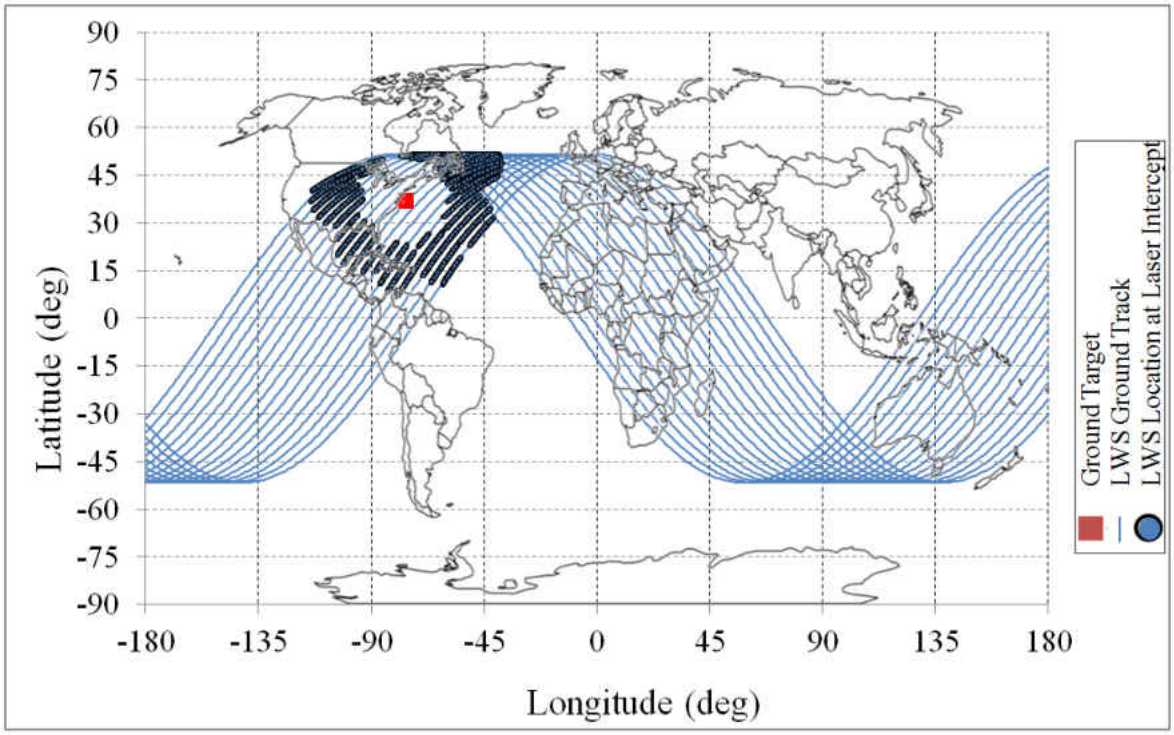

Figure 51 Intercept for Vf = 0.1 and Ω between 205° and 290° with LWS Ground Tracks

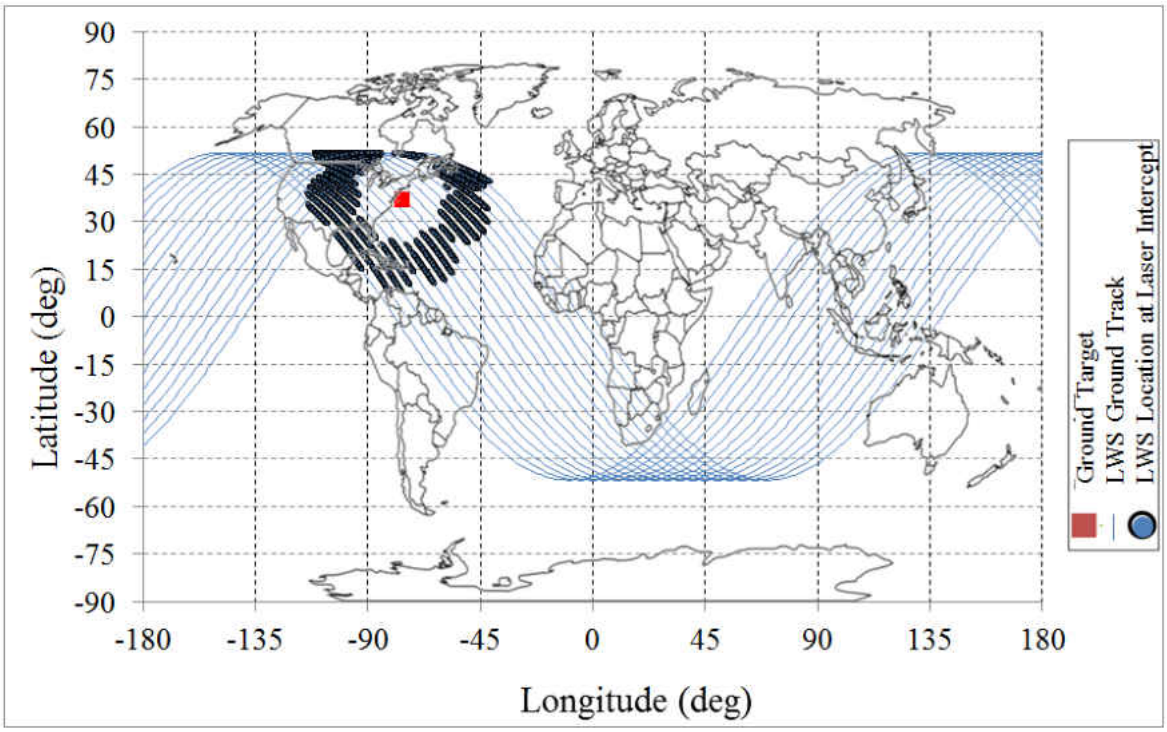

Figure 52 Intercepts for Vf = 0.1 and Ω between 100° and 185° with LWS Ground Tracks

The data set of intercepts for an HGV velocity ratio of 0.1 is further refined by examining only those intercepts that occurred when the HGV had a north heading and an HGV angle of 35°. This narrow range of data has been categorized subsequently in terms of intercept time duration. Figure 53 shows that as the LWS moves east in its orbit it acquires the HGV. The LWS continues at 60 second increments, per the time step, acquiring the HGV until it is out of range. The longest duration intercept that any orbit of the LWS was able to maintain was 5 minutes.

Examining one such intercept orbit of the LWS where the intercept duration was 5 minutes yields further insight. In Figure 54 the intercepts occurred when the LWS had orbit parameters of v = 150° and Ω = 270° and the HGV had flight path parameters of Vf = 0.1 and θf = 35°. Additionally, the location of the HGV for each intercepting time step is shown as the LWS heads northeast. The shortest approach occurred during the second time step at 180 seconds with a range of 392 km. As indicated in Table 7, this location also corresponded with the narrowest angle of 1.4° compared with approximately 7.9° at the start and finish of the intercept.

Applying the quality metrics outlined in Table 1 and Figure 34, the quality factors for range, time, angle and total quality are summarized in Table 8. From these quality metrics it can be seen that the maximum Total Quality measure occurs at 180 seconds and 240 seconds with the Quality then decreasing at 300 seconds. Normally, the intercept with the longest time would be expected to have the greatest quality, but as the range between HGV and LWS increased, the Total Quality was lowered. The effect that range, time, and angle have on the total quality can be seen in Figure 55 in which it is readily apparent that range plays the greatest role in reducing the total quality of the intercept.

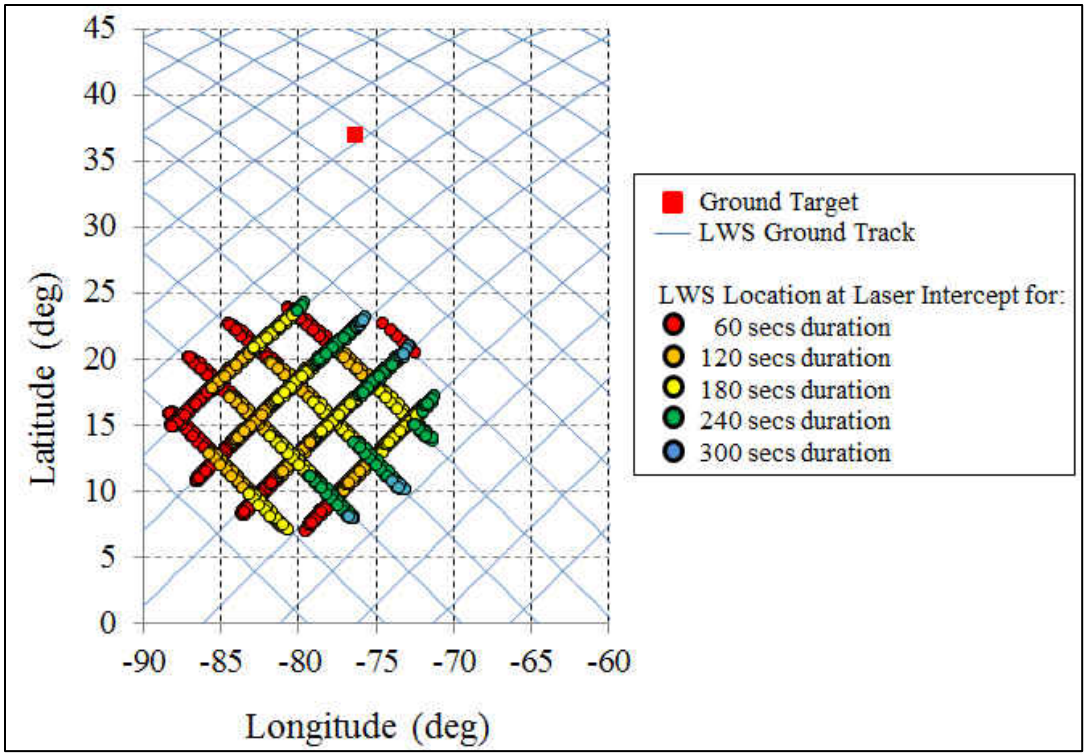

Figure 53 Intercepts for Vf = 0.1 and HGV Heading North, with LWS Ground Tracks

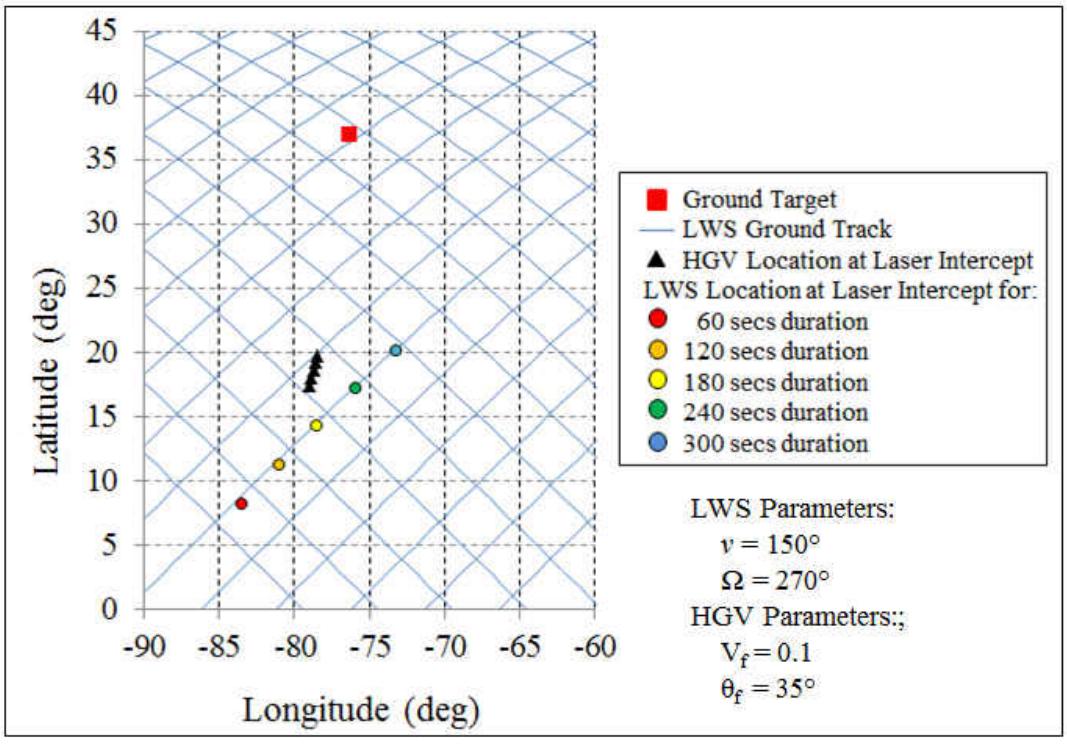

Figure 54 Intercepts for Single LWS Orbit

Table 7 Intercept Data for Single LWS Orbit

Time (sec)	Range (km)	Angle (deg)	LWS_LAT (deg)	LWS_LON (deg)	HGV_LAT (deg)	HGV_LON (deg)
60	970.7	7.82	8.2162	-83.497	17.4404	-79.008
120	591.2	4.08	11.2471	-81.025	18.034	-78.862
180	392.0	1.40	14.2569	-78.501	18.6287	-78.72
240	596.5	4.15	17.2391	-75.909	19.2244	-78.582

Table 8 Quality Metrics for Single LWS Orbit

Time (sec)	Range (km)	Angle (deg)	Q_R	Q_T	Q_G	Q
60	970.7	7.82	0.13	0.10	0.99	0.01
120	591.2	4.08	0.47	0.33	1.00	0.15
180	392.0	1.40	0.65	0.55	1.00	0.36
240	596.5	4.15	0.47	0.78	1.00	0.36
300	977.4	7.90	0.12	1.00	0.99	0.12

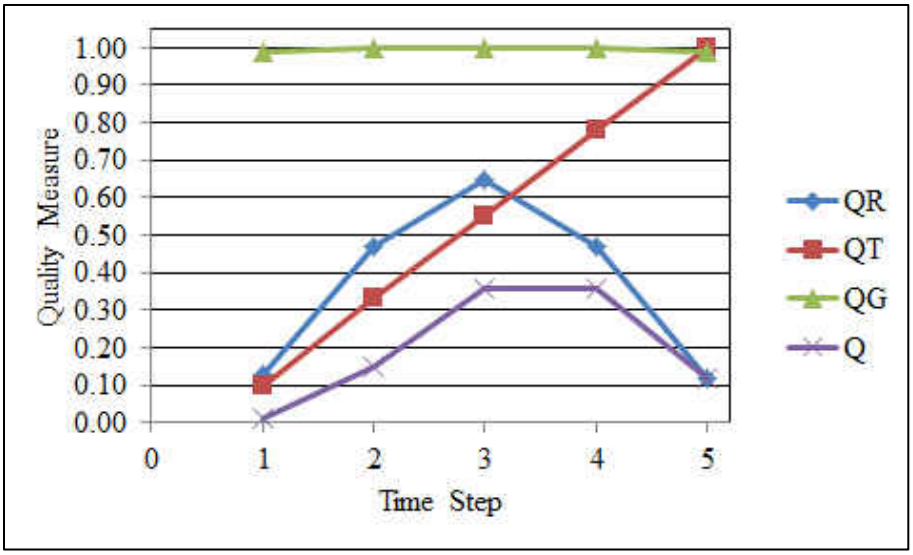

Figure 55 Quality Metrics for Single LWS Orbit vs. Time Step

4.3. Quality Metrics

Examining the quality metrics across all 487,414 intercepts resulted in interesting insights as well. Figure 56 shows that the occurrence of intercepts for a given range quality and for the five HGV velocity ratios are generally decreasing as the velocity ratio increased and as the range quality increased. This is similarly true for occurrence with respect to time quality shown in Figure 57. Again, it is apparent that a slight uptick in occurrence is noticed for a velocity ratio of 0.5 which is a factor of the HGV and LWS variables. The nadir angle was found to be near 0 degrees for most cases resulting in a geometry ratio of near 1.0 as seen in Figure 58. This bias is due to a combination of the time step, the mesh size for the LWS right ascension of the ascending node and the upper limit on the range quality. Combining the simultaneous influences of range, time and geometry on the simulation data set yields the total quality metrics for all intercept cases, as shown in Figure 59. For all intercepts, 31% have a total quality score of 0.05 which can be seen by the large spike in intercepts on the left of the graph. These are attributed to single time step intercepts with near maximum allowable ranges between the LWS and HGV. The second grouping of data has a total quality score between 0.06 and 0.25 which is attributed to 60 to 180 seconds of intercept and a medium to long range between the HGV and LWS. The most favorable grouping of data exists between a total quality of 0.26 and 0.45 accounting for 19% of all intercepts.

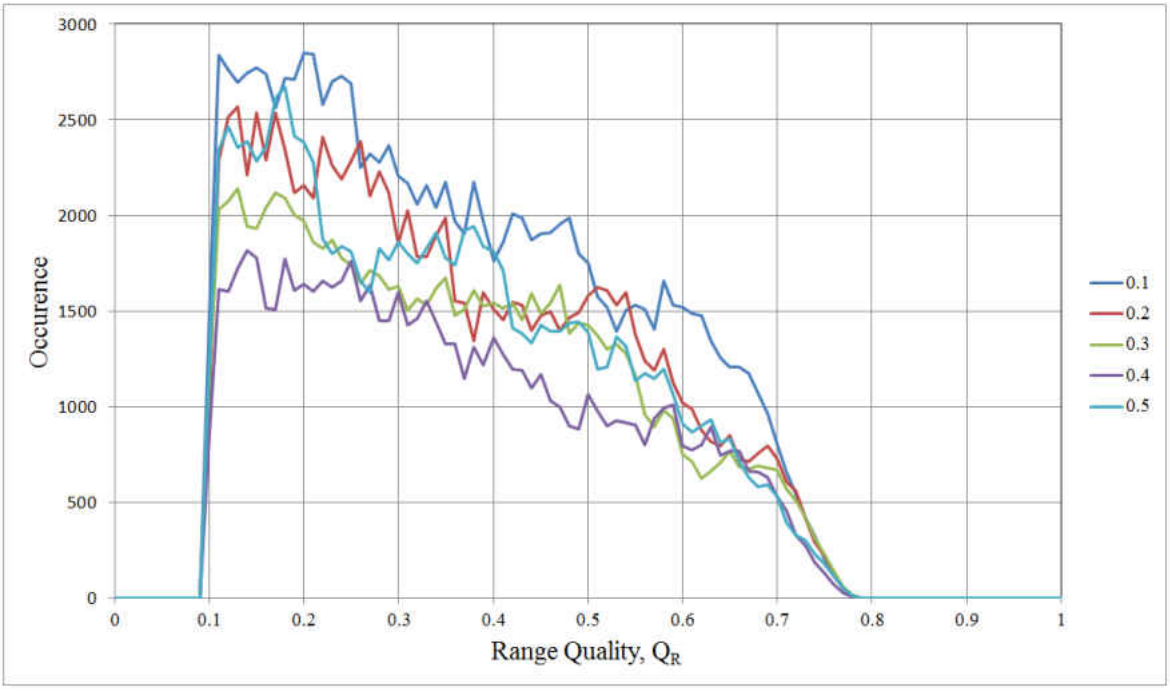

Figure 56 Intercept Occurrence vs. Range Quality

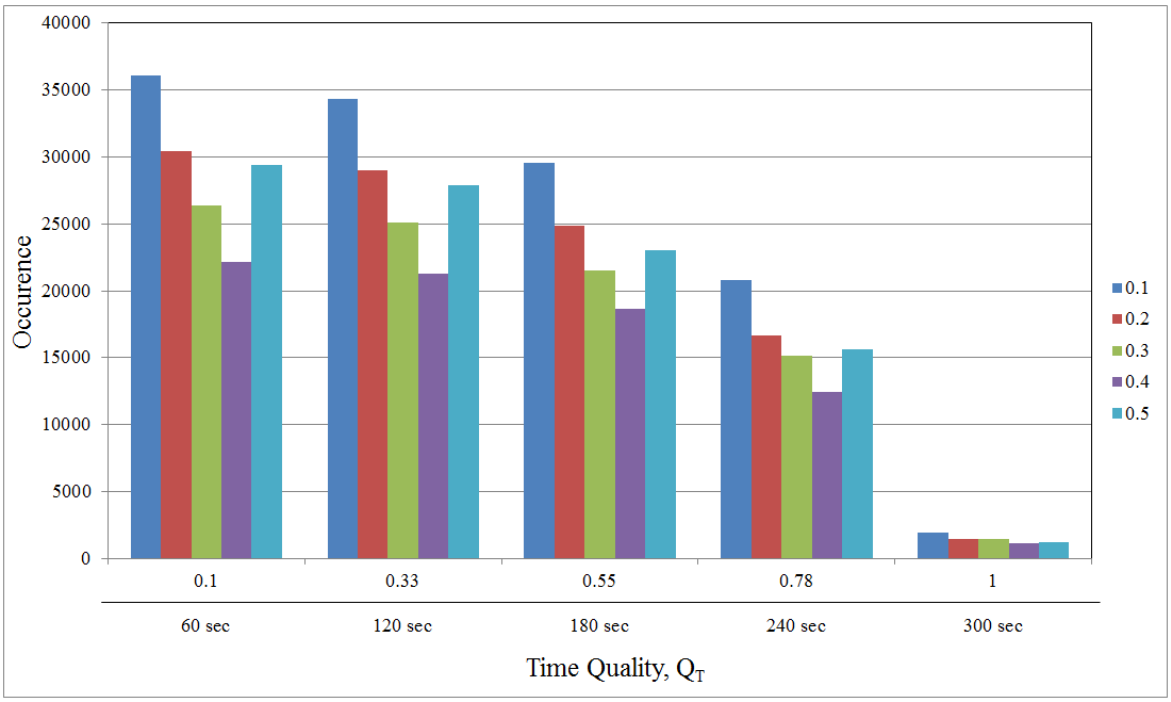

Figure 57 Intercept Occurrence vs. Time Quality

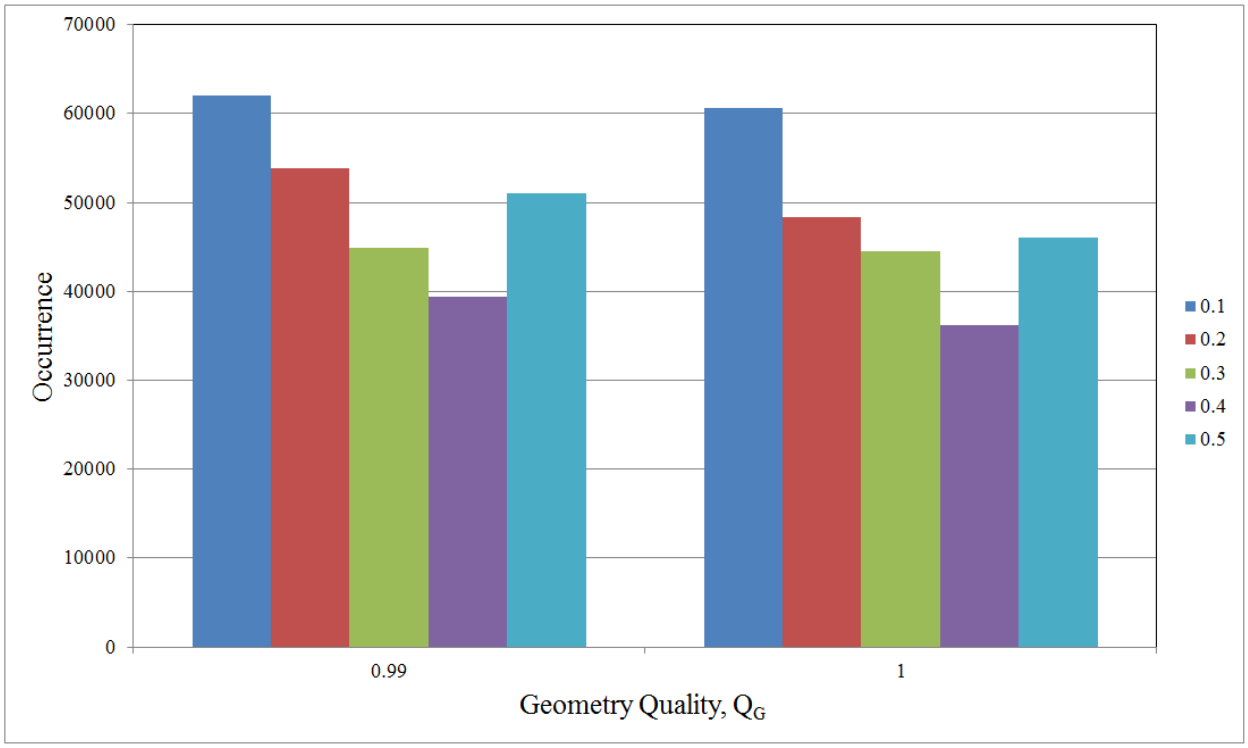

Figure 58 Intercept Occurrence vs. Geometry Quality

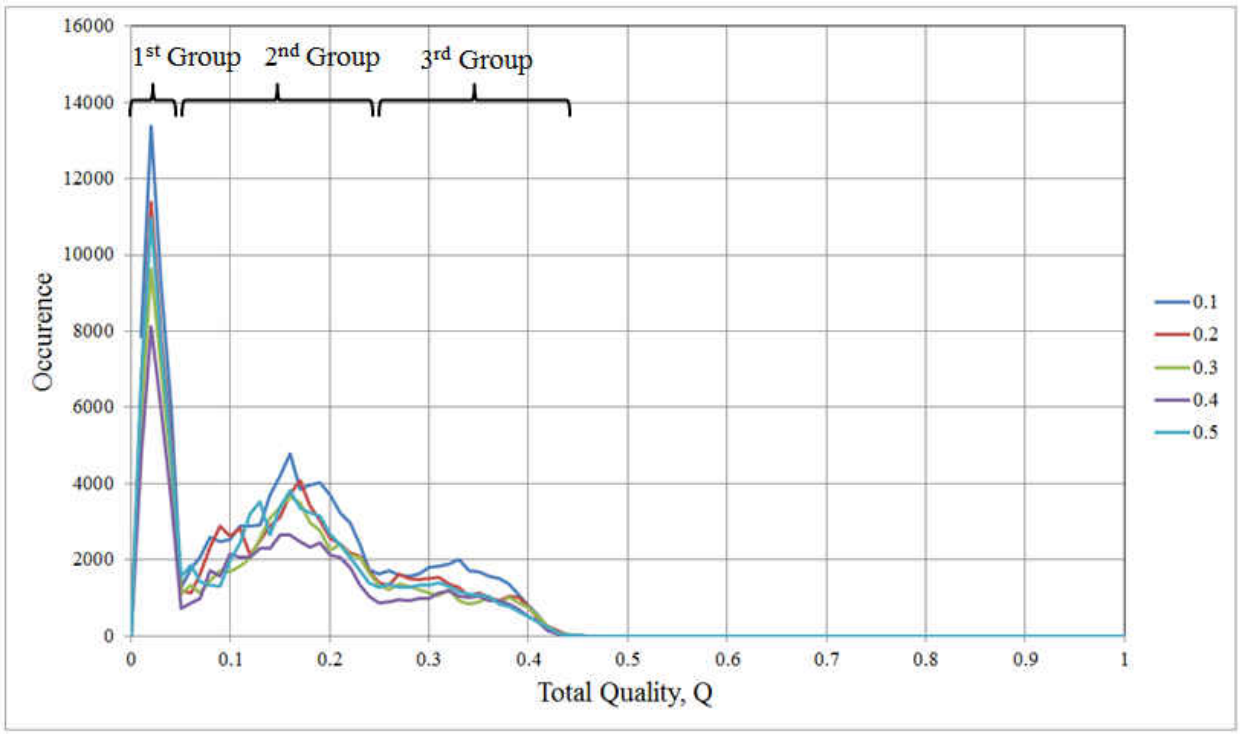

Figure 59 Intercept Occurrence vs. Total Quality

The trends and findings discussed thus far become readily apparent when the right ascension of the ascending node is compared with the total quality for multiple headings and varying velocity ratios as shown in Figure 60 through Figure 64. As the velocity increases, the grouping of data for various headings disperses from a tight grouping shown in Figure 60 to a separated grouping shown in Figure 64. This dispersal was also apparent in Figure 46 through Figure 50. The double grouping for heading 5 which aligns with a southwest trajectory also aligns with the increases in the number of cases shown in Figure 45. The apparent missing points that occur at total quality values of 0.05 align with the drop in occurrences in Figure 59 between the first and second groupings as described earlier.

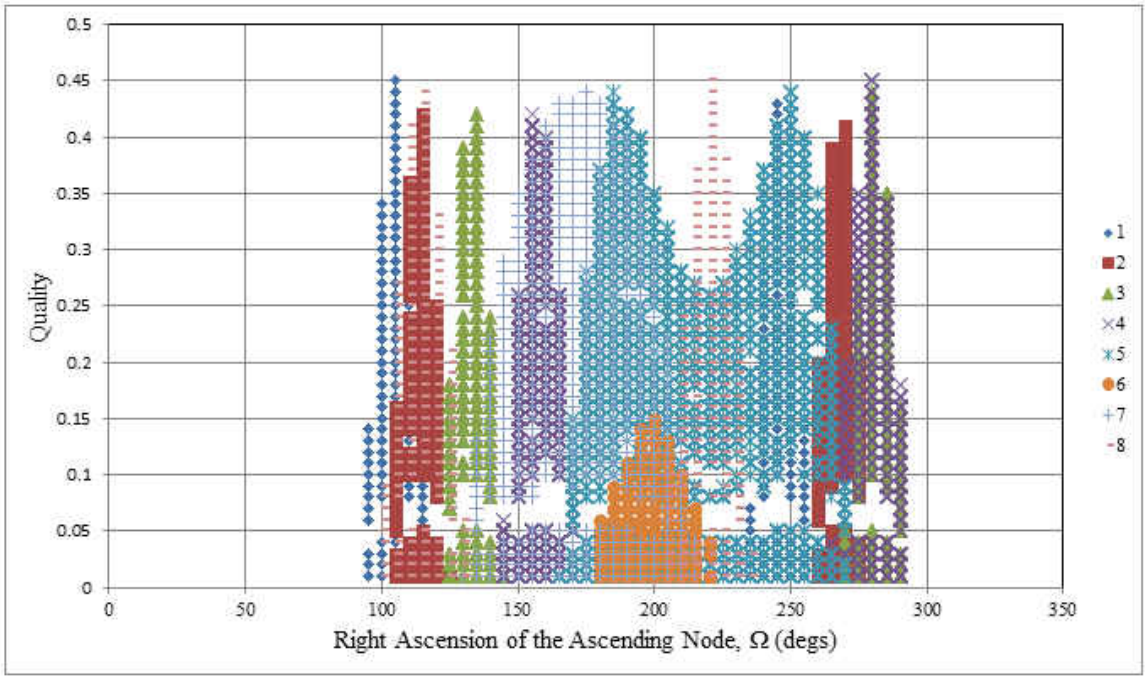

Figure 60 Right Ascension of Ascending Node vs. Total Quality for Multiple Headings at Vf=0.1

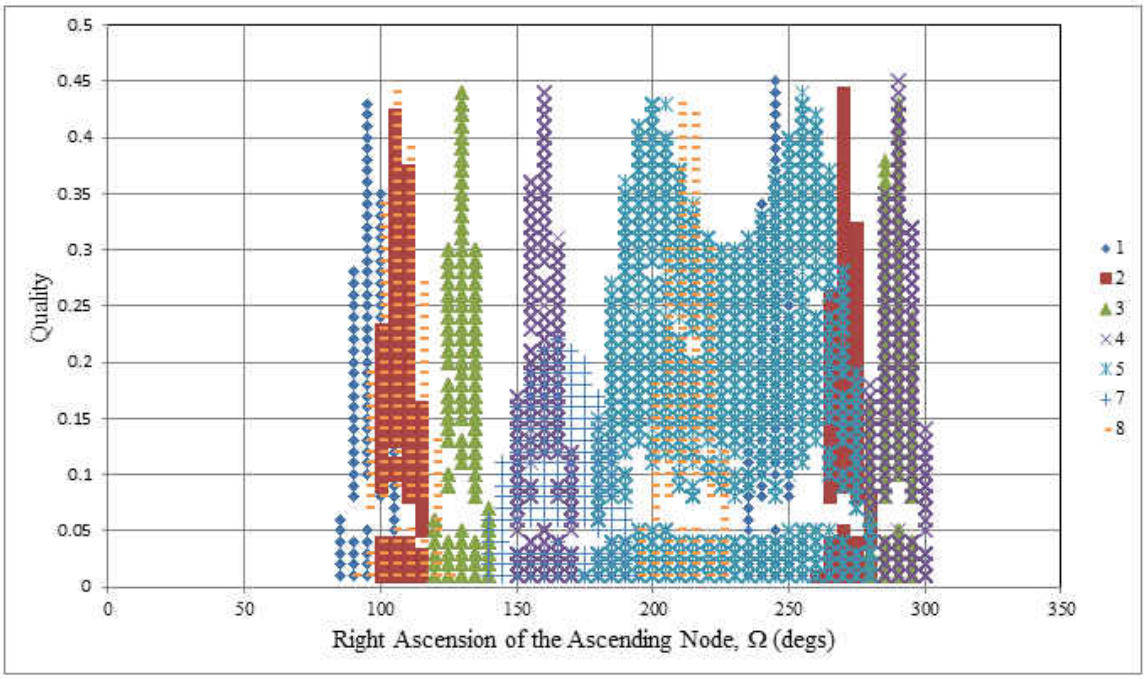

Figure 61 Right Ascension of Ascending Node vs. Total Quality for Multiple Headings at Vf=0.2

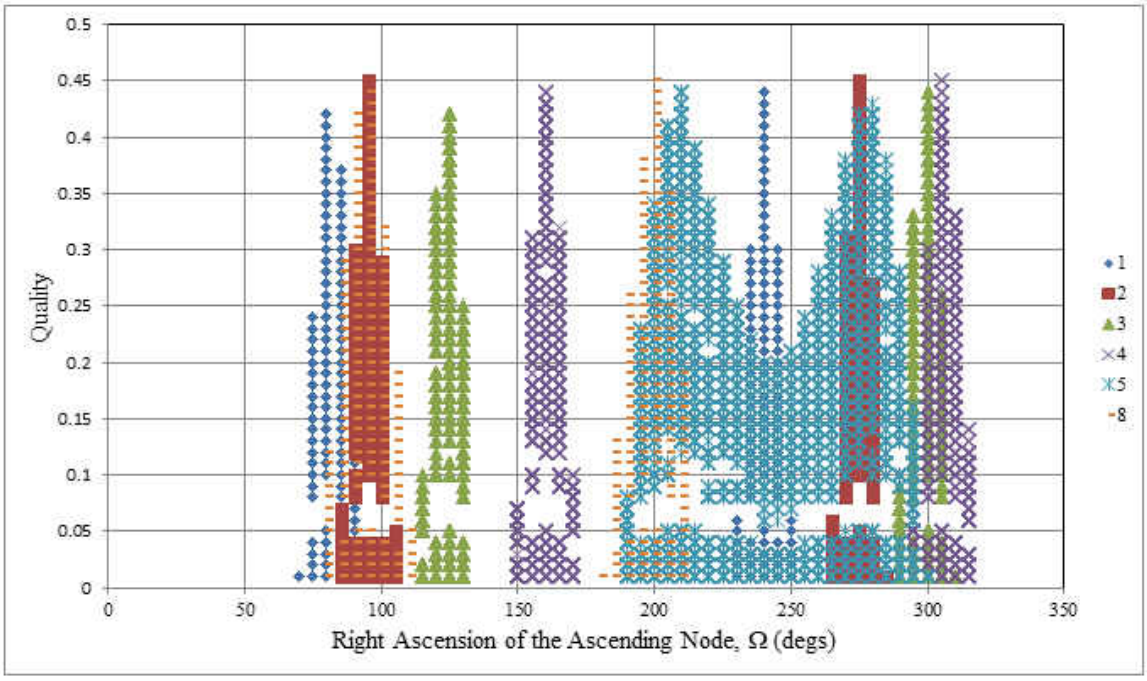

Figure 62 Right Ascension of Ascending Node vs. Total Quality for Multiple Headings at Vf=0.3

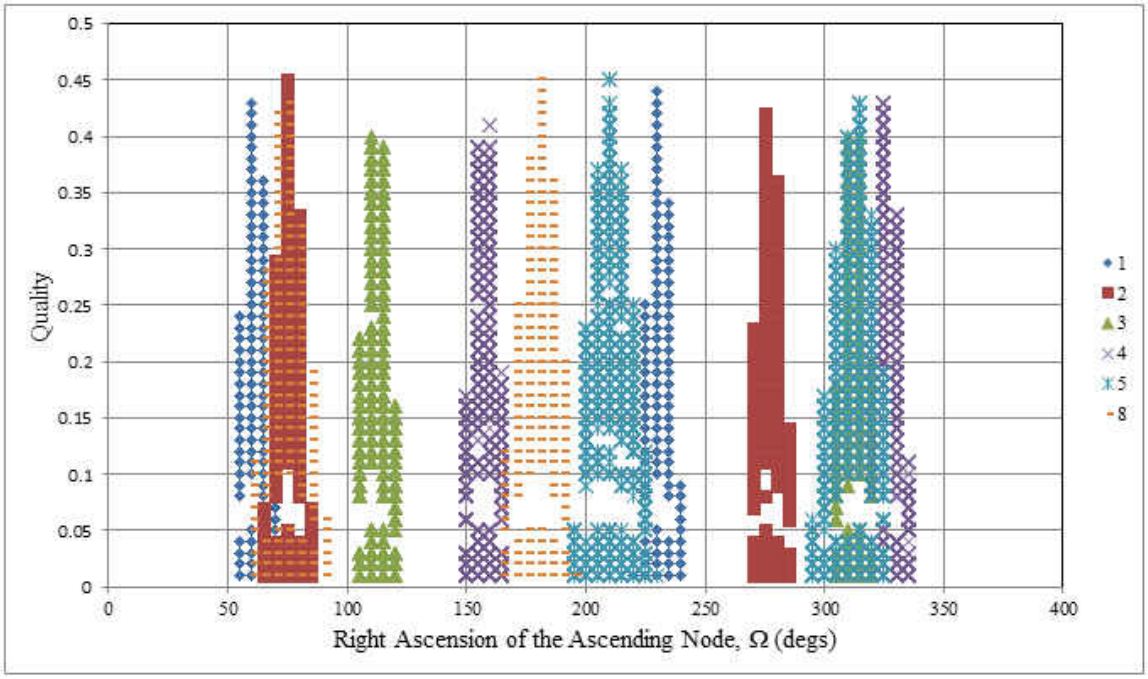

Figure 63 Right Ascension of Ascending Node vs. Total Quality for Multiple Headings at Vf=0.4

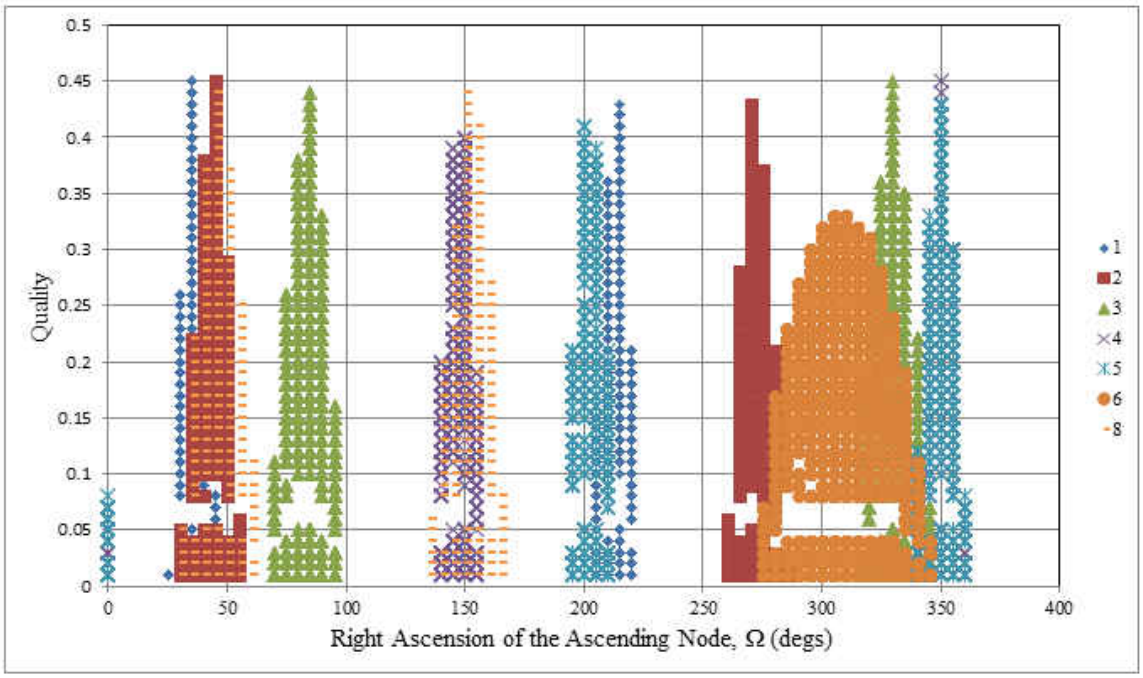

Figure 64 Right Ascension of Ascending Node vs. Total Quality for Multiple Headings at Vf=0.5

CHAPTER 5

CONCLUSIONS

5.1. Conclusions

This research has shown that for a given set of initial conditions for a space-based laser weapon system and a hypersonic glide vehicle, solutions for a laser weapon system intercepting the glide vehicle can be determined. The design methodology employed in this research employed simplifying assumptions with regard to the interaction of the laser and glide vehicle. A case study involving a single satellite demonstrated the effectiveness of this methodology, and a unique set of solutions was determined while varying the velocity ratio, angle of attack, and heading for the glide vehicle along with the true anomaly and right ascension of the ascending node for the space-based laser weapon system. As expected, the results showed that the glide vehicle was most vulnerable during its ballistic phase. Furthermore, by applying a series of quality metrics related to range, time, and trajectory geometries to the data set, the total quality or effectiveness of the interception was quantified.

5.2. Recommendations

Further investigation to refine the solution can be made by refining some of the simplifying assumptions. Regarding the LWS, this would include the effects of perturbations on the satellite orbit as well as a detailed physics model to incorporate target acquisition, tracking, beam power, and atmospheric effects. Additionally, increasing the number of LWS satellites in the constellation would allow for an increase in the number of intercepts of the HGV. With respect to the HGV, further incorporation of semi-random six degree of freedom motion within a power

and thermal budget would expand the application of the solution set allowing for an upper limit on vehicle operational capabilities that could be incorporated. Combining these improvements would yield an improved method for assessing orbital laser interception of an HGV by an LWS. Lastly, examining the dynamics and potential intercept of the laser and HGV from a land, sea, or air-based platform would have immediate applicability to systems under development.

REFERENCES

[1] A Sänger and J. Bredt, "A Rocket Drive for Long Range Bombers (Über einen Raketenantrieb für Fernbomber)," (translated by H. Hamermesh, CGD-32, US Navy, 1952), 1944.

[2] C. Hargis, "The X- 20 (Dyna- Soar) Progress Report," *Aeronautical Systems Division, U. S. Air Force*, 1964.

[3] A. Einsetin, "The Quantum Theory of Radiation," *Physikalische Zeitschrift*, vol. 18, no. 121, 1917.

[4] T. Maiman, "Optical and Microwave-Optical Experiments in Ruby," *Physical Review Letters*, vol. 4, no. 11, pp. 564-566, 1960.

[5] R. Reagan, Address to the Nation on Defense and National Security [Transcript], 1983.

[6] Missile Defense Agency. (2010, Feb) MDA News Release: Airborne Laser Testbed Successful in Lethal Intercept Experiment. [Online]. http://www.mda.mil/news/10news0002.html

[7] TACC. (2019, Dec) Vanguard Missile. [Online]. https://tass.ru/armiya-i-opk/7436431

[8] R. O'Rourke, "Navy Lasers, Railgun, and Gun-Launched Guided Projectile: Background and Issues for Congress (R44175)," Washington D.C., Congressional Research Report 2019.

[9] U.S. 114th Congress, "National Defense Authorization Act for Fiscal Year 2017 (114–255)," Washington D.C., Budget 2016.

[10] G.R. Mellinger, "Design and Operation of the X-15 Hypersonic Research Airplane," Istanbul, Turkey, October, 1960.

[11] J. Weil, "Review of the X-15 Program," NASA, Edwards, California, NASA-TN-D-1278, Dryden Flight Research Center June, 1962.

[12] T.C. Lin, "Development of U.S. Air Force Intercontinental Ballistic Missile Weapon Systems," *Journal of Spacecraft and Rockets*, vol. 40, no. 4, pp. 491-509, July-August 2003.

[13] R.A. Fuhrman, "The Fleet Ballistic Missile System: Polaris to Trident," *Journal of*

Spacecraft, vol. 15, no. 5, pp. 265-286, September-October 1978.

[14] J.W. Reece, R.D. Joseph, and D. Shaffer, "Ballistic Missile Performance," *Journal of Jet Propulsion*, vol. 26, no. 4, pp. 251-255, April 1956.

[15] J.P. McManus, "A History of the FBM System," Lockheed Missiles and Space Company, LMSC-255548, 1989.

[16] L.M. Nicolai, "A Perspective on the Requirements and Design for Advanced Cruise Missiles," in *AIAA-1979-1817, Proceedings of the AIAA Aircraft Systems and Technology Meeting*, New York, New York, August 1979.

[17] B.J. Kuchta, "Technology Advances in Cruise Missiles," in *AIAA-1981-0937, Proceedings of the Annual Meeting and Technical Display*, Long Beach, California, May, 1981.

[18] R.L. Hanson and M.H. Kiehle, "Performance Considerations in the Design of Subsonic Cruise Missiles," in *AIAA-1982-0371, Proceedings of the AIAA Aerospace Sciences Meeting*, Orlando, Florida, January, 1982.

[19] R.T. Voland, L.D. Huebner, and C.R. McClinton, "X-43A Hypersonic Vehicle Technology Development," *Acta Astronautica*, vol. 59, no. 1-5, pp. 181-191, July-September 2006.

[20] Bahm, C.M., Baumann, E., Martin, J.F., Bose, D.M., "The X-43 A Hyper-X Mach 7 Flight 2 Guidance , Navigation , and Control Overview and Flight Test Results.," American Institute of Aeronautics and Astronautics, 2005.

[21] M.R. Tetlow and C.J. Doolan, "Comparison of Hydrogen and Hydrocarbon-Fueled Scramjet," *Journal of Spacecraft and Rockets*, vol. 44, no. 2, pp. 365-373, April 2007.

[22] D. Lunan, "Waverider, a Revised Chronology," in *20th AIAA International Space Planes and Hypersonic Systems and Technologies Conference*, Glasgow, Scotland , July, 2015, pp. 1-22.

[23] R. Bakos, "Current Hypersonic Research in the USA," *Advanced Propulsion Technology High-Speed Aircraft*, vol. 10, pp. 1-26, 2008.

[24] J.M. Hank, J.S. Murphy, and R.C. Mutzman, "The X-51A Scramjet Engine Flight Demonstration Program," in *15th AIAA International Space Planes and Hypersonic Systems and Technologies Conference*, Dayton, Ohio, May 2008, pp. 1-13.

[25] R., Nacouzi, G., Lee, C., & Moore, R. Speier, "Hypersonic Missile Nonproliferation: Hindering the Spread of a New Class of Weapons," Santa Monica, CA, RR2137 2017.

[26] D. Morris, "Charts for Determining the Characteristics of Ballistic Trajectories in a Vacuum," Santa Monica, California, 1964.

[27] A. Eggers, H. Allen, and S. Neice, "A Comparative Analysis of the Performance of Long-Range Hypervelocity Vehicles," Moffett Field, California, NACA-TN-4046 1957.

[28] J. Acton, "Hypersonic Boost-Glide Weapons," *Science & Global Security*, vol. 23:3, pp. 191-219, 2015.

[29] S. Tan, H. Lei, and T. Liu, "Optimal Maneuver Trajectory for Hypersonic Missiles in Dive Phase Using Inverted Flight," *IEEE Access*, vol. 7, pp. 63493-63503, 2019.

[30] P. Nielsen, *Effects of Directed Energy Weapons*. Washington D.C.: National Defense University, 1994.

[31] D.L. Carroll, "Overview of High Energy Lasers: Past, Present, and Future," in *AIAA Plasmadynamics and Laser conference*, Honolulu, Hawaii, June 2011, pp. 1-21.

[32] C. Kopp, "High Energy Laser Directed Energy Weapons," Technical Report APA-TR-2008-0501 May, 2008.

[33] S. Lamberson, H.B. Schall, and O.L. Alvarado, "Overview of Airborne Laser's Test Program," *U.S. Air Force T&E Days*, pp. 1-4, December 2005.

[34] J. Tirpak, "Setting a Course for the Airborne Laser," *Air Force Magazine*, pp. 46-50, September 2003.

[35] Missile Defense Agency, "Supplemental Environmental Impact Statement for Airborne Laser Program," White Sands, New Mexico, June 2003.

[36] J.J. Wachs and G.T. Wilson, "United States Army Tactical High-Energy Laser Program," *Optical Engineering*, vol. 52, no. 2, October 2012.

[37] Congressional Research Service, "Navy Lasers, Railgun, and Gun-Launched GuidedProjectile: Background and Issues for Congress," Washington D.C., R44175 2019.

[38] H. Kaushal and G. Kaddoum, "Applications of Lasers for Tactical Military Operations," *IEEE Access*, vol. 5, pp. 20736-20753, September2017.

[39] C.B. Baxi and T. Knowles, "Thermal Energy Storage for Solid-State Laser Weapons Systems," *Journal of directed Energy*, vol. 1, pp. 293-308, 2006.

[40] Kim, D., Kim, J, Frist, D, Nagashima, M, Agrawa, B, "High Energy Laser Testbed for Accurate Beam Pointing Control," Monterey, CA, 2010.

[41] R. Ninneman, M. Vigil, and D. Founds, "Projected Technology Needs for an Operational Space-Based Laser," in *32nd AIAA Plasmadynamics and Lasers Conference*, Anaheim, California, June 2001, pp. 1-9.

[42] M.E. Capt. Zuber, J. Jackson, and M. Wacks, "Integrated Flight Experiment (IFX) Laser Payload Element (LPE) Progress," in *The Annual AIAA/BMDO Technology Conference [10th] - Unclassified Proceedings*, Williamsburg, Virginia, July 2001, pp. 1-9.

[43] M.E. Capt. Zuber, J. Jackson, and M. Wacks, "Integrated Flight Experiment (IFX) Laser Payload Element (LPE)," in *32nd AIAA Plasmadynamic and Lasers Conference*, Anaheim, California, June 2001, pp. 1-10.

[44] I. Col. Falto-Heck and A.H. Col. Steland, "Overview of the Space-Based Laser Integrated Flight Experiment," in *AIAA Space 2001 Conference and Exposition*, Albuquerque, New Mexico, August 2001, pp. 1-5.

[45] J., Milton, A. Parmentola, "Laser Satellite Constellations for Strategic Defense - An Analytical Model," *Journal of Spacecraft*, pp. Vol. 24, No.5, 1987.

[46] D.R. Wildt and S.A. Lissit, "Space-Based Chemical Lasers for Ballistic Missile Defense," in *AIAA 24th Plasmadynamics & Lasers Conference*, Orlando, Florida, July 1993, pp. 1-20.

[47] Department of Defense. (2001, July) Ballistic Missile Defense Program Briefing from DoD Archieves. [Online]. https://archive.defense.gov/news/briefingslide.aspx?briefingslideid=208

[48] J. Lt. Col. Zumwalt. (2019, April) Good Defense is the Best Offense with Hypersonic Missiles - The Hill. [Online]. https://thehill.com/opinion/national-security/438429-good-defense-is-the-best-offense-with-hypersonic-missiles

[49] N. Nguyen, "Performance Analysis of Skip-Glide Trajectories for Hypersonic Waveriders in Planetary Exploration," Master's Thesis, 2008.

[50] J. Sellers, *Understanding Space An Introduction to Astronautics*. New York, New York: McGraw-Hill, 2004.

[51] H. Curtis, *Orbital Mechanics for Engineering Students*. Oxford, England: Elsevier, 2005.

[52] NASA, "Orbital Flight Handbook," Huntsville, Alabama, 1963.

[53] H. Goldstein, C. Poole, and J. Safko, *Classical Mechanics 3rd Ed.* New York, New York: Addison Wesley, 2005.

[54] The Mathworks, Inc. (2013) MATLAB R2013a, Version 8.1.0.604. Computer Software.

[55] R. Pawlowicz. (2020) M_Map version 1.4m: A mapping package for MATLAB. Computer Software.

[56] Condoleo, E.. (2019) MATLAB Central File Exchange. [Online]. https://www.mathworks.com/matlabcentral/fileexchange/45573-orbit3d

[57] DeMark, R. (2019) MATLAB Central File Exchange. [Online]. https://www.mathworks.com/matlabcentral/fileexchange/69439-orbit-trajectory-propagation

[58] Reichelt, M. and Shampine, L., "The MATLAB ODE Suite," vol. 18-1, 1997.

[59] H. Lin, "Rationalized Speed/Altitude Thresholds for ABM Testing," *Science & Global Security*, vol. 2, pp. 87-101, 1990.

[60] D. Brooks, "An Introduction to Orbit Dynamics and its Application to Satellite-Based Earth Monitoring Systems," Hampton, Virginia, 1977.

[61] P. Zarchan, "Tactical and Strategic Missile Guidance, Progress in Astronautics and Aeronautics," in *American Institute of Aeronautics and Astronautics*, vol. 124, Reston, Virginia, 1990.

[62] H. Hablani, "Design of a Spacecraft Pointing Control System for Tracking Moving Objects," in *AIAA Guidance, Navigation and Control Conference*, Monterey, California, August 1987, pp. 1481-1494.

[63] A. Bourdeau, "Hypersonic Air-Breathing Propulsion Efforts In the Air Force Research Laboratory," in *AIAA/CIRA 13th International Space Planes and Hypersonics Systems and Technologies Conference*, Capua, Italy, 2005.

VITA

Robert Joseph Fowler IV earned his Bachelor of Science degree in Mechanical Engineering from Michigan Technological University in 2004. Following graduation, he worked briefly for several defense contractors in the Washington D.C. area working on submarines. He then joined the Department of the Navy as a Mechanical Engineer in Dahlgren, Virginia. His work focused on gun weapon system and precision missile system design, analysis, manufacturing, and testing. He led the mechanical development of the 30mm and 105mm Gun Weapon Systems for the Special Operation Command's next-generation AC-130W and AC-130J Gunships from 2009 until 2016, where he also earned several patents for innovative mechanisms and linkages. He later led the topside development of the Navy's amphibious transport dock, LPD-17 Flight II. He also founded a software development team committed to designing a toolset focused on increased holistic analysis results within a reduced schedule for use in naval ship design. He is currently the Chief Engineer of the Topside Engineering Branch in Dahlgren, Virginia. He will complete his Master of Science in Aerospace Engineering in December 2020 from Old Dominion University in Norfolk, Virginia.